Electrocatalysis in Water Electrolysis with Solid Polymer Electrolyte

by

Egil Rasten

Thesis submitted in partial fulfilment of the
requirements for the degree
Doktor Ingeniør

Norwegian University of Science and Technology
Department of Materials Technology and Electrochemistry

October 2001

URN:NBN:no-7264

URN:NBN:no-7264

List of symbols

Symbol	Explanation
α	Transfer coefficient
b	Tafel slope ($mV \cdot dec^{-1}$)
C	Capacitance ($C \cdot cm^{-2}$)
E_{RHE}	Potential vs. reversible hydrogen electrode (V)
E^{rev}	Reversible potential (V)
E^0	Standard potential (V)
ε	Efficiency (%)
η	Overpotential (V)
F	Faraday constant ($96487\ C \cdot cm^{-1}$)
i / cd	Current density ($A \cdot cm^{-2}$)
i_0	Exchange current density ($A \cdot cm^{-2}$)
q*	Integrated voltammetric charge ($C \cdot cm^{-2}$)
p_{H_2}	Hydrogen pressure (atm)
p_{O_2}	Oxygen pressure (atm)
R	Gas constant ($8.314\ J \cdot K^{-1} \cdot mol^{-1}$)
ν	Volt scan rate ($mV \cdot s^{-1}$)
U_{cell}	Cell voltage (V)
RHE	Reversible hydrogen electrode
rds	Rate determining step
T	Temperature (K)
λ	Membrane water content ($n_{H_2O}/n_{SO_4^-}$)
ξ	Water drag coefficient (H_2O/H^+)

URN:NBN:no-7264

Acknowledgements

The present work was carried out at the Department of Materials Technology and Electrochemistry at NTNU, in the period from June 1997 to October 2001 under the supervision of Professor Reidar Tunold and co-supervisor Professor Georg Hagen. The supervisors are acknowledged for support and for showing great interest in my work. Thanks to Dr. Børre Børresen for many fruitful discussions.

I would also like to acknowledge the department of Hydrogen Energy at Kurchatov Institute in Moscow for letting me stay three weeks at their laboratory.

A special thanks to Martha Bjerknes and Kjell Røkke for all practical help and for showing endless patience.

The Research Council of Norway (NFR) is acknowledged for financial support.

Summary

Development and optimization of the electrodes in a water electrolysis system using a polymer membrane as electrolyte have been carried out in this work. A cell voltage of 1.59 V (energy consumption of about 3.8 kWh/Nm^3 H_2) has been obtained at practical operation conditions of the electrolysis cell (10 kA $\cdot$ m^{-2}, 90 °C) using a total noble metal loading of less than 2.4 mg$\cdot$cm^{-2} and a Nafion® -115 membrane. It is further shown that a cell voltage of less than 1.5 V is possible at the same conditions by combination of the best electrodes obtained in this work.

The most important limitation of the electrolysis system using polymer membrane as electrolyte has proven to be the electrical conductivity of the catalysts due to the porous backing/current collector system, which increases the length of the current path and decreases the cross section compared to the apparent one. A careful compromise must therefore be obtained between electrical conductivity and active surface area, which can be taylored by preparation and annealing conditions of the metal oxide catalysts.

Anode catalysts of different properties have been developed. The mixed oxide of Ir-Ta (85 mole% Ir) was found to exhibit highest voltage efficiency at a current density of 10 kA $\cdot$ m^{-2} or below, whereas the mixed oxide of Ir and Ru (60-80 mole% Ir) was found to give the highest voltage efficiency for current densities of above 10 kA $\cdot$ m^{-2}.

Pt on carbon particles, was found to be less suitable as cathode catalyst in water electrolysis. The large carbon particles introduced an unnecessary porosity into the catalytic layer, which resulted in a high ohmic drop. Much better voltage efficiency was obtained by using Pt-black as cathode catalyst, which showed a far better electrical conductivity.

Ru-oxide as cathode catalyst in water electrolysis systems using a polymer electrolyte was not found to be of particular interest due to insufficient electrochemical activity and too low electrical conductivity.

URN:NBN:no-7264

URN:NBN:no-7264

Contents

Chapter 1

Introduction

1.1 Hydrogen as an energy carrier - background

Increasing energy demand has led to rapid consumption of fossil fuels and to an increasing release of climate gases and growing environmental concern among the public. The fossil fuels are finite in amount and within a few decades the availability will reach a peak where oil and gas becomes more difficult to exploit. Fossil fuels are unevenly distributed throughout the world and less access to this energy source may cause serious international conflicts. Additionally, fossil fuels should be preserved for non-energy applications where there is no substitute (synthetic materials) [1].

The release of CO_2 to the atmosphere and its impact on global warming has caused major concern worldwide and has led to international agreements on the reduction of CO_2 emission (Kyoto). There is still much dispute about the connection between CO_2 emission and global warming, however, there exist a general acceptance to carry on a "no regret policy" and to take necessary precautions [2].

Hydrogen as an energy carrier, generated from renewable energy sources, constitutes an environmental friendly solution to the world energy problem in the future. After oil-crisis and public awareness of the pollution caused by fossil fuels, rapid development of hydrogen energy systems has taken place during the last decade. In particularly the development of fuel cell technology, where hydrogen together with oxygen is chemically converted to electrical energy and water, has promoted the use of hydrogen as a fuel in vehicle propulsion. Today, fuel cell technology research has been committed by most of the largest car producers and research and development is in rapid progress.

Fuel cell technology based on a Solid Polymer Electrolyte (SPE), also denoted Proton Exchange Membrane (PEM), has gained a large interest due to the absence of a hazardous electrolyte, a low temperature regime, high power density and high

energy efficiency compared to other fuel cell systems. The acidic environment provided by the membrane requires electrodes of expensive noble metals and much research has been devoted to bring the necessary amount of noble metals down to a minimum to reduce the material costs [3]. The polymer membrane provides the same advantages in water electrolysis, where hydrogen and oxygen is produced from splitting of water using DC-power. However, noble metal electrodes are also required in water electrolysis systems and further research is necessary to bring down the material costs.

Some historical mile stones in the progress of hydrogen energy prospect:

- The first discovery of the possibility of splitting of water by electrolysis dates back to 1789 when the merchant Adriaan Paets van Trootswijk and medical doctor Johan Rudolph in Amsterdam, found that water could be split into hydrogen and oxygen gas by electric power. This was further brought into the public by Nicholas and Carlisle in 1800 [4].
- In 1839 sir William Groove, who worked on water electrolysis, discovered the corresponding process that hydrogen together with oxygen was able to generate electric power and one of the first primitive fuel cells was a fact [5].
- In 1902 more than 400 industrial electrolysers were in operation [6].
- In 1930s F. T. Bacon demonstrated the first alkaline fuel cell [5].
- A polymer membrane fuel cell was described by Grubb in 1959 and the first SPE® fuel cell used in an operating system was developed by General Electric and used as a power source of the Gemini Spacecraft during the mid 1960s [7].
- A small group of people, called the "Hydrogen Romantics", gathered and formed the International Association of Hydrogen Energy (IAHE) in 1974 in Miami Beach, Florida, and the hydrogen energy movement was a fact [8].

The only practical way to produce hydrogen using renewable energy sources is by water electrolysis [9].

1.2 Hydrogen by water electrolysis

Prior to the oil and gas age, hydrogen for industrial purposes was mainly produced by electrolysis of water when cheap electrical power was available. Today, water electrolysis is preferred for production of H_2 wherever on-site production is a more practical solution or when very pure H_2 is necessary. Approximately 4 % of todays H_2 is produced by electrolysis of water [10] and typical applications of hydrogen from water electrolysis are:

- Food industry
  - Hydrogenation of fatty acids
- Metallurgical industry
  - Reducing atmosphere
  - Furnace atmosphere
- Semi-conductors
  - Furnace atmosphere
- Chemical industry
  - Petrochemical refining of polyethylene, polypropylene
- Meteorological balloons
- Cutting/welding
  - High temperature flames
- Laboratory R&D

In water electrolysis, water is split to hydrogen and oxygen gas by use of DC-power in an electrolyser unit. Electrolysers can be distinguished by type of electrolyte and materials used for electrodes. Conventional electrolysis technology uses alkaline aqueous electrolyte of 25 % KOH and Ni based electrodes, which typically operates at 2 $kA \cdot m^{-2}$ and 80 °C and a cell voltage of 1.8 - 2.1 V [11]. Electrolysis systems using a solid polymer electrolyte and electrodes of platinum metals typically operates at 10 $kA \cdot m^{-2}$ and 80-90 °C at a cell voltage of $\sim$ 1.7 V (see section 3.1).

Large scale production of hydrogen by electrolysis is today dominated by the alkaline electrolysis technology. Electrolysers using solid polymer electrolyte becomes too expensive due to the high material costs, e.g. noble metal catalysts and polymer membrane. However, on long term where hydrogen becomes the main energy carrier and where large scale production of hydrogen take place from renewable energy sources, the energy efficiency of the electrolyser will become essential. The solid polymer electrolyte electrolyser has been proven as the most promising system with respect to high energy efficiency and high current density, and further research is important to bring down material costs of such systems.

1.3 Scope of present work

The objective of the present work is to bring down the high material costs of the electrolysis system using solid polymer electrolyte. The energy efficiency and the current density of the system is determined by the noble metal catalysts, which constitute the critical part of the electrodes. The main key to bring down the high material costs of the electrolyser will be to further develop and improve the noble metal catalysts, which facilitate:

- Lower amounts of noble metals
- Higher energy efficiency
- Higher specific production capacity
- Longer life time

In order to achieve further improvements of todays technology, the system must be characterized and studied to understand and reveal the most important limitations and further optimization of electrodes/catalysts must be carried out. This involves development of methods for preparation of electrodes/catalysts and methods for electrochemical characterization.

Chapter 2

Theory

2.1 Thermodynamics

In water electrolysis, the net reaction for splitting of water is given by:

$$H_2O_{(l)} \rightarrow H_{2(g)} + \frac{1}{2}O_{2(g)} \tag{2.1}$$

Gibbs free energy of reaction 2.1, ΔG, is given by equation 2.2:

$$\Delta G = \mu_{H_{2(g)}} + \frac{1}{2}\mu_{O_{2(g)}} - \mu_{H_2O_{(l)}} = \Delta G^0 + RT \ln\left(p_{H_2} p_{O_2}^{\frac{1}{2}}\right) \tag{2.2}$$

where μ are chemical potentials and ΔG^0 is the Gibbs free energy at standard conditions of 25 °C and atmospheric pressure. The activity of water is assumed unity. The energy balance of reaction 2.1 is to be referred to the enthalpy by equation 2.3:

$$\Delta G = \Delta H - T \cdot \Delta S \tag{2.3}$$

where ΔH is the enthalpy and ΔS is the entropy of the reaction. The formation equation for ΔG^0 at different temperatures can be expressed as [12]:

$$\Delta G^0(T) = -295.6 - 0.033 \cdot T \cdot \ln T + 2.81 \cdot 10^{-6} \cdot T^2 - 12.77 \cdot T^{-1} + 0.38 \cdot T \quad \text{(kJ/mole)} \tag{2.4}$$

The reversible potential, E^{rev} is given by:

$$E^{rev} = -\frac{\Delta G}{nF} = -\frac{\Delta G^0}{nF} - \frac{RT}{nF} \ln\left(p_{H_2} \cdot p_{O_2}^{\frac{1}{2}}\right) \tag{2.5}$$

$$= E^0 - \frac{RT}{nF} \ln\left(p_{H_2} \cdot p_{O_2}^{\frac{1}{2}}\right) \tag{2.6}$$

where n is the number of electrons involved in reaction 2.1, F is Faradays number and E^0 is the standard potential. E^{rev} is theoretically the lowest potential at given conditions which must be applied between two electrodes for reaction 2.1 to proceed to the right.

At 298 K and atmospheric pressure, $E^{rev} = 237349/2 \cdot 96487 = 1.230$ V. Figure 2.1 shows how E^{rev} changes by pressure and temperature according to equations 2.4 and 2.5. It can be seen that E^{rev} decreases more or less linearly with the temperature and increases at increasing pressures.

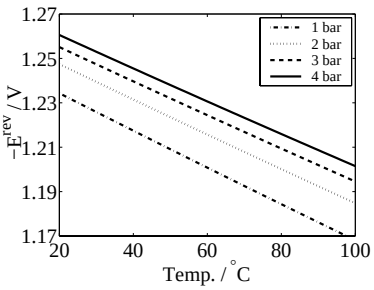

Figure 2.1: Change of E^{rev} by temperature and pressure.

ΔH is a measure for the energy required to break and form molecular bonds and to bring reactants and products into their reference states [13]. When the cell potential, U_{cell}, equals the thermoneutral potential difference, $U_{tn} = \Delta H/nF$, no net heat exchange with the surroundings takes place. For $U_{cell} < U_{tn}$, the cell absorbs heat from its surroundings and the opposite takes place for $U_{cell} > U_{tn}$. At standard conditions $U_{tn} = 285000/2 \cdot 96487 = 1.48$ V.

The thermal energy efficiency can be defined as:

$$\varepsilon_{\Delta H} = \frac{U_{tn}}{U_{cell}} \tag{2.7}$$

whereas the energy efficiency in terms of Gibbs energy can be defined as:

$$\varepsilon_{\Delta G} = \frac{E^{rev}}{U_{cell}} \tag{2.8}$$

In an electrochemical process the energy efficiency is better expressed by $\varepsilon_{\Delta G}$ which represents the efficiency in terms of the available work (exergy and 2. law of thermodynamics [14]).

2.2 Kinetic expressions

The reaction given by equation 2.1 can be divided into a cathode and an anode reaction given by equation 2.9 and 2.10 respectively.

$$2H^+ + 2e^- \rightleftarrows H_{2(g)} \tag{2.9}$$

$$H_2O \rightleftarrows 2H^+ + 2e^- + \frac{1}{2}O_{2(g)} \tag{2.10}$$

The reactions will follow specific paths and can be further divided into different steps depending on the state of the electrode material, see section 2.4.1 and 2.4.2. To determine the rate determining step (rds) of the reaction, kinetic expression must be derived on the basis of a possible reaction mechanism.

Given a simple electron charge transfer reaction between an oxidized and a reduced species:

$$O + e^- \rightleftarrows R \tag{2.11}$$

where O and R are oxidized and reduced species respectively and e is an electron. Assuming equal activity of O and R, the empirical relation between the current density and the overpotential for equation 2.11 can be described by the Butler-Volmer equation:

$$\mathrm{i} = \mathrm{i}_0 \cdot \left\{ \exp\left(\frac{\alpha \mathrm{nF}}{\mathrm{RT}}\eta\right) - \exp\left(-\frac{(1-\alpha)\mathrm{nF}}{\mathrm{RT}}\eta\right) \right\} \tag{2.12}$$

where i is current density (cd), i_0 is the exchange current density, η is the overpotential defined as $\eta = \mathrm{E} - \mathrm{E}^{\mathrm{rev}}$ and E is the applied potential. R, T and F has its usual meanings and n is number of electrons involved in the reaction. If reaction 2.11 is driven sufficiently in anodic or cathodic direction, the cathodic or anodic term respectively will disappear and η can be solved to give cathodic and anodic Tafel equations:

$$\eta_{\mathrm{c}} = \mathrm{b}_{\mathrm{c}} \cdot \log \frac{|\mathrm{i}|}{\mathrm{i}_0} \tag{2.13}$$

$$\eta_{\mathrm{a}} = \mathrm{b}_{\mathrm{a}} \cdot \log \frac{\mathrm{i}}{\mathrm{i}_0} \tag{2.14}$$

where b_{c} and b_{a} are cathodic and anodic Tafel slopes respectively given by:

$$\mathrm{b}_{\mathrm{c}} = -\frac{\mathrm{RT} \cdot 2.303}{(1-\alpha)\mathrm{nF}} \tag{2.15}$$

$$\mathrm{b}_{\mathrm{a}} = \frac{\mathrm{RT} \cdot 2.303}{\alpha \mathrm{nF}} \tag{2.16}$$

In equation 2.15 and 2.16 α is the transfer coefficient. α is usually close to 0.5, and expresses the activation barrier of the electrochemical reaction. For $\alpha = 0$ the barrier is activationless (spontaneous reaction) and for $\alpha = 1$ there is no barrier (spontaneous back-reaction) [15]. The rds in a given reaction path can be determined from the Tafel constant and from the reaction order of the participating species.

2.3 Experimental methods

2.3.1 Steady state polarization

By polarizing the electrode under equilibrium conditions, the steady state polarization behaviour of the electrode reaction can be measured. The measurement can be performed either by controlling the current (galvanostatic control) or the potential (potentiostatic control) and the response in potential or current is measured. The steps are performed in small increments and the response is measured typically after 10 minutes where equilibrium conditions of the electrode reactions

can be assumed. Steady state polarization measurements include all polarization effects including the thermodynamic potential, the overpotential due to the surface reactions, ohmic losses and diffusion terms.

To drive the reaction 2.1 at a practical rate, additional energy must be applied to overcome the kinetic hindrance of the reaction and the ohmic resistance. The potential which must be applied at a given rate, is given by:

$$U_{cell} = E^{rev} + \eta + i \cdot R_\Omega \tag{2.17}$$

where R_Ω is the ohmic resistance of electrolyte, cable connections and wires. η can be divided into cathodic and anodic parts:

$$\eta = \eta_c - \eta_a \tag{2.18}$$

and are given by the Tafel equations above. By polarization of an electrode, e.g. in anodic direction, and measuring the potential versus a reference electrode the cathodic term can be neglected and equation 2.17 is written:

$$E = E^{rev} + b_a \cdot \log \frac{i}{i_0} + i \cdot R_\Omega \tag{2.19}$$

$$= E' + b_a \cdot \log i + i \cdot R_\Omega \tag{2.20}$$

where

$$E' = E^{rev} + b_a \cdot \log i_0 \tag{2.21}$$

At low cd where R_Ω can be neglected, b_a and E' can be found from the slope of the curve. For high cd the data must first be corrected from iR-drop or, if proper knowledge about the reaction exists, it can be found by fitting equation 2.19 to the measured data.

2.3.2 Cyclic voltammetry

Cyclic voltammetry (CV) is a surface sensitive technique where each material gives rise to a unique spectrum in a given medium. The method is often applied for determination of the physio-chemical state of an electrode surface. CV is useful to study the behaviour of adsorbed species, participating as reaction intermediates in a given reaction or as impurities, as well as redox couples in the solution and at the electrode surface. Cycling the potential at different scan rates can be performed to find diffusion coefficients of electroactive species and the capacitance of an electrode (active surface area). Additionally, CV can give information about the reversibility of a the charging/discharging process [16].

In CV the potential is swept at a certain rate, ν, within the potential range of interest and the current response is measured. The potential at a given time can be written:

$$E_t = E_{t=0} \pm \nu \cdot t \tag{2.22}$$

where t is the time, E_t is the controlled potential, $E_{t=0}$ is the starting potential and plus and minus indicates anodic and cathodic direction of the sweep respectively. Table 2.1 shows some diagnostic criteria to determine the reversibility of a charge transfer reaction without diffusion or activation limitations where p indicate a point of interest in the voltammogram, usually a peak or a point at fixed potential.

Table 2.1: Diagnostic criteria for reversible reactions without diffusion limitations.

1.	$i_p \propto \nu$
2.	$\lvert i_p^a / i_p^c \rvert = 1$
3.	E_p independent of ν
4.	$\Delta E_p = E_p^a - E_p^c < 59/n$ mV

Capacitance

The double-layer capacitance, C_{dl}, arises from the potential dependence of electrostatic charging of the electrode surface balanced by dipole orientation of ions and water molecules in the solution near the surface. Electrosorption of species at the surface of an electrode give rise to a so-called pseudocapacitance, C_ϕ, where an intermediate is formed that stores charge at the surface. In contrast to double-layer charging, psuedocapacitance is a Faradaic process where the electrons cross the double layer region [17]. The total capacitance of an electrode can be derived from CV by performing multiple scans at different scan rates, ν:

$$i = C\frac{dV}{dt} = C \cdot \nu \tag{2.23}$$

$$C = \frac{i}{\nu} \tag{2.24}$$

For a reversible process controlled by electrode kinetics, a plot of i versus ν will give a straight line with slope equal to C.

Porous electrodes can give raise to a non-uniformity of charging/discharging down the pores, due to ohmic effects which makes potential penetration into the pores more difficult and may result in a locally smaller potential range [18].

Integrated charge

The voltammetric charge of an electrode can be found from equation 2.25:

$$\Delta q* = \int_{E_1}^{E_2} \frac{I}{\nu} dV \tag{2.25}$$

by integration between E_1 and E_2. q^* is independent of ν in the absence of ohmic drop, diffusion and/or kinetic limitations of the charging process.

2.3.3 AC-impedance

In an AC-impedance measurement a small sinusoidal voltage perturbation[1] is superimposed on a fixed potential, and the response in current is measured [19]. The voltage perturbation is typically applied over a wide frequency range, e.g. 10 kHz to 1 mHz, where different type of surface phenomena may give rise to a response in different parts of the frequency domain. For electrochemical systems of nonlinear behaviour, linearisation of the equations can be performed when the perturbation is small, usually about ±10mV.

The voltage perturbation E(t) with an amplitude of E_m and frequency f (angular frequency of $\omega = 2\pi f$) is given in equation 2.26.

$$E(t) = E_m \sin(\omega t) \tag{2.26}$$

The current response, I(t), will be a sinusoidal function of the voltage perturbation with a shift in angular frequency and a different amplitude, given by equation 2.27.

$$I(t) = I_m \sin(\omega t + \phi) \tag{2.27}$$

I_m is the amplitude of the current and ϕ is the phase shift. The relation between current and voltage can be visualised in figure 2.2 where the current is shifted by ϕ. The magnitude of the impedance is given as the ratio between E(t) and I(t):

$$|Z(\omega)| \equiv \frac{E}{I}(\omega) \tag{2.28}$$

The impedance can be expressed as a vector on complex form by equation 2.29 and is plotted as rectangular coordinates as shown in figure 2.3.

$$Z(\omega) = Z' + jZ'' \tag{2.29}$$

It can be seen from figure 2.3 that the rectangular coordinate values are:

$$\mathrm{Re}(Z) \equiv Z' = |Z| \cos\theta \tag{2.30}$$

$$\mathrm{Im}(Z) \equiv Z'' = |Z| \sin\theta \tag{2.31}$$

with the phase angle:

$$\theta = \arctan\left(\frac{Z''}{Z'}\right) \tag{2.32}$$

and the modulus:

$$|Z| = \left[\left(Z'\right)^2 + \left(Z''\right)^2\right]^{1/2} \tag{2.33}$$

Equation 2.33 can be used for representation of the impedance in a so-called Nyquist diagram, which results in a semicircle in the complex plane.

[1] A small current perturbation can also be applied

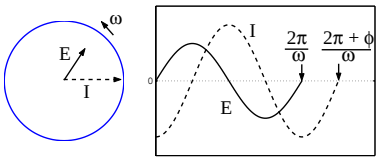

Figure 2.2: Graphical reperesentation of the current voltage relationship.

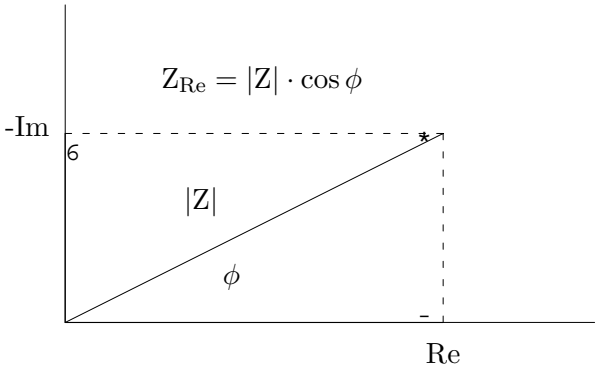

Figure 2.3: Impedance representation on vector form.

Equivalent circuit representation

In AC-impedance measurements the different phenomena taking place at an electrode are typically expressed in terms of electrical circuit elements, i.e. ohmic resistor (R), capacitance (C) and inductance (L). The impedance of the imaginary and real parts of the different circuit elements are summarized in table 2.2.

Table 2.2: Equivalent circuit elements

	Z	Z_{Re}	Z_{Im}
R	Z_R	R	-
C	Z_C	-	$\frac{1}{j\omega C}$
L	Z_L	-	$j\omega C$

The simple charge transfer reaction given by equation 2.11 can be expressed by the Randles circuit shown in figure 2.4 where R_Ω is the ohmic resistance (solution, cable connections etc.), R_{ct} is the charge transfer resistance and C_{dl} is the double layer capacitance. The impedance of this circuit can be written as:

$$Z = Z_{R_\Omega} + \left(Z_{R_{ct}}^{-1} + Z_{C_{dl}}^{-1}\right)^{-1} \tag{2.34}$$

$$= R_\Omega + \left(R_{ct}^{-1} + \left(\frac{1}{j\omega C}\right)\right)^{-1} \tag{2.35}$$

By manipulation of equation 2.35, and keeping in mind that $j^2 = -1$, the impedance

can be written:

$$Z = R_\Omega + \frac{R_{ct}}{1 + (\omega C R_{ct})^2} - j \cdot \frac{\omega C R_{ct}^2}{(\omega C R_{ct})^2} \tag{2.36}$$

From equation 2.36 it can be seen that when $\omega \to \infty$, $Z \to R_\Omega$. When $\omega \to 0$, $Z \to R_\Omega + R_{ct}$. Equivalent circuit models can be developed on the basis of assumption about rate determining electrode processes of a given reaction, and the model can be evaluated by fitting the model to measured data. Physical quantities of the electrode process can then be obtained. Fitting procedures of impedance data are implemented in most impedance software programs. The impedance represented by the circuit model in figure 2.4 shows that R_Ω is connected in series with a parallel combination of R_{ct} and C_{dl}. This circuit can also be written by a so-called Boucamp-representation as $R_\Omega(R_{ct}C_{dl})$.

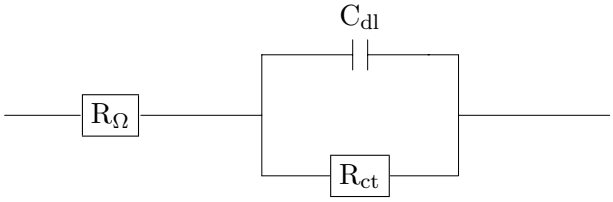

Figure 2.4: Circuit representation of a simple charge transfer reaction with ohmic resistance.

Graphical interpretation

The resulting impedance can also be graphically represented by an impedance diagram, the so-called Nyquist diagram shown in figure 2.5. The time constant of the process, τ, is given in equation 2.37 and can be found for a characteristic frequency at the maximum of the graph as shown in figure 2.5.

$$\omega_0 = 2\pi f_{max} = \frac{1}{R_{ct}C_{dl}} \tag{2.37}$$

$$\tau = \frac{1}{\omega_0} \tag{2.38}$$

R_{ct} can be found as the diameter of the semi circle and C_{dl} can be found from ω_0 and R_{ct} by using equation 2.37. The total polarization resistance can be found as the intercept by the real axis as $\omega \to 0$.

Constant Phase Element (CPE)

A CPE element is often used to model electrodes of porous nature and to model diffusion processes.

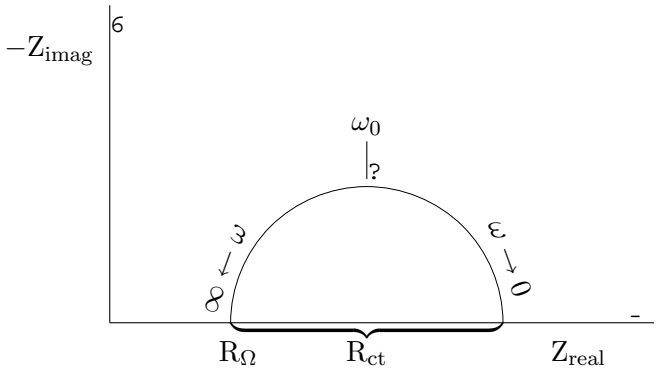

Figure 2.5: Nyquist representation of AC-impedance.

Rough and porous electrode surfaces may give raise to a suppressed or a tilted semicircle in the Nyquist diagram, caused by frequency dispersion of the interfacial impedance [19]. The impedance of a porous electrode have been explained by considering each pore by a transmission-line model where the potential or current slowly penetrate the pore and the phase angle becomes close to 45° under kinetic control and 22.5° under diffusion control [20].

Diffusion impedance results in a straight line with a slope of 45° in the Nyquist diagram and for diffusion within a finite distance the impedance intercept the real axis at low frequency [21].

The impedance of a CPE element is given by:

$$Z_{CPE} = \frac{1}{B(i\omega)^{\alpha}} \tag{2.39}$$

where B is a frequency independent term, ω is the angular frequency, $i = \sqrt{-1}$ and α is a value between 0 and 1. For $\alpha = 0$, Z_{CPE} becomes a pure resistor, for $\alpha = 0.5$ a Warburg element (diffusion) and for $\alpha = 1$ a pure capacitor where the value of B equals the capacitance.

2.3.4 Brunauer-Emmet-Teller (BET)

The BET isotherm is useful for determining the surface area of catalysts. In contrast to the Langmuir isotherm, it also takes into account multilayer adsorption. By BET the amount of adsorbed N_2 gas is measured. The adsorption process can occur by formation of chemical bonds, denoted chemisorption, or by weak van der Waals forces called physical adsorption. The enthalpy for formation of the first monolayer is assumed to be different and greater in magnitude than that of the second and higher layers.

The BET equation is given by:

$$\frac{\frac{P}{P_0}}{V_m\left(1-\frac{P}{P_0}\right)} = \frac{1}{V_m c} + \frac{(c-1)\left(\frac{P}{P_0}\right)}{V_m c} \tag{2.40}$$

where P is the equilibrium pressure, P_0 is the vapour pressure of the adsorbate at standard conditions, V_m is the volume required to cover the adsorbent surface with a monolayer of adsorbate and c is a temperature-dependent constant related to the enthalpies of adsorption of the first and higher layers.

2.4 Electrode reactions in PEM water electrolysis

2.4.1 The hydrogen evolution reaction (HER)

The standard potential of H_2 is by definition zero. As a first approximation the electrochemical activity of HER on different metals can be compared by a so-called "Vulcano-plot", where $\log(i_0)$ is related to the bond energy of chemisorbed H to the metal [22]. A "Vulcano-plot" is shown in figure 2.6 and it can be seen that the metals of intermediate bond-strength energy is the most active towards the HER represented by the noble metals [22]. For the metals of low bond-strength on the left side of the curve discharge of H becomes the rate determining step, whereas for the metals on the right side of stronger bond-strength the H desorption step becomes the rate determining step [23]. The noble metals are of particular interest here due to their corrosion resistance in acidic solution.

Attempts to combine different metals from the opposite branches of the "Vulcano-plot" to obtain properties of the intermediate bond strength have been carried out, however, with limited success for only a few metals. The Pt electron configuration can be imitated by the combination of metals from the left side of the periodic table with metals from the right side of the periodic table, analogue to the Brewer-Engels theory [13]. This means to combine metals which have less than five d-electrons (hypo-electronic) with metals which have more than five d-electrons (hyper-electronic) in the outer shell. The acidic environment caused by the membrane limits the choice of materials to noble metals as Pt, Pd, noble metal oxides like RuO_2 / IrO_2 and to a few tungsten compounds (WO_3, WC) [13]. The reaction of HER together with the Tafel slopes of the rate determining steps are given in table 2.3.

Hydrogen evolution on Pt

Pt is known as the most active catalyst for the HER and is commonly used in fuel cell for the catalysis both of hydrogen oxidation and oxygen reduction. Thus, a large number of Pt catalysts are available on the commercial marked, optimized to provide high surface area to minimize the necessary catalyst loading.

Pt has, as an isolated atom in gaseous ground state a d^9s configuration which redistributes to an electronic configuration of $d^{7.5}sp^{1.5}$ in the lattice. These d-orbitals are pointing out from the metal surface and provide two half occupied d-orbitals, each able to bind one H-atom, and one fully occupied d-orbital able to bind H_3O^+/H_2O species. For Pt particles on a nano-meter scale, more d-orbitals per Pt atom may become available [23].

The HER on Pt occurs on a strongly bounded underpotential deposited (UPD) monolayer of H atoms. UPD hydrogen starts to cover the Pt surface at about

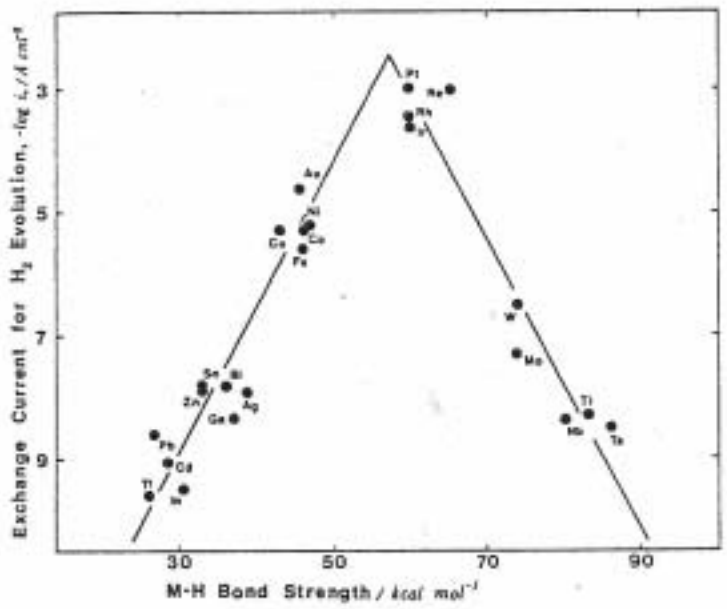

Figure 2.6: Vulcano-plot of HER on different metals [22].

Table 2.3: Reaction steps and Tafel slopes of HER [11].

			b_a low η	b_a high η	
$M + H_3O^+ + e^-$	$\rightleftarrows$	$M - H_{ads} + H_2O$	120	120	Volmer
$M - H_{ads} + H_3O^+ + e^-$	$\rightleftarrows$	$M + H_{2(g)} + H_2O$	40	120	Heyrovsky
$2M - H_{ads}$	$\rightleftarrows$	$2M + H_{2(g)}$	30	∞	Tafel

+0.35 V_{RHE} and at 0 V_{RHE} the Pt surface is fully covered by H atoms. UPD hydrogen is believed to be a proton laying below the surface electron plasma with the electron being in the conduction band and, thus, UPD hydrogen is strongly bounded to the surface and is not taking part in the HER as an intermediate [23].

It is thermodynamically not possible for UPD H to form H_2 when $E \geq 0$, since the M-to-H bond energy is higher than the $\frac{1}{2}H_2$ bond. The intermediate in the HER is the so-called overpotential deposited (OPD) H, which is deposited on the UPD H for $E < 0$ V_{RHE}.

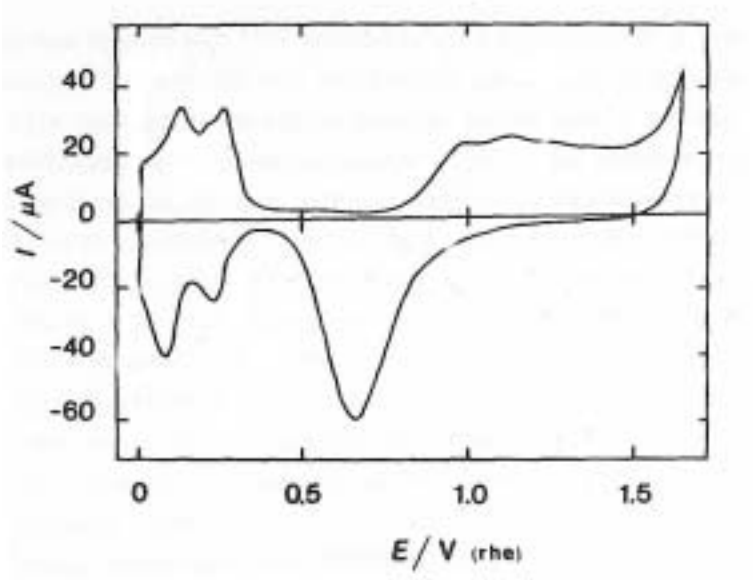

Figure 2.7: Voltammogram of Pt in 1.0 M H_2SO_4 solution [24].

The HER on Pt is strongly influenced by the crystallographic orientation of the surface where the (110) plane provides the highest activity towards the HER. However, the differences between the crystal planes are obscured by the diffusion of H_2 away from the supersaturated region and the differences are only visible under strong convection terms [25]. A voltammogram of Pt in 1.0 M H_2SO_4 solution can be seen in figure 2.7 [22] and shows the peaks of weakly and strongly adsorbed hydrogen at 0.12 and 0.25 V_{RHE} respectively. A third pair of peaks may also exist on Pt resulting from H-subsurface states located at 0.05 and 0.22 V_{RHE} of the cathodic and anodic peak respectively and is believed to arise from adsorbates participating as intermediates in the HER [26]. The different crystal faces on Pt provides different adsorption properties [27]. The Pt(111) provides a long-range adsorption site, the Pt(100) provides both long- and short-range ordered sites and the Pt(110) provides a short-range adsorption site.

2.4.2 The oxygen evolution reaction (OER)

The OER will mainly be discussed under the assumption that oxides of iridium or ruthenium are the active catalysts, since other materials such as Ni, Co, Mn

and other transition metals, undergoes corrosion in acidic media. Their cations are known to poison the membrane by attaching to the sulphonic clusters and reducing the conductivity of the membrane, and to strongly adsorb to the active sites at the Pt-cathode and further deactivate electrode [28].

The OER is a very complex reaction. The standard potential for the oxygen electrode is 1.23 V_{RHE} and falls above the standard potentials of almost all the solid elements and only a few materials can be considered stable in acidic solution. The OER involve complex pathways of high activation energy and high energetic intermediates [13]. On a bare metal, oxygen species covers the metal surface by UPD by discharge of water before the liberation of O_2 and since the M-O bond strength (M=metal) always is stronger than the O-O dissociation energy, the OER always takes place at an oxide surface. This includes oxide phase formation on the metal surface by formation and breakage of new bonds between the oxygenated species and the surface metal ions during the anodic reaction [29]. Thus, the catalysis of the OER involve a material process and is not a simple surface process, which may explain the very low exchange current density of the reaction (typically $1 \cdot 10^{-10}$ - $1 \cdot 10^{-11}$A/cm^2) and why the reversible potential of 1.23 V_{RHE} at room temperature never is obtained.

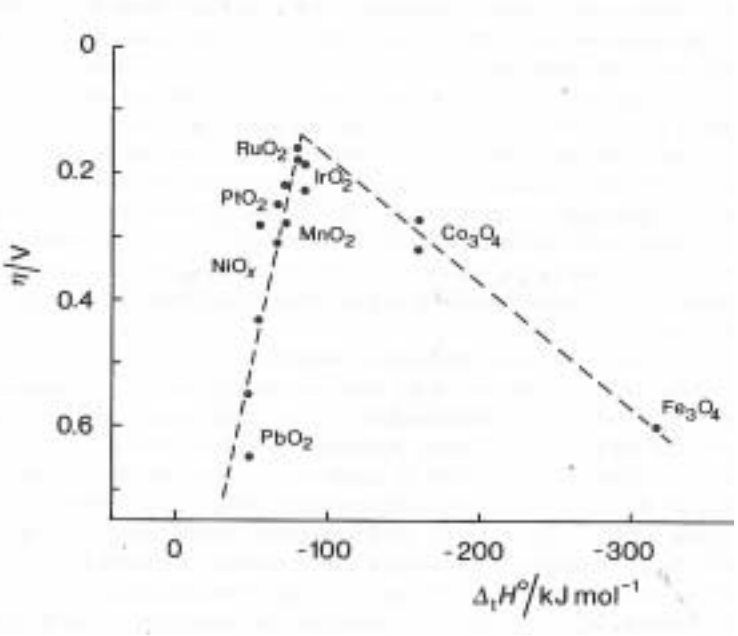

Figure 2.8: Overpotential at 0.1 mA·cm^{-2} on different metal oxides as a function of enthalpy of transition from lower to higher oxide [29].

Vulcano plots for the OER shows the correlation of the catalytic activity, in terms

of η or $\log(\mathrm{i})$, correlated by some energetic parameter, specific for each material. The activation energy for the homomolecular isotopic O_2 exchange in the gas phase has been shown to correlate the enthalpy of formation from a lower to a higher oxidation state and both parameters have been applied to construct a so-called Vulcano plot as can be seen in figure 2.8. These plots identify the oxides of Ru and Ir (and Os) as the most active catalyst towards the OER, which are also stable in acidic environment. What governs the catalytic activity of different materials towards the OER is their easiness of changing between lower and higher oxidation state from which O_2 is liberated. The potential of this redox couple should be as close to the onset of the OER as possible. If the redox potential is too low the oxide is oxidized too easily and may become non-catalytic active and a too high redox potential may lead to high overpotentials [30]. Oxygen adsorption starts at lower anodic potentials the stronger the M-O bond strength is, and a high M-O bond strength may cause anodic dissolution. The OER is believed to take place with a low coverage of adsorbed intermediates [31].

J. O'M Bockris [32] provided a method for evaluating kinetic expression of electrode reactions, where several intermediate steps are involved, and applied this method to study different paths of the OER and many different possible paths and rate expressions for the OER have been listed within this reference. Among these paths are the Electrochemical Oxide Path and the Oxide Path which has been suggested to occur on iridium and ruthenium oxide coatings [33, 34, 35, 30]. In equations 2.41 to 2.50, S denotes an active site.

I. The Electrochemical Oxide Path [32]:

$$\begin{aligned} \mathrm{S} + \mathrm{H_2O} &\rightleftarrows \mathrm{S-OH_{ads}} + \mathrm{H^+} + \mathrm{e^-} && (2.41)\\ \mathrm{S-OH_{ads}} &\rightleftarrows \mathrm{S-O} + \mathrm{H^+} + \mathrm{e^-} && (2.42)\\ \mathrm{2S-O} &\rightarrow \mathrm{2S} + \mathrm{O_{2(g)}} && (2.43) \end{aligned}$$

II. The Oxide Path [32]:

$$\begin{aligned} \mathrm{S} + \mathrm{H_2O} &\rightleftarrows \mathrm{S-OH_{ads}} + \mathrm{H^+} + \mathrm{e^-} && (2.44)\\ \mathrm{2S-OH_{ads}} &\rightleftarrows \mathrm{S-O} + \mathrm{S} + \mathrm{H_2O} && (2.45)\\ \mathrm{2S-O} &\rightarrow \mathrm{2S} + \mathrm{O_{2(g)}} && (2.46) \end{aligned}$$

III. The Krasil'shchikov Path [36]:

$$\mathrm{S} + \mathrm{H_2O} \rightleftarrows \mathrm{S-OH_{ads}} + \mathrm{H^+} + \mathrm{e^-} \tag{2.47}$$
$$\mathrm{S-OH_{ads}} \rightleftarrows \mathrm{S-O^-} + \mathrm{H^+} \tag{2.48}$$
$$\mathrm{S-O^-} \rightleftarrows \mathrm{S-O} + \mathrm{e^-} \tag{2.49}$$
$$\mathrm{2S-O} \rightarrow \mathrm{2S} + \mathrm{O_{2(g)}} \tag{2.50}$$

Table 2.4: Summary of Tafel slopes for different paths in the OER [37, 32].

Path	Step	b_a low η ($mV \cdot dec^{-1}$)	b_a high η ($mV \cdot dec^{-1}$)	ν_{H^+}
I.	2.41	120	120	2
	2.42	40	120	2
	2.43	15	∞	1
II.	2.44	120	120	4
	2.45	30	∞	2
	2.46	15	∞	1
III.	2.47	120	120	2
	2.48	60	60	2
	2.49	30	120	2
	2.50	30	∞	1

A Tafel slope of 15 $mV \cdot dec^{-1}$ have never been reported for the OER. The Tafel slope is usually 40 or 60 $mV \cdot dec^{-1}$ at low η and 120 $mV \cdot dec^{-1}$ at high η as $\theta \rightarrow 1$. A change in Tafel slope from a low to high value can take place when going from low to high overpotentials due to a change in reaction mechanism, to increasing surface coverage or to a change of rds within the same reaction mechanism [15]. A rather sharp transition from low to high b_a can be observed when a change in the rds take place [30].

In general, the oxide surface is covered initially by a carpet of OH-groups by discharge of water, which are further oxidized by ejection of H^+ and electrons along with an increase in the valence state of the metal ion. This creates an unstable higher valence oxide which decomposes when liberating oxygen gas and may require rearrangement of the surface. Oxides which are further oxidized with difficulty, adsorb the intermediate too weakly and water discharge becomes the rate determining step. Oxides which are oxidized too easily, however, adsorb the intermediate too strongly and removal of oxygenated species becomes the rate determining step [29]. As the affinity towards oxygenated species increase (increasing valence of the metal ion), the rate determining step moves further down

the route and the Tafel slope decreases accordingly. Too high affinity towards oxygenated species, however, will cause the release of oxygen gas to become rate determining and a limiting current density will be observed [38].

The density of active site of metal oxides influences the kinetics of the OER. High density of active sites facilitates the rearrangement step to proceed with ease, and the recombination step with a low Tafel slope becomes the rds. For lower density of active sites, the rearrangement step becomes the rds and an increase in Tafel slope will take place. This can be observed by increasing the preparation temperature of the oxide where the Tafel slope increases from 30 $\mathrm{mV} \cdot \mathrm{dec}^{-1}$ for highly defective electrodes prepared at low temperatures, to 60 $\mathrm{mV} \cdot \mathrm{dec}^{-1}$ for less defective electrodes prepared at higher temperatures [30]. This is because the crystallite size increases by increasing temperature and that the OER changes from taking place on corners and cracks of the crystallites to taking place on the crystal faces where there are longer distance between the active sites. However, this can also be explained by increasing stoichiometry with decreasing number of active sites in terms of defects. For slow adsorption and discharge of water, the first step becomes rate determining and the Tafel slope becomes 120 $\mathrm{mV} \cdot \mathrm{dec}^{-1}$.

2.5 Noble metal oxides

Structure

The oxides of Ir and Ru are tetragonal and isomorphous with rutile structure, which posses metal-like conductivity [39]. The rutile structure is shown in figure 2.9. In the rutile structure every cation is almost octahedrally surrounded by anions which are oriented along the set of rectangular coordinate axis, and every anion is trigonally surrounded by cations.

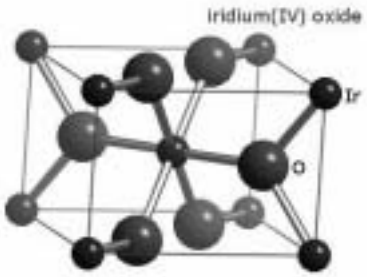

Figure 2.9: Unit cell of a rutile structure.

The coordination number of the oxide ion increase as the calcination temperature is increased and attain 6, which is the theoretical value of the standard samples of rutile IrO_2 and RuO_2 [40]. Upon heat treatment of RuO_2 the a-axis decreases while the c-axis increases at increasing temperature [40]. Both oxides are slightly non-stoichiometric, the oxide of Ru is oxygen deficient and the oxide of Ir has an excess of oxygen [41].

Electrical conductivity

IrO_2 and RuO_2 possesses metallic conductivity with electrical resistivities of $6 \cdot 10^{-5}$ and $5 \cdot 10^{-5}$ $\Omega \cdot$ cm respectively measured at 300 K [39]. In a crystalline rutile state, the electron energy of the d-level of the metal cation is split into $3e_g$ and $3t_{2g}$ sublevels which are further split and broadened due to unequal length in two of the six cationic ligands which are orientated in the c-axis. IrO_2 and RuO_2 occupy only partly the t states with 5 and 4 electrons respectively and the c-axis is quite extended (see table C.1). Thus, the orbitals become relatively spread out in space and facilitate the excitation of electrons from valence band to conduction band. This is why crystalline IrO_2 and RuO_2 exhibit such excellent metallic conductivity [42].

Electronic conductivity is also present in the more amorphous hydroxides of lower average valence, however, the conductivity is more of a semiconductor character. Gottesfeld *et* al. [38] showed by ellipsometric measurements that the thick hydrous oxide layer on Ir exhibit semiconducting properties. Burke *et* al. [43] suggested a p-type semiconductor behaviour by an electron hopping process with the generation and diffusion of higher valence states, i.e. Ir(IV) sentras, picking up electrons at the metal/metal oxide interface. Introducing defects into the oxide structure may enhance the electrical conductivity of amorphous oxides, however, for crystalline oxides distortion of the crystal lattice may affect the band width and decrease the electrical conductivity [41]. Most electrodes of metal oxides probably exhibit some

intermediate properties between the crystalline and amorphous state depending of the crystalline degree of the oxide.

Electron conduction in the oxides of Ir and Ru takes place by a "hopping" mechanism from grain to grain while the grain boundaries possesses increased electrical resistivity [41]. Thus, electrical conductivity of the oxides will also depend on crystallite size and how compact the grains are. Further decrease in electrical conductivity may be caused by residual Cl from the precursors and thereby expansion of the lattice, and by segregation of impurities to the grain boundaries (Ir metal or insulating Ir_2O_3) [44].

Acid-base properties

Metal oxides react with water, and become covered by a carpet of OH-groups, which determine the interfacial properties of the oxide surface towards the solution. Water molecules are adsorbed onto the metal cation while a proton from each water molecule becomes transferred to a neighbouring oxygen atom in the oxide lattice [44], illustrated in figure 2.10. The OH-groups at the oxide surface give rise to Lewis acid/base properties according to equation 2.51 where S is an adsorption site.

$$SO^- + H_2O \quad \overset{\text{acid}}{\underset{OH^-}{\longleftarrow}} \quad SOH \quad \overset{\text{base}}{\underset{H^+}{\longrightarrow}} \quad SOH_2^+ \tag{2.51}$$

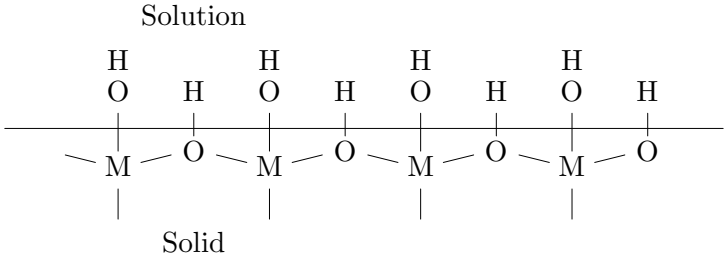

Figure 2.10: The oxide/solution interface.

Metal ions of high electronegativity withdraw electrons from the OH-group and thereby weaken the O-H bond (H^+ is more easily released) and the metal oxide act as an acid, whereas metal ions of low electronegativity tend to push back the electrons to the OH group and weaken the M-OH bond and the metal oxide may act as a base. The point of zero charge (pzc), at which pH the surface is neutrally charged, pH_z, determines the acid/base properties of an oxide. On IrO_2

pzc is found for pH< 1 whereas on RuO_2 pzc is found for pH∼6, which can be explained by the higher electroneutrality of the Ir metal At pH < pH_z the surface is positively charged and at pH > pH_z the surface is negatively charged. pzc is a parameter very sensitive to the surface state and can be used to separate geometric and electronic effects and is expected to correlate with the catalytic activity of metal oxides. The metal oxides tend to become more hydrophobic at higher temperatures of calcination [44].

Voltammetry on IrO_2 and RuO_2 electrodes

Voltammetry is very useful for determination of the surface state of metal oxides[2]. Typical voltammograms of IrO_2 and RuO_2 prepared by standard DSA technique[3] and measured in 0.5 M H_2SO_4 at room temperature are shown in figure 2.11 and 2.12 respectively. The metal ion is undergoing continuous redox transition as oxygenated species are adsorbed and further oxidized balanced by ejection of protons and electrons. The reversibility of the redox transitions of oxides of Ir and Ru between lower and higher valence can be understood from the respective voltammograms by the symmetry of the anodic and cathodic peaks. Michell *et* al. [45] have proposed a general electrochemical oxidation process which gives rise to the peaks of iridium oxide:

$$IrO_a(OH)_b \rightleftarrows IrO_{(a+\delta)}(OH)_{(b-\delta)} + \delta H^+ + \delta e^- \tag{2.52}$$

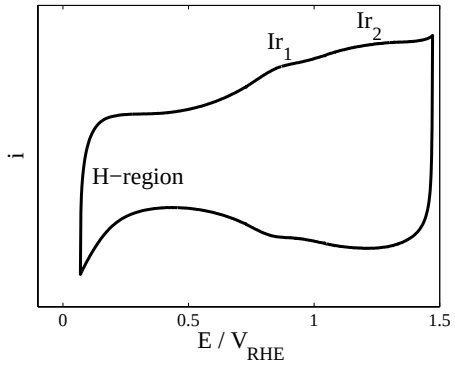

Figure 2.11: Voltammogram of IrO_2.

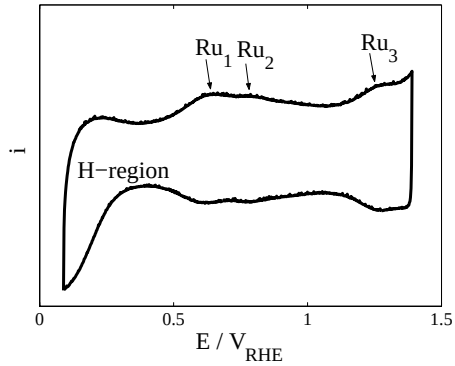

Figure 2.12: Voltammogram of RuO_2.

The hydrogen region, where underpotential deposition (UPD) and desorption of H takes place, is located at potentials below 0.4 V_{RHE}. At potentials above 0.4 V_{RHE}, adsorption of OH-goups and further oxidation to oxygenated species takes place. The two peaks in the voltammogram of IrO_2 denoted Ir_1 and Ir_2 at 0.93 and 1.35 V_{RHE} corresponds to the redox couples Ir(III)/Ir(IV) and Ir(IV)/Ir(VI)

[2] see section 2.3.2
[3] see section 3.2

respectively [33]. The redox transition between Ir(III) and Ir(IV) can be described by equation 2.52 when a = 1, b = 1 and $\delta = 1$ and the redox transition between Ir(IV) and Ir(VI) when a = 1, b = 2 and $\delta = 2$. The standard potential of transformation of the oxide from Ir_2O_3 to IrO_2 is reported to take place at 0.926 V_{RHE} [46], whereas redox reaction at 1.35 V_{RHE} is reported to take place together with the onset of O_2 [33]. The Ir(V) state has also been observed, however, only in basic media [47]. Corrosion on IrO_2 take place according to reaction 2.53 in parallel with evolution of O_2 [33].

$$IrO_3 + H_2O \rightarrow IrO_4^{2-} + 2H^+ \tag{2.53}$$

The general charging process on RuO_2 electrodes has been described by equation 2.54 [45]:

$$RuO_x(H_2O)_y \rightleftarrows RuO_{(x+\delta)}(H_2O)_{(y-\delta)} + 2\delta H^+ + 2\delta e^- \tag{2.54}$$

A voltammogram of RuO_2 prepared by the DSA technique is shown in figure 2.12. The hydrogen region is located below 0.4 V_{RHE} and adsorption of oxygenated species takes place at potentials above 0.4 V_{RHE}. The peaks Ru_1 and Ru_2 has been attributed to the redox couples Ru(II)/Ru(III) and Ru(III)/Ru(IV) respectively and the peak Ru_3 to the redox couple Ru(IV)/Ru(VI) [48, 49].

Whereas the highest possible valence state of the Ir oxide is Ir(VI), the oxide of Ru can be oxidized to Ru(VIII). The corrosion of the RuO_2 electrode during OER is related to the initial stability of the $RuO_2(OH)_2$ species which is oxidized to the thermodynamically unstable RuO_4, shown in equation 2.55 and 2.56. RuO_4 can either liberate O_2 according to equation 2.57, or formation of volatile RuO_4 or hydrous $RuO_2 \cdot 2H_2O$ can take place according to reaction 2.58 and 2.59 respectively [48].

$$RuO_2(OH)_2 \rightarrow RuO_3(OH) + H^+ + e^- \tag{2.55}$$

$$RuO_3(OH) \rightarrow RuO_4 \tag{2.56}$$

$$RuO_4 + H_2O \rightarrow RuO_2(OH)_2 + 1/2O_{2(g)} \tag{2.57}$$

$$RuO_4 \rightarrow RuO_{4(g)} \tag{2.58}$$

$$RuO_4 + H_2O \rightarrow H_2RuO_5 \rightarrow RuO_2 \cdot 2H_2O + O_{2(g)} \tag{2.59}$$

Voltammograms recorded on metallic surfaces of Ir and Ru are quite similar to that of Pt, showing strong and weak adsorption peaks of UPD H atoms and irreversible oxide peaks. On continuous cycling the voltammetric current increases due to formation of a thick oxide film and the oxide peaks becomes reversible in nature. On Ir, the hydrogen region remain as a thin tail of the voltammogram and is little altered during cycling [43], whereas on Ru also the hydrogen region is broadened on continuous cycling [45].

Oxides of Ir and Ru are able to conduct protons by a Grøtthus hopping mechanism via OH^- and O^{2-} sites. The anodically formed oxides are essentially hydroxides and the entire mass is permeable to protons and they provide an environment similar to an ionic solution. Thus, on anodically formed oxide the entire oxide mass is believed to be involved in the charging reactions, whereas on thermally prepared oxide only sites along crystallite boundaries, crevices, pores and cracks are available and the charging reactions 2.54 are limited by proton diffusion at the boundary interfaces [50, 51]. Anodically formed oxides therefore facilitates a larger surface area available for reaction and they are in general more catalytic active towards the OER, compared to thermally formed oxides, however, due to oxygen bridging thermally formed oxides are more stable and a compromise must be found between activity and stability [30].

AC-impedance on IrO_2 and RuO_2 electrodes

The impedance of IrO_2 and RuO_2 based electrodes during O_2 evolution is characterized by a transmission line of infinite length type of behaviour in the high frequency region and a Faradaic time constant in the low frequency region. The high frequency part shows a straight line close to 45° and and have been attributed to the intrinsic properties of the oxide. Burrows *et* al. [52] studied RuO_2/TiO_2 electrodes and assigned the high frequency behaviour to that the ac-signal reached the bottom of the pore. Glarum *et* al. [53] studied anodically grown hydroxide on Ir and attributed the high frequency response to diffusion of reduced lattice sites through a layer of finite thickness, balanced by hydrogen ion exchange within the pores. Rishpon *et* al. [54] attribute the high frequency response to diffusion of protons along oxide grains on thermally prepared oxide of Ru, i.e. diffusion in a a layer of finite thickness. Lassali *et* al. [55] found that the contribution of the transmission line behaviour became less important at higher firing temperature and attributed this effect to the formation of a more crystalline and less amorphous oxide, where the amorphous oxide constituted the difficulty to access region.

The impedance of IrO_2 based electrodes, prepared as DSA electrodes, have been fitted to a circuit represented by $R_\Omega(RQ)(R_{ct}Q_{dl})L$ [55, 56, 57]. R_Ω was attributed to the ohmic resistance, R to the insulating TiO_2 interlayer between the substrate and the catalytic film, R_{ct} to the charge transfer resistance and L to inductance. Q and Q_{dl} are constant phase elements given by equation 2.39. The (RQ) combination takes into account the properties of the oxide layer and the ($R_{ct}Q_{dl}$) combination is attributed to the charge transfer reaction of the OER [57]. L originates from the instrumentation, i.e. cables and connectors.

2.6 Adams fusion method

Platinum oxide prepared by fusion of chloroplatinic acid and sodium nitrate was first described by R. Adams *et* al. [58]. During the fusion process nitrogen dioxide is evolved and platinum oxide is precipitated. The reaction mechanism was assumed to be as follows:

$$6NaNO_3 + H_2PtCl_6 \rightarrow 6NaCl + Pt(NO_3)_4 + 2HNO_3 \quad (2.60)$$

$$Pt(NO_3)_4 \rightarrow PtO_2 + 4NO_2 + O_2 \quad (2.61)$$

The process is typically carried out in the temperature range 300 - 600 °C. This procedure may also be applied to prepare IrO_2 and RuO_2 using their respective chloride salts.

2.7 The polymer membrane

The solid polymer electrolyte (SPE® is the registered trademark of Hamilton Sundstrand), also referred to as the proton exchange membrane (PEM), are attractive as electrolytes for fuel cells and water electrolysers due to their high mechanical, chemical and thermal stability, high ionic conductivity and low permability to H_2 and O_2 gases.

The perfluorosulfonated ionomer (PFSI) membrane consists of a polytetrafluoroethylene backbone and perfluoronated pendant side chains terminated by sulphonic groups. The perflouronated carbon backbone chain is responsible for the mechanical and thermal stability of these membranes and the sulphonic ionic groups are responsible for the ionic conductivity. These membrane types have been developed for the chlor-alkali industry and several types of commercial membranes are available on the marked including Nafion® (DuPoint), Dow membrane (Dow Chemical), Flemion® (Asahi Glass Company), Aciplex® -S (Asahi Chemical Industry), Neosepta-F® (Tokuyama), Gore-Select® (W. L. Gore Associates, Inc.) among others [7]. The thickness of the membranes ranges from about 20 to 200 μm.

The sulfonated perfluorinated polymers are rather expensive and extensive research are carried out on cheaper membranes. Sulphonated hydrocarbons of aromatic rings (PBI, PEEK) are cheaper than perfluorinated membranes and can withstand higher temperatures due to higher water uptake and are attractive in methanol fuel cells [7]. Radiation-grafted membranes represent a simple method for introducing sulphonic groups into cheap commercially available materials (PVDF, PTFE) by first irradiation followed by grafting [59, 60]. However,

the Nafion® membrane is today the most available type of membrane and is commonly used in fuel cell- and electrolysis-research.

The polymer structures of the Nafion® membrane from DuPoint and of the Dow Chemicals membrane can be seen in figure 2.13. The different PFSI membranes typically differ in length of repetitive units of the carbon backbone and in length of the side groups.

DuPont Nafion®

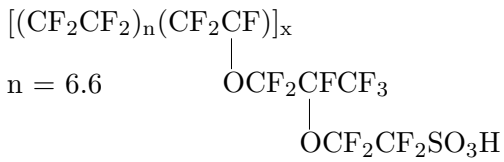

Dow Chemicals

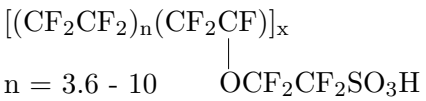

Figure 2.13: Structure of perfluorosulfonated ionomer membranes

A model of the microstructure of PFSI membranes were proposed by Gierke *et* al. [61] who described the membrane as a series of ionic clusters or inverted micelles of about 40 Å in diameter in the hydrated state separated from the perfluorinated polymer backbone. The clusters were believed to be interconnected by narrow channels of about 10 Å. Swelling of the membrane take place for increasing water content and figure 2.14 shows how the ion exchange sites redistribute upon dehydration. The primary hydration shell of the SO_3H group is six water molecules, and the ionic conductivity of the membrane increases significantly when the average number of water molecules per sulfonic acid group increases to more than six [62].

The membrane water content is defined by the number of mole of water per moles of sulfonic group:

$$\lambda = \frac{n_{H_2O}}{n_{SO_3^-}} \tag{2.62}$$

where n is number of moles. The ionic conductivity increases for increasing λ and reaches a value of 18 for 100% relative humidity (RH) under fuel cell operation and approximately 22 when the membrane is swollen in water [63]. When proton transport through the membrane take place, a certain number of water molecules are transferred per H^+ ion by electro-osmotic drag. The drag coefficient, ξ, has been found to be about 1 H_2O/H^+ and independent of current density for less than 100 % humidification and 2 - 3 H_2O/H^+ for a Nafion® membrane swollen

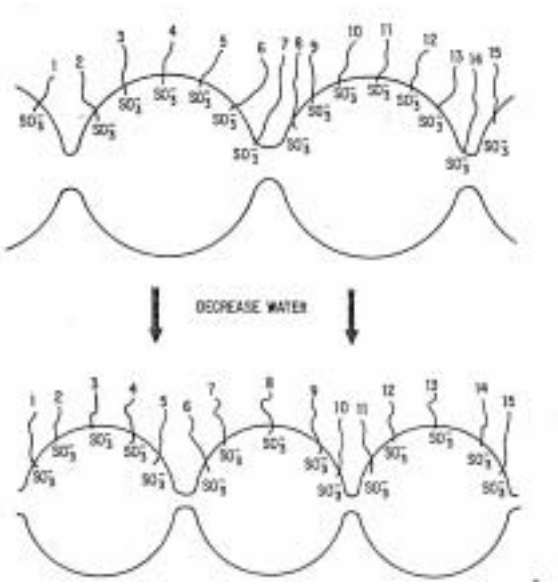

Figure 2.14: Sketch of rearrangement of ionic cluster upon dehydration of polymer [61].

in water [63]. The equivalent weight (EW) is defined as weight of polymer per sulfonic group and a lower EW represent more sulfonic groups and higher specific ionic conductivity of the polymer. Thickness, resistance and EW of different commercial membranes are given in table 2.5.

Table 2.5: Ionic conductivity, EW and thickness data of different membranes.

Commersial trade name	Thickness (μm)	EW ($g \cdot mole^{-1}$ SO_3^-)	Resistance ($\Omega \cdot cm^2$)	Ref.
Nafion® -112	50	1100	0.036	[64]
Nafion® -115	125	1100	0.168	[65]
Nafion® -117	175	1100	0.23	[66]
Flemion® S	80	1000	0.10	[7, 66]
Aciplex® -S	120	1000	0.111	[65]
Dow	120	800	0.110	[65]
Gore-Select™	20	900	0.03	[64]

A lower specific conductivity of the membrane can be accepted if the system allow the use of thinner membranes. However, membrane type must be chosen according to the specific system. Gas permeation and risk of membrane destruction must also be taken into account. K. Broka *et* al. [67] studied H_2 and O_2 permeability of Nafion® -117 membranes and found that the gas permeability increased for

increasing temperature and for increasing RH. The H_2-permeability was found to increase from about 8 to 22 $\cdot 10^{-12}$ mol $\cdot$ cm^{-1} $\cdot$ s^{-1} and the O_2-permeability increased from about 9 to 13 $\cdot 10^{-12}$ mol$\cdot$cm$^{-1}\cdot$s^{-1} when the temperature increased from 20 to 80 °C. Yoshida *et* al. [66] found that gas permeation of different membrane types was determined by the thickness of the membrane and that the permeation was inverse proportional to the thickness.

Chapter 3

Literature review

3.1 Water electrolysis using solid polymer electrolyte

The first water electrolyser using polymer membrane as electrolyte was first developed by the General Electric Company in 1966 for space applications [6]. The production and development of SPE® electrolysers was in 1984 purchased by Hamilton Sundstrand, a subsidiary of United Technologies Corporation. Several research groups have started working with SPE® electrolysis, and today a few companies are in commercial business. Relatively few papers have been published during the last few years, and much of the research on SPE® electrolysis is carried out in connection to regenerative fuel cell technology.

The physical and chemical properties of the catalysts determine the most important characteristics of the system, i.e. service life, energy consumption and current density. The choice of catalyst preparation in SPE® electrolysis will depend on how the preparation procedure of membrane electrode assemblies (MEAs) is carried out. The preparation of MEAs must facilitate:

- Good adhesion of the catalyst to the membrane.
- Low resistivity between the catalytic layer and the membrane.
- A three dimensional reaction zone where reactant, electrolyte and electrons are brought together.
- A structure that allow easy transport of water and gas to and from the catalytically active zone.
- A certain percolation path to obtain high electrical conductivity of the layer [68].
- Easy release of gas bubbles.

In Grenoble in France, Millet *et* al. [69] developed a procedure for preparation of composites for SPE® water electrolysis by precipitation of noble metal particles at the surface of a polymer membrane by chemical reduction of cationic precursor salts, i.e. $Pt(NH_3)_4Cl_3$ and $NaBH_4$ as reducing agent (French patent, 1987). Cell voltage of 1.75 V at 1 $A \cdot cm^{-2}$ and 80°C was obtained for a Pt/Nafion/Pt-Ir composite using relatively low loading of noble metals of 1 $mg \cdot cm^{-2}$ Pt and 0.2 $mg \cdot cm^{-2}$ Ir. Precipitation of metallic Ru, instead of Ir, resulted in a very short service life of the electrode, where Ru became dissolved and precipitated within the membrane as isolated clusters. Continuous operation of a Pt/Nafion/Pt composites of more than 15000 hours were reported at current densities from 0.5 to 1 $A \cdot cm^{-2}$ with no degradation of performance. Metallic Ir and Ru was found to be too unstable for long time operation [70]. Loss in performance of the composites was attributed to Ni ions detected in the feed water, which caused poisoning at the cathode and decreased the membrane conductivity. Etching the surface of the membrane to achieve roughness gave no significant improvement and pressurizing the system had very little influence on the performance [70].

RuO_2 was compared to Pt as cathode catalyst in SPE® electrolysis by Michas *et* al. [71] where the RuO_2 electrode was prepared by thermal precipitation of noble metal chloride precursor onto a porous sheet of titanium and the Pt electrode was prepared by chemical reduction onto the membrane. The RuO_2 catalyst was found to be insensitive to poisoning by Cu^{2+}. However, at current densities up to 1 $A \cdot cm^{-2}$, the cathodic overvoltage of the RuO_2 electrode was about 300 mV higher compared to the Pt electrode.

Andolfatto *et* al. [28] prepared IrO_2 electrodes by thermal precipitation of noble metal chloride precursor on to a porous sheet of titanium, followed by impregnation with Nafion® ionomer and hot pressing onto the membrane. Metal cations were found in the feed water of a 0.4 kW system due to corrosion of steel pipes, which caused degradation of the cell performance. IrO_2 was tested as anode catalyst and as cathode catalyst, since IrO_2 is insensitive to UPD of metal cations at negative potentials. More stable performance was obtained compared to the Pt cathode. However, IrO_2 possessed only a moderate activity towards the HER and purification of the water was still necessary to avoid contamination of the membrane and a further decrease in the membrane conductivity.

Research and development on SPE® electrolysers have been quite extensive during the last two decades at research laboratories in Osaka, Japan, implemented within the World Energy Network (WE-NET) program and the Agency of Industrial Science and Technology (AIST) [72]. Mori *et* al. [73] investigated a method for chemical plating of metallic Ir onto a Pt/Membrane/Pt composite (Japanese patent [74]). They found that the complex $Ir(N_2H_5)Cl_5^-$ served well as precursor when reduced by N_2H_4 at pH = 3 and below. When using a loading of 1.5-2 Ir $mg \cdot cm^{-2}$, a cell voltage of 1.68 V at 80°C and 1 $A \cdot cm^{-2}$ was obtained on a 50 cm^2 of active area single cell using Nafion® -117.

Inazumi *et* al. [75] investigated the long term stability of 4 single cells in electrolysis mode, prepared by the same method as Mori *et* al. [73], and found that the degradation of the cell voltage was caused by accumulation of Ni, Fe and Cr ions within membrane. The increase in cell voltage was found to be proportional to the content of accumulated cations in the membrane. Gas impurity was also found to increase by the increased content of cations. An increase in cell voltage by 0.2 V was observed after 200 days at operation condition of 1-1.5 $A \cdot cm^{-2}$ and 80°C. Original performance was established by flushing the MEA in 4 N HCl at 365 K for 1 h. The presence of metal ions was believed to arise from corrosion of stainless steel components of the cell.

Sakai *et* al. [76] investigated the effect of surface roughening by different sputtering methods of Nafion® -117 membranes in SPE® electrolysis using the same preparation method as Mori *et* al. [73]. They found that roughening of the membrane surface caused gas bubbles to be released more easily, which improved the gas purity and lowered the resistance of the membrane due to the presence of less bubble inside the catalytic layer during operation. Although the mechanical strength of the membrane decreased by the sputtering process, the membrane maintained its initial strength after electrolysis, as opposed to membranes not pretreated by sputtering. However, sputtering had no influence on the roughness factor of the Pt electrodes.

Kondoh *et* al. [77] tested two SPE® electrolysis modules of 0.25 m^2x10 cell stack using Nafion® -117 membrane and the same preparation procedure as Mori *et* al. [73]. The first module was tested for long term stability at 80°C and maintained stable performance during 2500 hours at 1 $A \cdot cm^{-2}$ and then during 2500 hours at 2 $A \cdot cm^{-2}$ at an average cell voltage of 1.74 V and 1.9 V respectively. For the second module, an improved plating bath resulted in an average cell voltage of 1.73 V at 1 $A \cdot cm^{-2}$ and improved current efficiency of 98.3 % was obtained at same operating conditions. A piece of 5 cm^2 was cut out from the 0.25 m^2 composite and tested in a small laboratory cell at temperatures up to 100 °C. A cell voltage of 1.68 V 1 $A \cdot cm^{-2}$ was obtained at 98.3 % current efficiency, which gave a specific energy consumption of 4.1 kWh/Nm^3 H_2. Anode current collector was of sintered titanium and cathode current collector of sintered carbon.

Ioroi *et* al. [78] prepared bi-functional electrodes for a regenerative fuel cell system, which was operated in both fuel cell and water electrolysis mode using a total loading of 8-10 $mg \cdot cm^{-2}$ and Nafion® -115 membrane. IrO_2 was synthesised in aqueous solution followed by heating in air at 400 °C for 1 hour. The resulting catalyst obtained high specific surface area of 38 $m^2 \cdot g^{-1}$. The electrodes were prepared by mixing the O_2 catalyst (IrO_2 and Pt-black) with Nafion® -ionomer and the H_2 catalyst (Pt-black) with 20 % PFTE. Solvent was evaporated and the electrodes were hot-pressed into the membrane. The best round trip efficiency, $\epsilon_{R.T.} = U_{FC}/U_{WE}$ of 49 % was obtained when IrO_2 content of the O_2 electrode was 10-30 mole%. The best water electrolysis performance obtained was approx-

imately 1.74 V at 1 $A \cdot cm^{-2}$ and 80 °C with an IrO_2 content of 50 mole% .

Yamaguchi *et* al. [79] obtained 1.533 and 1.665 V at 1 and 3 $A \cdot cm^{-2}$ respectively and 80 °C using 3 mg IrO_2 per cm^2 and 0.5 mg Pt per cm^2. The electrode area was 50 cm^2 and the membrane of B2-type with 51 μm thickness and EW=1000. The electrodes were prepared by a hot-pressing procedure. Anode current collector was Ti-sinter electroplated with Pt and cathode current collector was a goldplated stainless steel sinter. The same group [80] operated later a 0.25 m^2 single cell SPE® electrolyser at 1.54 V, 80°C and 1 $A \cdot cm^{-2}$ using similar catalysts and conditions. The target within the WE-NET program is to obtain electrodes of 1 m^2 active area able to operate from 1-3 $A \cdot cm^{-2}$ at energy efficiency ($\varepsilon_{\Delta H}$) of more than 90 % (U_{cell} lower than 1.64 V at 3 $A \cdot cm^{-2}$ and 90 °C.).

At Fraunhofer-Institute for Solar Energy Systems in Freiburg in Germany extensive research and development of SPE® electrolysers and regenerative fuel cells has been carried out. Cell voltage at 1.73 and 1.90 V was obtained at 1 and 2 $A \cdot cm^{-2}$ respectively at 80 °C in a SPE® electrolyser using 4 $mg \cdot cm^{-2}$ of Pt at the cathode and 4 $mg \cdot cm^{-2}$ of Ir at the anode, the latter prepared by a sputtering process on to the anode current collector [81]. A life time of 3000 h was obtained without any degradation of performance. Current densities up to 10 $A \cdot cm^{-2}$ was realized without transport limitations for an electrode of 1 cm^2 active area and without any severe corrosion problems. Even higher current densities up to 25 $A \cdot cm^{-2}$ and linear current voltage relationship has been reported [82]. In the Dr. thesis by Mahlendorf [83], the best anode catalyst was reported to be the binary oxide catalyst of $Ir_{0.5}Ru_{0.5}O_2$ where 1.71 V in cell voltage was obtained at 1 $A \cdot cm^{-2}$ and 80 °C using Nafion® -117, 4 $mg \cdot cm^{-2}$ Pt as cathode catalyst and 4 $mg \cdot cm^{-2}$ of the anode catalyst. At 10 $A \cdot cm^{-2}$ the cell voltage was measured to be 3.14 V using the same composite at the same temperature. The oxide catalyst was prepared by thermal oxidation of the chloride salts in alcoholic solution followed by grinding in a vibrator mill until a particle size of 1-2 μm was obtained.

ABB in Switzerland developed during the period 1976 to 1989 the commercial Membrel® electrolyser [84]. Two units of 100 kW were put in operation for long term testing and later disconnected for further analysis. Both units had to be shot down due to gas impurity problems, as H_2 in O_2 (and visa versa) reached the safety limit of 3 %. The first unit was stacked into four smaller units of 30 cells, which were compressed together by a hydraulic system. The cathode was prepared by depositing Pt on to the membrane by an electroforming technique, whereas the anode consisted of a PFTE bonded layer of mixed oxides of Ir and Ru on which was further deposited onto the porous Ti-current collectors. The cathode current collector was made by a PTFE bonded carbon composite on a brass wire mesh. During operation the cell voltage was in average 1.75 V at 1 $A \cdot cm^{-2}$ and 80°C. This unit was shot down after 15000 hours of operation and several cells had short-circuited. Severe thinning of the membranes was observed,

which showed a linear correlation with the ion exchange capacities and thereby excluding loss of ionic groups as the cause of thinning. In a lab experiment a cell was connected with 4 membranes between anode and cathode and the thickness of the individual membranes was measured after some time of operation. Only the membrane adjacent to the cathode showed severe thinning of approximately 50 % compared to the initial value, which revealed that the thinning of membranes occurred in connection to the cathode.

In case of the second unit, all 120 cells were stacked in series using a mechanical spring-system to compress the cells together to allow expansion during operation and the cathode catalyst was the same as the anode catalyst. This unit was shot down after 2300 hours of operation due to gas impurities. The cells of the first unit was replaced with new cells, using the same catalysts as the second unit. After 5500 hours of operation, no continuous increase in gas impurity had been detected. The authors suggested that chemical attack of the fluorinated polymer chain may have caused the thinning of the membranes:

$$-CF_2 - ... + 2H_2 \rightarrow ... - CH_2 - ... + 2HF \quad \Delta G < 0$$

Traces of fluoride ions was previously detected in laboratory cells. It was pointed out that the problems could be influenced by the mechanical compression system, as well as properties of the current collectors. The thinning of membrane was believed to be caused by mechanical stress from gas bubble nucleation as the pores of the cathode current collectors was smaller than the anode current collectors, which explained why the problem only occurred at the cathode side.

Titanium is reported to be used as a current collector at the anode side in almost all literature concerning SPE® electrolysis. Titanium has also been used throughout in the industry as anode-substrate for Cl_2 and O_2 evolving electrodes due to its high corrosion resistance at high potentials and acidic media [85]. Its low density, high electrical conductivity and its excellent mechanical properties and formability should make titanium attractive as construction material in the SPE® electrolysis system. Bipolar plates of titanium, prepared by a super plastic mold-forming process, have been reported to be suitable for large scale production at a remarkable low costs compared to traditional machining process [77]. Titanium has recently gained increasing interest as bipolar plate material in SPE® fuel cells as well [86, 87]. Unprotected titanium, however, may easily passivate by formation of an electrically insulating oxide layer and the titanium surface must therefore be coated or modified to obtain a protective layer which at the same time allow easy passage of electrons. Protection of titanium in SPE® cells has become an increasingly important area of research [88].

3.2 Noble metal oxides in industrial applications

In the mid 1960s the Dutch scientist Henry B. Beer described the properties and applications of noble metal oxides as electrocatalysts in a British patent [89]. Since then, the oxides of Ir and Ru have been widely used as active catalysts in so called dimensionally stable anodes (DSA®). RuO_2 has for many years been the prototype of DSA due to its excellent properties as chlorine evolving catalyst, however, IrO_2 is recognised to be more attractive towards the OER due to a better stability, despite a higher prize and lower activity compared to RuO_2 [90, 91]. The more fundamental aspects on noble metal oxides are given in section 2.5.

DSA electrodes are usually prepared by thermal deposition of metal chloride precursors onto a roughened substrate, preferably of Ti, however, Ta and Nb may also be possible materials. The substrate is first sandblastered and further etched in 10 - 20 % HCl or oxalic acid to obtain roughness and attachment of the catalytic layer to the substrate. The precursors, usually the chloride salt of the metals, are first dissolved in appropriate ratio in aqueous or organic solvents and then coated onto the substrate. The solvent is evaporated and the electrode is then heated in 350 - 600 °C from 5 to 15 minutes. This is repeated until desired catalyst loading is obtained. Finally the electrode is heated at the same temperature for 1 hour. The active catalysts of IrO_2 and RuO_2 are always mixed with some inert components, e.g. Ta_2O_5, TiO_2, SnO_2, Nb_2O_5, ZrO_2, to improve stability and selectivity and to modify the morphology [89, 92].

The mixed oxides of Ir and Ru is maybe the most promising anode catalyst in SPE® electrolysis. Kötz *et* al. [91] studied $Ru_xIr_{1-x}O_2$ electrodes prepared by a sputtering process onto a Ti substrate for different values of x. They found that for $x = 0.2$ the corrosion rate of RuO_2 decreased down to 4 % of the initial corrosion rate and that the corrosion rate of the of the composite approached the corrosion rate of pure IrO_2 for $x \geq 0.5$. This was explained by the formation of a common d-band and a lowering of the heat of interaction between RuO_2 and oxygen where the oxidation to RuO_4 was suppressed, which is the state of ruthenium oxide for which corrosion takes place [48]. The electrochemistry was mainly controlled by IrO_2 for $x \geq 0.5$. The Membrel® electrolyser, developed by this group, uses this catalyst at $0.5 \leq x \leq 0.8$ as the O_2 evolving electrode.

Mattos-Costa *et* al. [93] studied $Ru_xIr_{1-x}O_2$ coatings prepared by a sol-gel process in 0.5 M H_2SO_4 solution using etched Ti as substrate. This process provided chlorine free coatings and excellent correlation between the concentration of starting solution and composition of the resulting catalyst layer. They found that small additions of RuO_2 to IrO_2 greatly improved the stability of the catalytic layer compared to pure IrO_2 (in contradiction to Kötz *et* al. [91]). Best life time performance was obtained for $x = 0.1$ wheras the most active electrode was obtained for $x = 0.7$ attributed to catalytic- and roughness effects. Wen *et* al. [49] studied thermally prepared $Ru_xIr_{1-x}O_2$ coatings using chloride salt precursors and found

a maximum activity for x = 0.3.

The IrO_2-Ta_2O_5 system is one of the most promising catalysts in different electrochemical industries using DSAs, i.e. electrodes in cleaning of waste water [94] and electrowinning of metals [95, 96] where O_2 evolution is the main anodic reaction. Ta_2O_5 is mixed with IrO_2 mainly to improve the service life of the latter, which is the active catalyst and the most expensive component.

Comninellis *et* al. [85] studied different combinations of active catalyst and inert oxides prepared by the DSA technique and found that IrO_2 (70 mole%) - Ta_2O_5 (30 mole%) constituted the best choice from an economical point of view, where lifetime of the active catalyst was emphasized as the most important factor. Krýsa *et* al. [94] found 65-70 mole% IrO_2 as an optimum composition. The IrO_2 - Ta_2O_5 system formed epitaxial grown needle shaped IrO_2 crystallites on a layer of cobblestone shaped amorphous phase of Ta_2O_5 when heated below 750°C and both phases became crystalline when heated above this temperature [85]. The needle density was believed to determine the maximum in anodic charge. The formation of needles was very sensitive to the preparation conditions and the needles were only formed when using organic solvent and when coated on to a roughened titanium or platinum substrate, not when coated onto substrates of Zr or Ta or polished Ti [97, 98]. No solid solution was found to exist between IrO_2 and Ta_2O_5 by XRD measurements [97]. The influence of catalyst loading on the service life of IrO_2 - Ta_2O_5 electrodes was studied by Krýsa *et* al. [98] and was found to have a linear relationship, which suggested that the layer was uniformly dissolved. The overpotential was found to rapidly decrease by increasing loading until 0.4 $mg \cdot cm^{-2}$. At 1 $mg \cdot cm^{-2}$ and above, no further decrease in the overpotential was observed.

Roginskaya *et* al. [99] used TEM and X-ray measurements to study the IrO_2 - Ta_2O_5 system and showed that for IrO_2 content of less than 30 mole%, IrO_2 formed two rutile phases of small amounts in the mixed film, which was dominated by β-Ta_2O_5. For IrO_2 content of more than 30 mole% the rutile phases of IrO_2 was dominating whereas β-Ta_2O_5 was more or less absent unless the temperature was increased to above 750°C. The presence of IrO_2 was believed to inhibit the growth and formation of the β-Ta_2O_5 phase and visa versa. Above 750 °C crystallization of β-Ta_2O_5 occurred from the amorphous phase. They also found that the surface of the IrO_2 particles were enriched by Ta_2O_5 phase at lower IrO_2 content. TEM measurements showed particle sizes in the range of 7-10 nm, 40-70 nm and 100-140 nm, which was believed to consist of different rutile phases of IrO_2. Spectroscopic studies of the Ir + Ta chloride solutions showed that the intensity of the absorption bands increased by the presence of $TaCl_5$, which indicated that the $[IrCl_6]^{2-}$ complex accumulated on the positively charged surface of the colloidal Ta species.

The mixed oxide of RuO_2 and TiO_2 is the prototype catalyst in the chlor-alkali industry [15]. The study of IrO_2-TiO_2 systems, however, usually involve a third

component, e.g. SnO_2 [55, 100], CeO_2 [56, 34]. SnO_2 has been reported to significantly increase the active surface area when added to the IrO_2-TiO_2 mixture [100]. Additions of CeO_2 has been reported to increase the surface area of the mixed catalyst and to increase the open circuit potential by withdrawal of electrons from the Ir cation [34].

Addition of SnO_2 to the mixed oxide coatings of IrO_2 and RuO_2, prepared by firing the precursors in air, was found to considerably enhance the life time performance of the catalyst mixture, however, on cost of the initial activity [101]. A metastable phase of $(Sn, Ru, Ir)O_2$ with rutile structure was believed to be the reason for the apparent stability of the catalyst.

3.3 Discussion

Contamination of membrane and Pt catalyst have proven to be an important issue. Cell body and pipe lines of stainless steel does not seem to be a very good choice due to release of poisoning ions as Fe^{2+}, Ni^{2+} and Cr^{2+} [70]. Stainless steel is in general recognised to be corrosion resistant in hot water, however, the material will in any case corrode initially until passivation takes place [102]. This strongly points out that stainless steel component should be avoided in SPE® systems.

Titanium is the most commonly used construction material in SPE® electrolysis cells and is the most obvious choice as anode current collector. Passivation of the Ti surface constitute an important issue in SPE® electrolysis and modification of the Ti surface is necessary to obtain corrosion resistant layers with high electrical conductivity. Pt metal can be used as a temporary solution to the problem, however, this constitute a very expensive choice for protection. The ongoing research on Ti in SPE® fuel cells is likely to bring forward some good solutions to this problem in SPE® electrolysis as well. Hydrogen brittleness is a possible danger on titanium under cathodic polarization, which may lead to cracking of the material [103], and other materials can be considered, e.g. carbon.

Pt seem to be the preferred cathode catalyst in SPE® electrolysers due to its high stability and high electrochemical activity towards the HER. Low overpotentials are obtained and the catalyst constitutes less difficulties compared to the anode catalyst. Contamination of the Pt catalyst by UPD of cations and blocking of active sites is a possible danger in the SPE® system and RuO_2 towards the HER in SPE® electrolysers have been studied. However, as long as polymer membranes of Nafion® type are used as electrolyte, the feed water must in any case be kept free from cations which contaminates the membrane and decreases its ionic conductivity. RuO_2 is, however, still interesting as cathode catalyst due to its lower prize.

A wide range of performance data have been obtained by the different research groups using significantly different approach of MEA preparation. Typically the cell potential at 1 $A \cdot cm^{-2}$ and 80 °C ranges between 1.68 - 1.75 V by using Nafion® -115/117 membranes, Pt and Ir as cathode and anode catalysts respectively and a noble metal loading from 1 to 10 $mg \cdot cm^{-2}$. A cell voltage obtained by Yamaguchi *et* al. [79] at 1.53 V is by far the best performance reported. However, this does not necessarily indicate that the best catalysts and preparation techniques have been obtained when considering the very thin membrane of 51 μm in thickness, gold- and Pt-plated current collectors and a relatively high catalyst loading of totally 3.5 $mg \cdot cm^{-2}$. Millet *et* al. [69] obtained 1.75 V using only 1.2 $mg \cdot cm^{-2}$ of noble catalysts by chemical precipitation of the catalysts onto the membrane.

By using a chemical precipitation method for preparation of MEAs it seem to be possible to obtain a good performance at a relatively low loading of noble metals. However, this preparation technique results in metallic Ir as anode catalysts and further corrosion of the catalyst [70]. Thermally prepared IrO_2/RuO_2 based catalysts constitute a much better choice with respect to life time performance compared to metallic Ir [15]. Since the preparation of the metal oxides takes place at 350-600 °C, the oxide catalyst must be prepared before deposited onto the membrane. Two methods for preparation of anode catalyst in SPE® electrolysis seem to be possible; (i) a typical DSA® approach by calcination of the precursor salt onto a porous backing of Ti and (ii) preparation of metal oxide powder and further deposition onto the membrane by hot-pressing, brushing or spraying.

Neither pure RuO_2 nor pure IrO_2 catalysts show satisfactory lifetime performance compared to mixed oxides. The binary catalyst systems of IrO_2-RuO_2 and IrO_2-Ta_2O_5 have exhibited the most promising properties as O_2 evolving catalysts with respect to lifetime and catalytic activity in real applications. The IrO_2-RuO_2 catalyst has already been used as active anode catalyst in SPE® electrolysis system prepared by both the DSA approach [84], i.e. deposition onto the porous Ti backing, and the Adams method [101]. The good catalytic properties of the IrO_2-Ta_2O_5 system is strongly influenced by the substrate [97], and in SPE® electrolysis the catalyst must be prepared by the DSA approach to obtain the same catalytic properties. Reports on the latter mixed catalyst system prepared as powder are scarce.

From this section it is possible to point out the most important issues in SPE® water electrolysis system and what considerations that must be taken for development of active electrodes:

- Cell body, current collectors and other metallic parts should be of titanium.
  - Stainless steel components must be avoided.
- Stability and activity of the anode catalyst is crucial for further development.

  - Thermally prepared mixed oxide systems of IrO_2-RuO_2 and IrO_2-Ta_2O_5 constitute the most promising anode catalysts towards the OER in industrial applications.

- Pt is by far the most realistic alternative as cathode catalyst in SPE® electrolysis when using PFSI-type membranes. Reducing the noble metal loading is the main challenge of the cathodic side.

- Preparation of electrodes should be carried out to obtain thermally formed metal oxides at the anode side.

Chapter 4

Experimental

4.1 Chemicals and apparatus

Chemcials used for preparation of metal oxide catalysts and for preparation of MEAs are given in table 4.1 and 4.2 respectively.

Table 4.1: Chemicals (pro analysis) for metal oxide preparation.

Chemical	Manufacturer
$H_2IrCl_6 \cdot 4H_2O$	Johnson Matthey, Alfa Aesar
$RuCl_3 \cdot xH_2O$ (99.9%)	Johnson Matthey, Alfa Aesar
$TaCl_5$	Merck
$NaNO_3$	Merck
30 wt% H_2O_2	Merck
H_2SO_4 cons.	Merck

Table 4.2: Membrane and fuel cell catalysts.

Chemical	Manufacturer
Nafion® membrane	Du Point, ElectroChem, Inc.
Nafion® solution 5 wt%	Du Point, ElectroChem, Inc.
10-40 wt% Pt on Vulcan XC-72	Johnson Matthey, E-TEK, Inc.
Pt-black	Johnson Matthey, Alfa Aesar

All water was tapped from a Milli-Q® Ultra Pure Water Systems connected to a water distillation system. The resistance of the water was 18.2 $M\Omega \cdot cm$.

Equipment:

- Potentiostat: Autolab PGSTAT20, Echo Chemie.
- 10 A booster: Autolab PGSTAT10, Echo Chemie.
- Pumps: Eheim universal circulation pumps (300 l per hour)
- Air gun: Badger™ Air-Brush 200-Gil.
- Ceramic furnace with electrical heating.

SPE-cell

A principal sketch of the SPE-cell, used for determination of separate anode and cathode behaviour, is shown in figure 4.1. Water enter the anode side and, under polarization of the cell, becomes split into oxygen gas, protons and electrons. Oxygen leave the anode chamber, protons migrate through the membrane to the cathode side where it re-combines with electrons and form hydrogen gas.

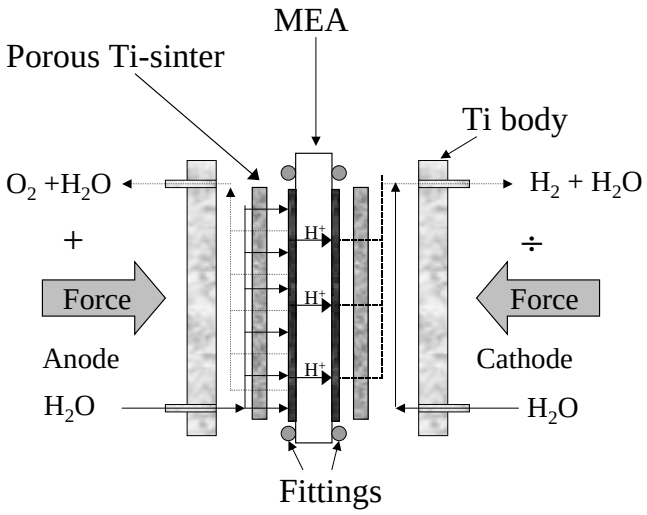

Figure 4.1: Principal sketch of the SPE-cell.

Two almost identical SPE-cells were made at the workshop of NTNU and each cell was made of titanium in two identical parts. The flow fields were machined into

Figure 4.2: Picture of SPEcell together with fittings, Ti-sinters and one MEA.

the titanium body and was 2 mm in depth and 2 mm in width and the flow field patterns are shown in figure A.1 in appendix. A picture of a SPE-cell together with fittings, Ti-sinters and one MEA in front can be seen in figure 4.2. The four bolts in each corner of the Ti end-plate to the left in figure 4.2 fitted exactly into the four holes of the opposite end-plate to the right so that exact positioning of the end-plates could be obtained, see also figure A.2 in appendix. A brass bolt, 1 cm thick and 5 cm long, was screwed into the back side of the Ti-body, which can be seen in figure A.2 in appendix. After assembling the MEA into the cell, between the Ti sinters, the cell was mounted in a clamp at a manually fixed mechanical pressure, which can be seen in figure A.3 in appendix. The pressure was fixed by a screw until no further pressure could be obtained unless brutal force was applied. A second and almost identical cell was made with the exception that the flow fields were machined in both vertical and horizontal direction. No limitation of gas/water flow was obtained in any of the two cells within the current range investigated and both cells were used in parallel without specific reference to any of the cells.

The cells were designed with main emphasis on reducing the ohmic contribution from the cell hardware and at the same time maintain easy flow of water and gas. Straight current pathways, short length and wide cross section area for current transport is crucial when operating an electrochemical cell at such high current densities. The ohmic resistance of the cell hardware was controlled before each new measurement by mounting the cell together without an MEA and then measuring the ohmic drop when applying a total current of 10 A (2 $A \cdot cm^{-2}$ of the active area) between the brass-bolts. The ohmic drop between the end-plates was less than 5 mV at 10 A when using fresh Ti-sinters. When the ohmic drop exceeded 10 mV at 10 A, the Ti-sinters were replaced by new ones. The Ti sinters were used without any further protection and became oxidized after some time of use and had to be replaced after some time of use. The Ti-sinters were of 10

micro meter grade, obtained from Mott Corporation, USA. The diameter was 1 inch and the thickness 2 mm.

Feed water was circulated through anode and cathode compartment by two centrifugal pumps, mainly to reduce the effects from heat production at high current density. Measurement at higher temperatures was possible by pre-heating of the bottle reservoirs, however, the temperature was difficult to control for different current densities. A sketch of the water management is shown in figure 4.3.

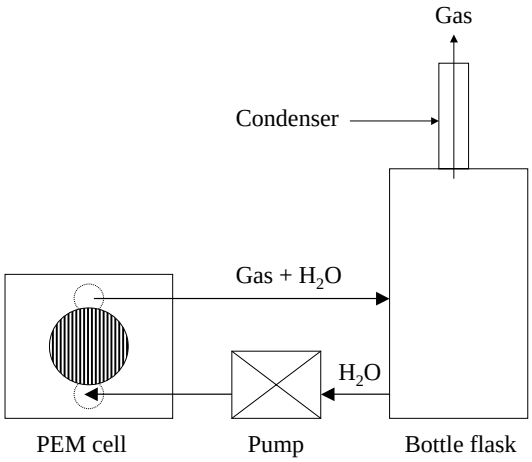

Figure 4.3: Sketch of water management of the SPE-cell.

A third SPE-cell was obtained from Kurchatov Institute in Moscow. This cell was also made of Ti and the active area was 5 cm^2. The flow field pattern of this cell was the same as described above, with cross flow fields. This cell had integrated water channels inside of the end-plates, not interconnected to the feed water channels, and could be used for measurements at higher temperatures by circulation of hot water from a thermostated bath through the integrated water channels. No pumps were used to circulate the feed water of this cell and self-circulation of water through anode and cathode compartment took place as a consequence of gas production.

The Kurchatov-cell was more difficult to operate and was not suitable for half-cell measurements. The cell had a higher ohmic drop (30-50 mV at 10 A) and a somewhat non-uniform surface of the flow fields resulted in lower performance compared to the NTNU-cells. This cell design provided easy temperature control and the cell was merely used to obtain polarization curves at higher temperatures. The temperature was measured inside the cell at the anode side by using a Pt/Pt

+ 5% Rh thermocouple and maximum temperature obtained by this cell was 80 °C when the thermostat bath measured 100 °C.

Reference electrode

Reference electrodes of Hg/Hg_2SO_4 type were made for *in situ* electrochemical measurements in the SPE-cell. The reference electrode was made by first filling a glass capillary of 5 mm in diameter and 10 cm in total length with wetted Nafion® membrane. A paste, made from Hg_2SO_4 and 1 M H_2SO_4, was inserted at the top of the capillary onto the membrane material and few drops of $Hg_{(l)}$ was placed on top of the paste. A Pt wire was placed in contact with the $Hg_{(l)}$ and the top of the capillary was sealed with epoxy leaving 1 cm of the Pt wire outside the capillary available for electrical contact. The bottom-end was left open with 5 mm of the membrane material outside the capillary for ionic contact with the MEA. The electrodes were always stored in pure water to prevent drying. A sketch of the reference electrode can be seen in figure 4.4.

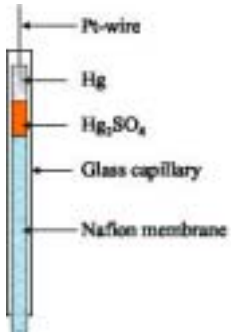

Figure 4.4: Sketch of the reference electrode used for SPE-cell measurements.

A small pit was made into the top of the fittings of the SPE-cell to expose a slip of the membrane and a few drops of water was added into the pit. The reference electrode was placed in ionic contact with the wetted membrane and the contact point inside the pit was kept wetted during the measurements by regularly adding a few drops of water. Usually, a few drops each hour was sufficient to maintain wetted conditions inside the pit. This cell arrangement is in principal the same as used by P. Millet [104], who showed that the measured reference potential was the same as in the middle between anode and cathode.

The potential of the reference electrodes was measured between 0.69 and 0.73 V towards a reversible hydrogen electrode (RHE) and the potential of these reference electrode changed by less than 5 mV after 1-2 years of use. The potential of the reference electrode was regularly calibrated against the RHE.

4.2 Electrochemical measurements in the SPE-cell

Only the NTNU-cells were used for *in situ* electrochemical measurements. The MEAs were first operated galvanostatically at 0.2 $A \cdot cm^{-2}$ for 30 minutes to obtain steady state behaviour of the catalysts.

Voltammetry of both anode and cathode was measured for each MEA against the reference electrode at different scan rates from 20 to 100 $mV \cdot s^{-1}$, between the potential limits of hydrogen and oxygen evolution reaction. Three scans at each scan rate was obtained and the third scan was chosen for presentation and calculation of data. All voltammograms were measured at room temperature by the Autolab potentiostat and the NTNU-cells.

AC-impedance was determined at room temperature from 10 kHz to 10 mHz. For comparison of the impedance between different MEAs, the measurements were performed under galvanostatic control at constant current density of 20 $mA \cdot cm^{-2}$ using an amplitude of 10 mA. This allowed separation of the anodic and cathodic contribution to the total impedance at exactly the same operating conditions. To find the impedance-potential behaviour, the impedance was determined under potentiostatic control at different potentials using an amplitude of 5 mV. Impedance data were fitted by use of ZView software from Scribner Associates, Inc.

Steady state polarization curves were obtained under galvanostatic control at cds up to 2 $A \cdot cm^{-2}$. The anode and cathode potentials were measured simultaneously versus the same reference electrode and the cell potential between the two end-plates. All potentials were determined by three digital Yokogawa multimeters and the data were logged by a computer. The measured potential after 10 minutes of each current step was used for obtaining the polarization curves. The measurement were automatically interrupted to prevent strong oxidation of the Ti-current collectors and cell hardware when the total cell voltage exceeded 2.5 V.

Measurements performed above room temperature were performed using the Kurchatov -cell, where quasi steady state polarization curves were obtained at a scan rate of 10 $mA \cdot s^{-1}$ and 10 mA steps.

4.3 Transmission Electron Microscopy

The particles, prepared by the Adams fusion method [58], were examined in a Jeol 2010 transmission electron microscope (TEM) operating at 200 keV. A slurry of the particles and ethanol was made and a drop of the slurry was transferred to a copper grid with a carbon film. The particles were imaged in bright-field at suitable magnifications, while the crystallinity of the particles was examined by selected-area diffraction with a camera length of 100 cm.

4.4 Scanning Electron Microscopy

SEM measurements were performed using a Zeiss DSM 950 Scanning Electron Microscope. Gold was deposited onto the samples of exposed polymer membrane

to avoid electrical charging of the surface.

4.5 Preparation of metal oxides by Adams method

The background for this preparation procedure is given in section 2.6. The metal chloride precursors were mixed in excess amount of $NaNO_3$ and dissolved in water, using 50-100 g $NaNO_3$ per 1 g precursor. Water was carefully evaporated from the mixture on a heating plate. The salt mixture was introduced into a pre-heated ceramic furnace from 5 - 30 minutes until the evaporation of the dark brown nitrous gas stopped. The salt mixture was then cooled to room temperature and washed in water to remove excess salt. The resulting metal oxide was then dried and annealed at evaluated time and temperatures.

4.6 Preparation of MEAs

A short screening process of different MEA-preparation techniques was carried out at an early stage of this work. The so called spraying technique[1] was chosen for MEA preparation. Spraying directly onto the membrane [105, 106] or onto the backing/current collector [106, 68] is a commonly applied technique for preparation of electrodes in SPE fuel cells. The spraying technique was preferred due to its simpleness and because the catalyst loading was easier to control compared to the other methods. Other techniques were tested for electrode preparation, i.e. brushing, chemical precipitation into the membrane and thermal decomposition of anode catalyst onto the Ti-backing. These methods involved preparation of relatively large quantities of catalysts and catalyst loss became significant and was found to be unsuitable on a laboratory scale. The outcome of the other methods led to no measurable results and they were abandoned at an early stage and will not be further described.

The membrane was cleaned according to procedure described by Srinivasan *et* al. [107]. The membrane was first preheated in pure water at 80 - 90 °C and then transferred to a solution of 5 wt% H_2O_2 at 70 - 80 °C for 30 minutes to remove organic impurities. The membrane was then kept in pure water for approximately 10 minutes at 80 - 90 °C and further heated in 0.05 M solution of H_2SO_4 at 80 - 90 °C for 30 minutes to ion exchange the membrane completely with protons and to remove metallic impurities. At last the membrane was boiled repeatedly 4 times in pure water. The membranes were stored in pure water.

The exact amount of catalyst needed for preparation of one catalytic layer was measured on a mass balance and the amount of Nafion® ionomer was added

[1] The method for MEA preparation used in this work was basically obtained at the Department of Hydrogen Energy at Kurchatov Institute in Moscow after three weeks stay at their laboratory.

relative to the amount of catalyst from 5 - 30 wt%. Typical ink composition is given in table 4.6. A total volume of 1 ml represented a convenient amount for preparation of 5 cm^2 catalytic surface.

Table 4.3: Ink composition and conditions during spraying of 5 cm^2 surface area

Catalyst	x mg
Nafion ionomer	5 - 30 % of x
Water	0.5 ml
Ethanol	0.5 ml
Glycerol	20-30 mg
Air pressure	0.5 - 1 bar

The ink was first ultrasonically mixed for approximately 5 minutes and then transferred to the cup of the air gun, shown in figure 4.5. The spraying was immediately carried out and the ink was carefully deposited onto the membrane fixed in a frame. Excess water was removed from the membrane surface prior to spraying. Deposition of the ink was carried out by careful inspection of the spraying-zone at the membrane surface, which was kept in a semi-dry condition without flooding of ink solvent. Pressure and nossle-opening of the air-gun was adjusted according to particle size and viscosity of the ink. Typical time for preparation of one catalytic layer varied from 15 to 20 minutes. Ethanol was used as solvent to speed up the evaporation of the ink under deposition. Isopropanol could also be used instead of ethanol and no significant difference was observed between the two solvents. Ethanol was preferred due to less toxicity. Glycerol was used to tailor the viscosity of the ink [108] and to prevent the catalytic layer from becoming smeared out at the membrane surface.

Figure 4.5: Badger air gun.

After deposition of catalytic layers on both sides of the membrane, the MEA was kept in an oven at 125 °C for 1 hour for polymerisation of the Nafion® ionomer to take place. The MEA was at last boiled in 10 wt% HCl for 30 minutes to protonate the membrane, repeatedly boiled in pure water and then kept in water prior to use.

Chapter 5

Results and discussion

5.1 PEM cell measurements

This section shows the basic characteristics of the SPE-cell and gives an evaluation of the in situ electrochemical measurements.

Electrochemical measurements of SPE-cells are typically carried out by determining the potential between the end-plates. Usually, the overpotential of the hydrogen electrode is small and are neglected compared to the oxygen electrode. Steady state polarization curves at 80 - 90 °C are often the only technique used to characterize the electrodes. However, to be able to reduce the noble metal loading of both anode and cathode layer, individual optimization is necessary and a reference electrode must be used.

5.1.1 Transport limitations

Figure 5.1 shows a polarization curve of an MEA measured at approximately 80 °C using Nafion® -115 membrane and 40% Pt on Vulcan XC-72 and RuO_2 as cathode and anode catalyst respectively. The noble metal loading was 0.5 mg $Pt \cdot cm^{-2}$ at the cathode and 1 mg $RuO_2 \cdot cm^{-2}$ at the anode. The curve demonstrate some of the most interesting futures of SPE electrolysis where current densities up to 4 $A \cdot cm^{-2}$ without diffusion limitations is possible to obtain at a relatively low U_{cell} (high energy efficiency). At 3 $A \cdot cm^{-2}$ U_{cell} is still below 2 V and at 1 $A \cdot cm^{-2}$ the cell voltage is 1.62 V. It can be seen that the curve is not strictly linear for high cds, probably caused by heat production, transitions to higher Tafel slopes and gas bubble release. The anode catalyst was originally a $RuO_2 \cdot xH_2O$ powder (Merck) which was annealed at 450 °C for 1 hour and served merely as a test catalyst before a proper technique for catalyst preparation was developed. Figure 5.2 shows the cell voltage versus time obtained at 1 $A \cdot cm^{-2}$

and 80 °C and confirm the insufficient life time performance of the pure RuO_2 catalyst. Weininger *et* al. [109] studied the MEAs by electron microscopy after water electrolysis and found a line of RuO_2 particles within the membrane at a distance of 2-8 μm away from the anode layer. It was believed that a pH gradient was produced through the membrane and that dissolved Ru-species precipitated when exceeding its solubility limit at a certain pH. This may explain the very sudden increased in cell voltage after about 5 hours, where deterioration take place due to blocking of ionic transport by precipitated Ru-species in addition to loss of active catalyst.

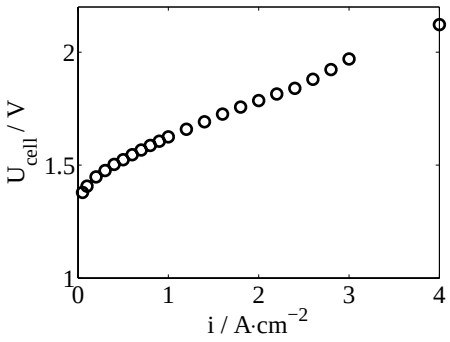

Figure 5.1: Cell polarization at 80 °C of 40 wt% Pt on Vulcan XC-72/Nafion-115/ RuO_2 composite.

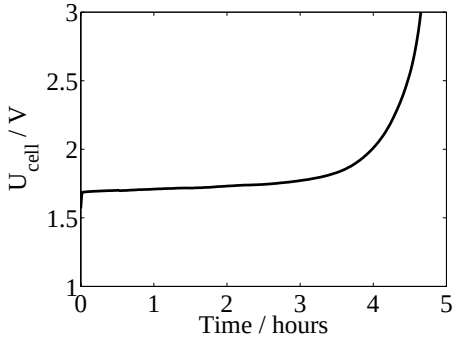

Figure 5.2: Life time performance at 1 $A \cdot cm^{-2}$ and 80 °C using pure RuO_2 anode catalyst.

Diffusion processes may still take place in the SPE® water electrolyser system, i.e. diffusion of H_2 away from the Pt catalyst [25] and diffusion of H^+ in the Ru oxide [50]. However, these diffusion processes are fast and does not limit the system at continuous operation.

5.1.2 Voltammetry

The capacitance of oxide electrodes of Ir and Ru is mostly related to its pseudocapacitance[1], where the double layer contribution to the total measured capacitance is usually from 5 to 10 % when the pseudocapacitance has an appreciable value [110].

Figure 5.3 show the voltammograms of an IrO_2 electrode measured at different scan rates from 20 to 100 $mV \cdot s^{-1}$. This catalyst[2] was pyrolysed at 340 °C for 30 minutes and annealed at 490 °C . The anodic current density was measured at 1.2 V_{RHE} for all scan rates and is shown in figure 5.4. As can be seen there is an excellent linearity between i_p and ν where the regression line exhibits a correlation coefficient close to 1, which confirms the reversibility of the electrode

[1] see section 2.3.2
[2] see section 5.2

reaction. The capacitance of this electrode was found from the slope of the line to be 110 $mF \cdot cm^{-2}$ according to equation 2.24.

Some sharp peaks are present in the voltammograms. These peaks are not present on IrO_2 when measured in sulphuric acid solutions, neither are they present on Pt nor on RuO_2 when measured in the Nafion environment. At higher annealing temperatures of the IrO_2 catalysts, the sharp peaks observed in the SPE® system tend to disappear. Some phenomena related to the Nafion environment or to non-converted precursor within the oxide may be possible causes.

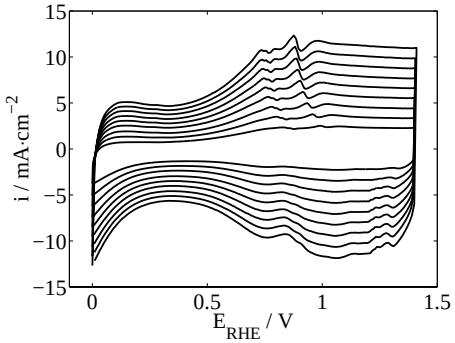

Figure 5.3: Voltammograms of IrO_2 catalyst measured at scan rates from 20 to 100 $mV \cdot s^{-1}$.

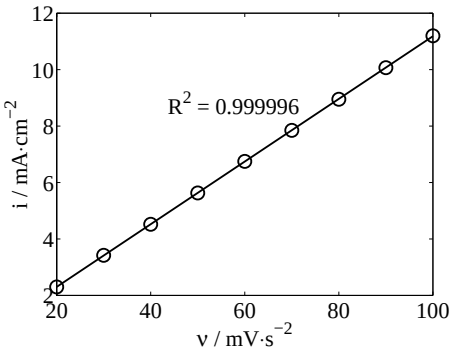

Figure 5.4: Anodic charging current measured at 1.2 V_{RHE} versus scan rate.

The voltammograms resemble that of IrO_2 when compared to figure 2.11 prepared by the DSA approach, except from the presence of the sharp peaks.

5.1.3 AC-impedance

Results from AC-impedance provides important information about the ohmic resistance as well as the electrochemical activity. The impedance of these systems is in general very small. In systems of low impedance, AC-impedance measurements are strictly limited to a small current density region, where the polarization resistance, R_p, is of a certain measurable value. At higher current densities the accuracy of the measurement soon becomes disturbed by artifacts from the instrumentation and by increased bubble formation. One way to overcome this problem is of course to produce smaller electrodes. However, when using the spraying technique performed manually, 5 cm^2 represents a convenient size where the technique can be evaluated with respect to structure and uniformity of the catalytic layers as well as the properties of the electrocatalysts. For smaller electrodes, edge effects become important and the effective loading of catalyst becomes more difficult to control.

The use of AC-impedance in a cell configuration with reference electrode and thin electrolyte, as in this work, can be questioned. A critical parameter is the

frequency stability of the equipotential lines at the point where the reference electrode is in contact [111]. Small displacements of the working and counter electrodes relative to each other may result in a large deviation of the value of the electrolyte resistance. However, due to the relatively long distance between the contact point of the reference electrode and the working electrode (1 cm) compared to the electrolyte thickness (125 mm), this issue should not pose an important problem [112, 113].

AC-impedance measurements obtained in this work are mainly used for determination of the ohmic resistance of the samples. According to Millet [114] the reference potential of a SPE-cell system is measured in the middle between anode and cathode. Figure 5.5 shows the impedance of anode, cathode and cell when measured at a constant current density of 20 $mA \cdot cm^{-2}$ and a signal amplitude of 10 mA. The pseudo-inductive loop at high frequencies of the cathode impedance is further discussed in section 5.5. Adding together the real- and imaginary values of the anodic and cathodic impedance, results in an impedance spectrum equal to the measured cell impedance as shown by the semicircle of continuous line in figure 5.5. A small deviation can be seen at high frequency, approximately above 1 kHz, where the measurements are disturbed by inductance. The sum of the ohmic resistance of anode and cathode, matches the measured ohmic resistance of the cell by less than 5 % deviation, which is satisfactory for correcting the polarization curves for ohmic contribution. As can be seen from figure 5.5 the ohmic resistance of anode and cathode is about half the ohmic cell resistance. However, this does not need to be the case for every measured MEA, since the ohmic drop through the catalytic layer will depend on the percolating path for electrical current transport, which can be expected to change according to preparation conditions of the different catalytic layers.

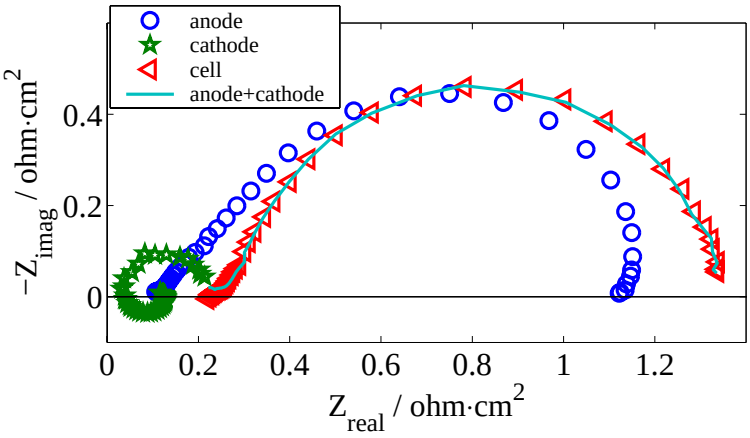

Figure 5.5: Impedance of cathode, anode and cell.

To be able to separate the impedance contribution of anode and cathode at a given

production rate, the impedance was measured at constant anodic and cathodic current of 20 $mA \cdot cm^{-2}$ at the anode and cathode respectively.

For a few samples the impedance was measured as a function of the potential under potentiostatic control. No significant difference of the impedance spectra was obtained between galvanostatic and potentiostatic control. Two impedance spectra measured under potentiostatic control are shown in figure 5.6 together with an impedance spectrum measured under galvanostatic control at 20 $mA \cdot cm^{-2}$. Spectra a and c was measured at 1.510 and 1.520 V_{RHE} respectively using an amplitude of 5 mV. The potentials and current densities of the three measurements are given in table 5.1 and as can be seen from figure 5.6 the impedance decreases at increasing polarization as expected and the shape and magnitude of the impedance does not seem to be influenced by potentiostatic or galvanostatic control. An amplitude of 10 mA under galvanostatic control was found after some trial and error.

Table 5.1: Potentials and current density of impedance spectra.

Sample	E_{RHE} (V)	i ($mA \cdot cm^{-2}$)	Measurement
a	1.510	16	Potentiostatic control
b	1.512	20	Galvanostatic control
c	1.520	26	Potentiostatic control

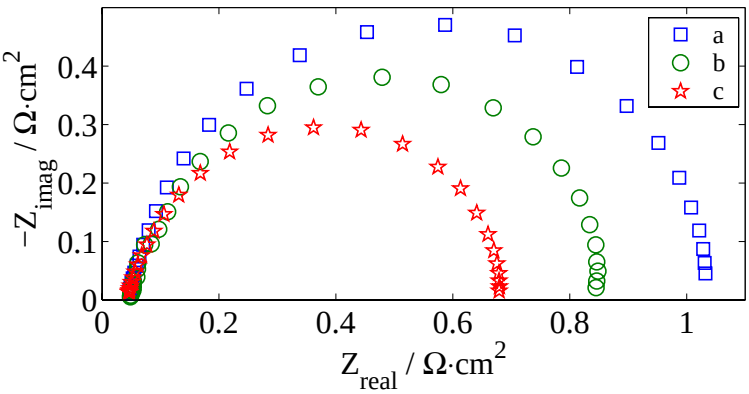

Figure 5.6: Spectra a and c: impedance under potentiostatic control, spectra b: impedance under galvanostatic control.

5.1.4 Polarization curves

Figure 5.7 shows the forward and backward scan of IrO_2 anode and Pt supported cathode when polarized galvanostatically and measured simultaneously versus the same reference electrode. No significant hysteresis of the curves can be observed. Large hysteresis may take place on freshly prepared oxide electrodes where the backward scan possesses higher potentials than the forward scan [115]. However, due to initial polarization of the electrodes at 0.2 $A \cdot cm^{-2}$ for 30 minutes, a more well defined surface state is obtained at the oxide. For most polarization measurements, only the forward scan was performed.

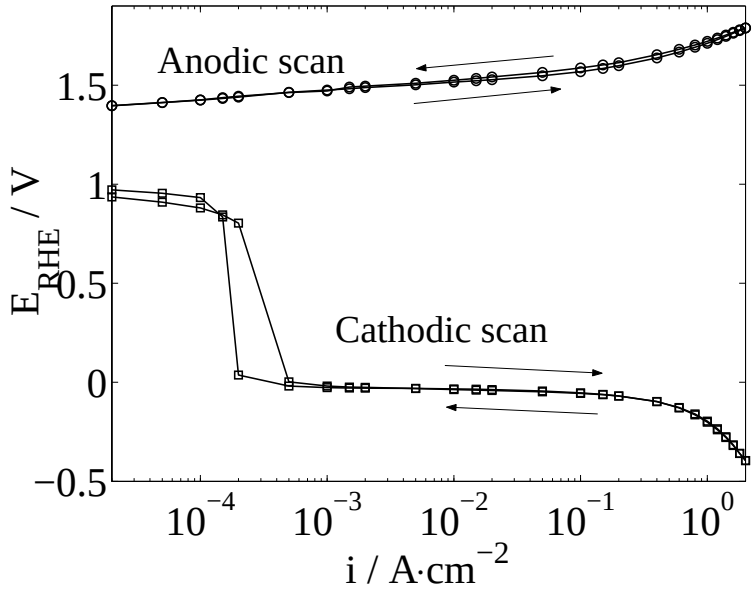

Figure 5.7: Forward and backward scan of anode and cathode.

It can be seen that the cathodic curve starts from anodic potentials at about 0.94 V_{RHE} and increases to about 0.98 V_{RHE} after the backward scan. This high anodic rest potential at the Pt supported catalyst is determined by the presence of oxygen. The higher rest potential after H_2 evolution indicate that the catalyst has become more active towards the ORR, which probably can be explained by increased wetting of the hydrophobic catalyst.

5.1.5 Aging effect

Figure 5.8 shows the transient behaviour of an IrO_2 electrode after stepping the current to 0.2 $A \cdot cm^{-2}$. Thermally prepared oxides are typically non-stoichiometric

[41] provided by different valence state of the metal cation, i.e. Ir(III)/Ir(IV). Non-stoichiometry generates defects, which are believed to be the active sites at the oxide surface. Loss in activity on anodically formed oxides of Ir was explained by Gottesfeld *et* al. [38] in terms of an aging effect by the oxidation of lower valence states to more stoichiometric IrO_2. "Rejuvention" of the reduced centres was reported to take place by performing a back scan to 0.25 V_{RHE} and then returning to anodic potentials where enhancement of the cd by a factor of more than two was obtained [38]. This aging effect has not been further studied, however, the phenomenon has been observed to take place throughout this work on all metal oxides catalysts polarized anodically.

The "rejuvention" effect can be an interesting topic for further study. This may be advantageous where the electrical power is generated from power sources of alternating output signal, e.g. wind mill and solar panels.

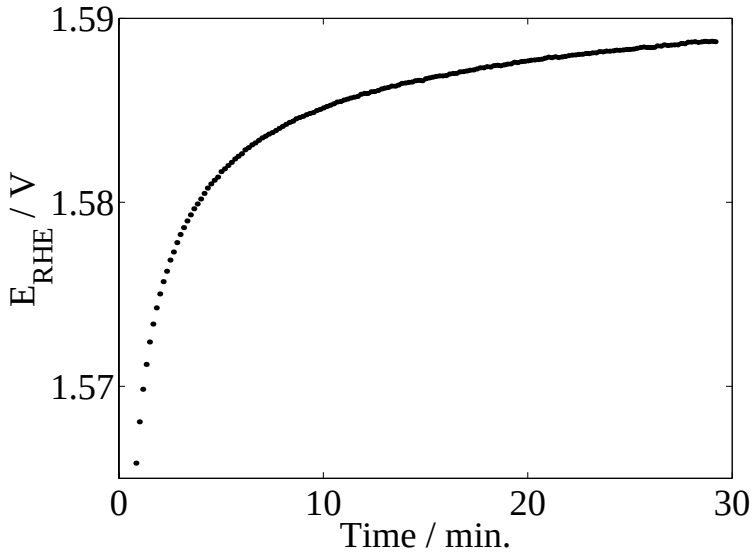

Figure 5.8: Chronoamperometry of IrO_2 electrode. Current stepped to 0.2 $A \cdot cm^{-2}$.

5.1.6 Membrane resistance

The ionic conductivity of a Nafion® -115 composite was measured by AC-impedance at different temperatures using the Kurchatov-cell and the Arrhenius plot can be seen in figure 5.9 obtained from R_Ω. It is observed that there is a change in activation energy of ionic conductance at approximately 49 °C, which is in very close agreement with 50.4 °C found by Ferry *et* al. [116]. This shows that the there is a change from low to high activation energy in ionic conductivity of the Nafion® membrane when the temperature is raised above 50 °C.

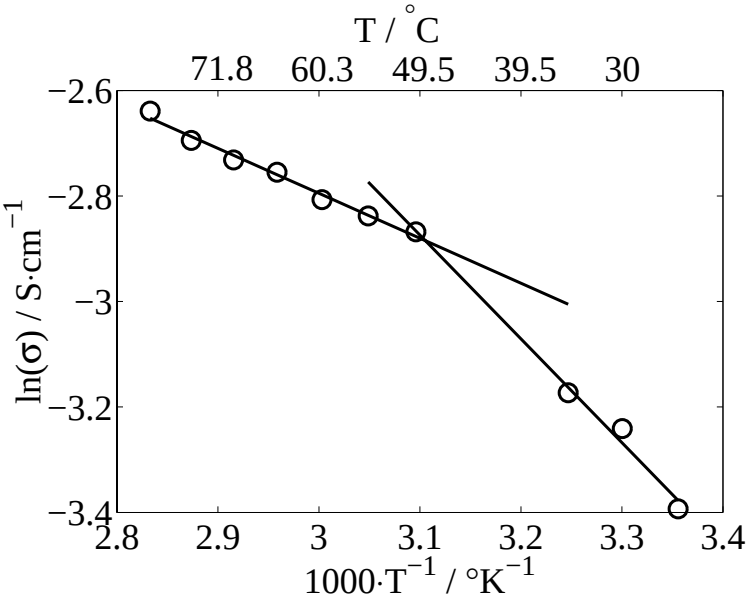

Figure 5.9: Arrhenius plot of MEA of IrO_2/Nafion-115/Pt on carbon composite.

U_{cell} versus current density as a function of the temperature is shown in figure 5.10. At 1 $A \cdot cm^{-2}$ U_{cell} decreases by 242 mV as the temperature increases from 25 to 75 °C. It can be seen that the decrease in U_{cell} becomes less for temperatures of 55 °C and above, which is in agreement with the Arrhenius plot in figure 5.9. At 2 $A \cdot cm^{-2}$ U_{cell} decreases by 336 mV when increasing the temperature from 25 to 75 °C. From the data in figure 5.9 the difference in R_Ω at 25 and 75 °C becomes 0.369-0.188 = 0.181 $\Omega \cdot cm^2$. Thus, the ohmic contribution to U_{cell} at 1 and 2 $A \cdot cm^{-2}$ should be reduced by 181 and 362 mV respectively. The discrepancy at 1 $A \cdot cm^{-2}$ is probably caused by improved kinetics and a lower thermodynamic potential, whereas at 2 $A \cdot cm^{-2}$ bubble-effects may be more important, i.e. larger bubbles and higher bubble pressure within the catalytic layer.

The influence on U_{cell} by the membrane thickness can be seen in figure 5.11. At 1 $A \cdot cm^{-2}$, U_{cell} is 230 mV less when using Nafion® -112 (50 μm) compared to Nafion® -117 (175 μm). According to table 2.5 the difference in R_Ω of Nafion® -117 and Nafion® -112 is 0.23-0.036 = 0.194 $\Omega \cdot cm^2$, which corresponds to an ohmic drop-difference of 194 mV between the two membranes at 1 $A \cdot cm^{-2}$. At 2 $A \cdot cm^{-2}$ the difference in U_{cell} is about 360 mV and from the R_Ω values in table 2.5 the ohmic drop difference represents 390 mV. This is actually in quite good agreement taking into account the reproducibility of the cathode catalysts (see section 5.5) of typically ± 50 mV at 1 $A \cdot cm^{-2}$ and at room temperature. It can be noted from figure 5.11 that the curves separate from each other at 0.25-0.40

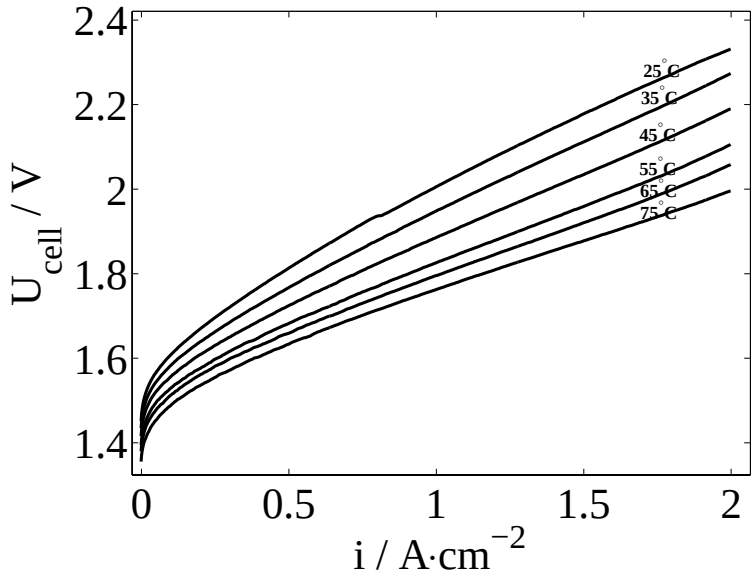

Figure 5.10: Cell voltage versus current density at increasing temperatures from 25 to 75 °C of MEA using Nafion-115.

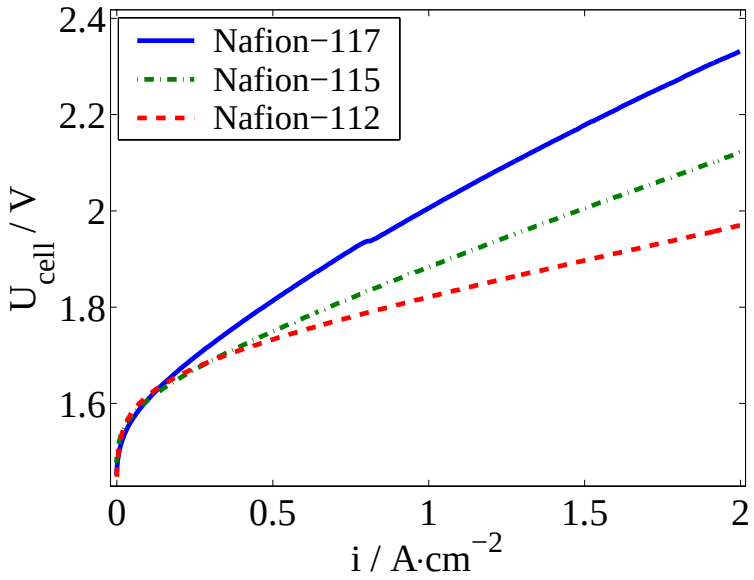

Figure 5.11: Polarizaiton curves using Nafion membranes of different thickness, measured at room temperature.

$A \cdot cm^{-2}$, which means that the ohmic drop contribution of the Nafion® membrane becomes significant. It must be noted here that the R_Ω-values in table 2.5 are

measured for 100 % RH where $\lambda \sim 18$. In water electrolysis the water content of the membrane can be expected to be higher and the ionic conductivity also to be higher. As shown in figure B.3 the Nafion® -115 membrane is 100 μm rather than 125 μm. The membrane expand approximately 10-15 % (both in x- and y-direction) after the cleaning procedure and as a result, thinning of the membrane take place. Thus, a lower ohmic resistance of the membranes used in this work can be expected compared to the literature.

5.2 Effect of annealing the IrO_2 catalyst

This section shows the basic influence of physical and electrochemical properties of the IrO_2 catalyst in the SPE cell as a function of annealing conditions and the most important factors which limits the electrode performance.

The Adams method was chosen mainly due to its simpleness and because of previous reports on using this method in SPE electrolysis [101, 109, 117]. However, detailed descriptions of the preparation procedure is not easy to obtain and even when following a description given in the literature, the results typically deviates between different laboratories due to small differences in the preparation process. The influence of the annealing conditions on the electrochemical properties and the performance will be shown.

5.2.1 Experimental

The initial calcination stage, where the metal chloride precursor is fused in a nitrate melt, was performed at 340 °C for 30 minutes for all samples. The metal oxide was then annealed according to table 5.2. All electrochemical experiments were performed *in situ* in the NTNU-cells at room temperature. Nafion® -115 membrane was used as electrolyte for all samples. Detailed description of the methods are given in section 4.

Table 5.2: Annealing conditions

Sample	Temperature (°C)	Time (hours)
a[1]	-	-
b	440	8
c	490	8
d	510	8
e	540	8

[1] Not annealed

5.2.2 Results

Transmission Electron Microscopy

TEM images of a non-annealed sample (*a*) and of a sample annealed at 490 °C (*c*) can be seen in figure 5.12 and 5.13 respectively. Diffraction images of the samples are shown in the small figure in upper left corner. The average particle size of the non-annealed sample was observed to be in the range 5-20 nm and the majority of the particles were amorphous, recognised by the diffuse and broad rings and

the absence of speckles in the diffraction image shown in figure 5.12. Only a small fraction of the smallest particles (< 10 nm) was observed to be crystalline, shown by narrow rings and a high number of speckles in the diffraction image. The annealed sample showed a wider distribution of particle size within the range of 5-100 nm. The larger particles consisted of small crystallites of approximately 5 nm in size or less, as can be seen in figure 5.13. Diffraction image of the annealed sample reveal a high degree of crystallinity, which was found for all the particles investigated within this sample.

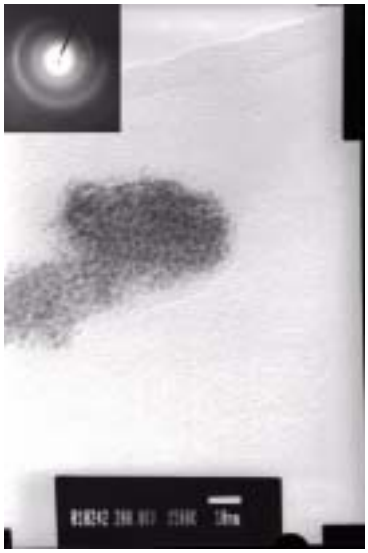

Figure 5.12: TEM and diffraction image of sample a.

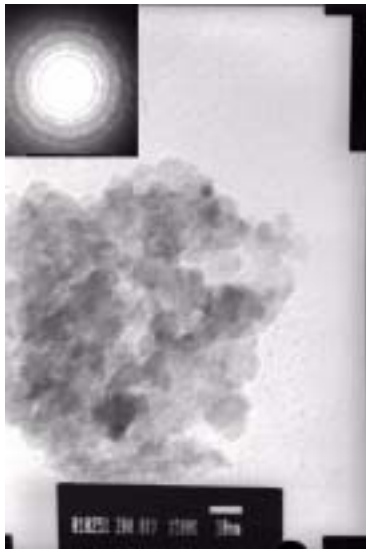

Figure 5.13: TEM and diffraction image of sample c.

Scanning Electron Microscopy

A SEM photo of an anode layer can be seen in figure 5.14 and the layer consists of particles of approximately 0.5 - 1 μm in particle size and a few larger flake-shaped particles up to 5 μm in size. This is a representative morphology of the anodic layers and no difference in particle size on a μm scale can be observed between the different samples. No apparent change in morphology or particle size of the anodic layers can be detected after electrochemical measurements.

Voltammetry

Figure 5.15 shows the voltammograms of the different samples cycled at 20 $\mathrm{mV{\cdot}s^{-1}}$ as a function of annealing temperature. Sample *a* in figure 5.15a exhibits a large voltammetric area in the oxygen regions (note that a different scaling of the current axis has been used in figure 5.15a).

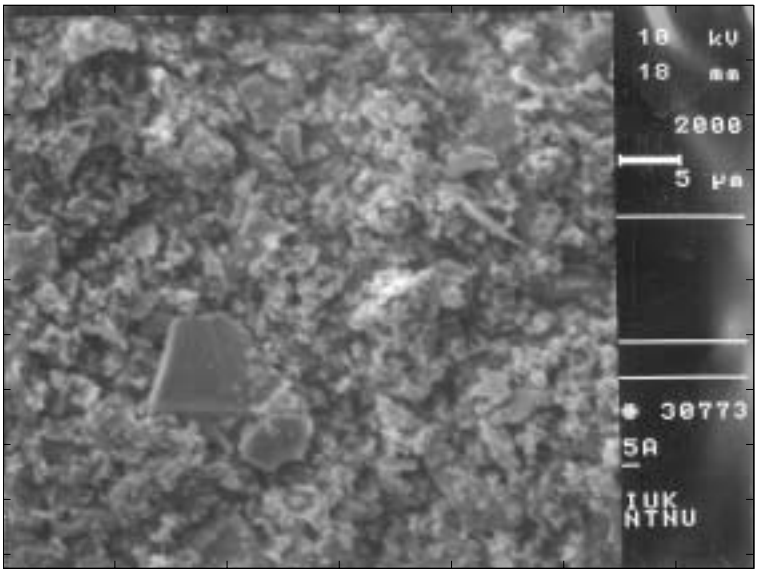

Figure 5.14: SEM photo of an IrO_2 catalytic layer. Magnified 2000X.

The voltammograms of the annealed samples in figure 5.15b to 5.15e are more narrow in the oxygen region and wider in the hydrogen region, which is more typical of a thermally prepared oxide. Further inspection of the voltammograms in figure 5.15 shows that the voltammetric charge decreases at increasing annealing temperature. From 440 °C (fig. 5.15b) to 490 °C (fig. 5.15c) no major changes occur, whereas at 510 °C (fig. 5.15d) a small decrease in the voltammetric charge can be observed. A further considerable decrease of the voltammetric charge occurs after annealing at 540 °C (fig. 5.15e).

The main peak attributed to the redox couple Ir(III)/Ir(IV) at 0.9 V_{RHE} decreases more relative to the peak at 1.35 V_{RHE} attributed to the Ir(IV)/Ir(VI) redox couple (see section 2.5). A shift of the main peak towards higher anodic potentials indicates a transformation of the oxide from Ir_2O_3 to IrO_2 [38], caused by increased valence of the Ir ion. At 540 °C, the peak at about 1.35 V_{RHE} becomes more visible and the sharpness of the peak indicates a more ordered crystal structure of lower surface heterogeneity of this sample [90].

The capacitance of the samples were obtained, as shown in section 5.1.2, and the values are shown in table 5.3 and the capacitance decreases by increasing annealing temperature.

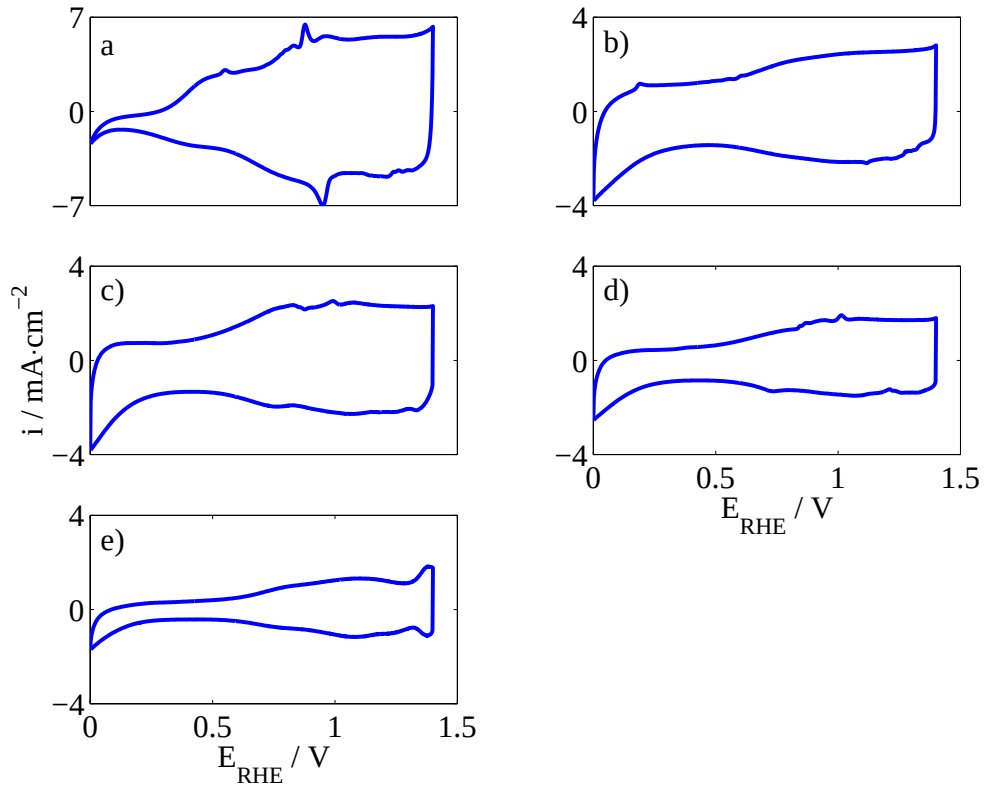

Figure 5.15: Voltammograms of IrO_2 catalyst as a function of annealing temperature, measured at room temperature at a scan rate of 20 $mV \cdot s^{-1}$. a: Not annealed; b: 440 °C; c: 490 °C; d: 510 °C; e: 540 °C. Annealing time 8 hours.

Table 5.3: Capacitance found by voltammetry.

Sample	Capacitance ($mF \cdot cm^{-2}$)
a	283
b	128
c	110
d	88
e	66

AC-impedance

The impedance spectra in figure 5.16 were measured at constant current of 20 $mA \cdot cm^{-2}$ and show that R_Ω, defined as the intercept with the real axis at high frequencies, decreases as the annealing temperature is increased. It can be

seen that the semi circle increases from sample *a* to *e*, which means that the polarization resistance, R_p, increases as the annealing temperature is increased. Sample *a* exhibits the smallest semi circle whereas sample *e* exhibits the largest semi circle.

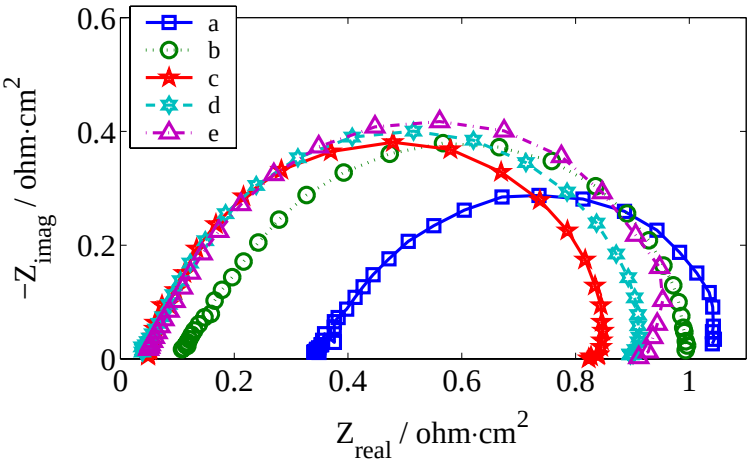

Figure 5.16: AC-impedance of IrO_2 catalysts as a function of annealing temperature. Measured at room temperature and anodic current of i = 20 mA · cm^{-2}.

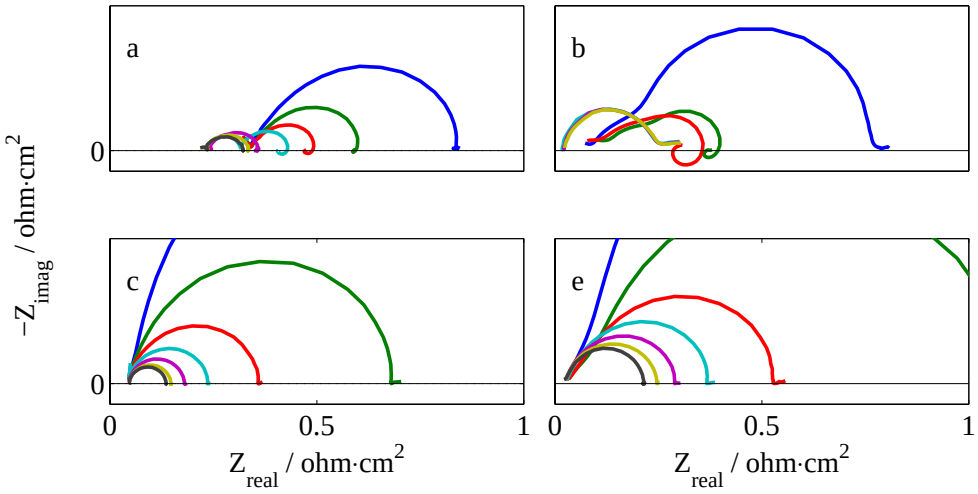

Figure 5.17: AC-impedance at increasing potentials from 1.52-1.64 V_{RHE} at 20 mV increment. a: Not annealed; b: 440 °C, c: 490 °C, e: 540 °C. All figures presented on the same scale.

The impedance behaviour at different potentials of sample *a*,*b*, *c* and *e* can be

seen in figure 5.17. For sample *a* it is observed that R_p decreases at increasing potentials according to a "normal" charge transfer resistance. However, the semi circles are shifted towards lower values along the real axis, which means that R_Ω decreases for higher potentials. R_Ω remains at a constant value of 0.34 $\Omega \cdot cm^2$ in the potential range 1.52-1.56 V_{RHE} and then starts to decrease down to 0.23 $\Omega \cdot cm^2$ from 1.58 to 1.60 V_{RHE} where it remains constant for higher potentials. A small inductive loop at lower frequencies below the real axis is formed at 1.54 V_{RHE} which disappears again at 1.60 V_{RHE}. This loop will be further commented below. For sample *c* and *e* R_p decreases continuously according to "normal" charge transfer for all potentials and no major shift in R_Ω takes place. Similar behaviour was also found for the sample annealed at 510 °C.

The impedance behaviour of sample *b* is quite different from the other samples. The large semi circle decreases much faster than for any of the other samples and the small inductive loop at low frequencies is also present on this sample at potentials of 1.54 and 1.56 V_{RHE}. The impedance behaviour changes radically at potential of 1.58 V_{RHE} and above, where a sudden shift towards lower values of R_Ω takes place together with the formation of a new semi circle. This semi circle does not change by increasing potentials and the impedances obtained between 1.58 and 1.64 V_{RHE} are superimposed on each other. These changes can be shown more clearly from the Bode-plot where the time constants are better distinguished. The Bode-plot of sample *b* can be seen in figure 5.18 measured at potentials of 1.45, 1.50 and 1.64 V_{RHE}. It is observed that the time constant related to the charge transfer reaction at lower frequencies, τ_1, disappear for higher potentials. The time constant at high frequency, τ_2, also decreases by increasing potential until 1.58 V_{RHE} where a sudden change to a potential independent time constant take place. Sample *a* showed only one time constant for all potentials in the Bode-plot, attributed to the charge transfer reaction. Sample *c*, *d* and *e* also showed a second time constant at higher frequencies similar to sample *b*, however, much smaller in magnitude compared to sample *b* and only visible at potentials lower than 1.47 V_{RHE}.

The impedance measured at different potentials were fitted to the circuit $R_\Omega(R_1C_1)(R_{ct}C_{dl})L$. The model fitted the data of sample *b* satisfactorily only within the potential range of 1.45 to 1.50 V_{RHE}, where successful iteration were obtained. A linear relation between E_{RHE} and $1/R_{ct}$ on a logarithmic scale indicate Tafel behaviour, where the reaction rate is controlled by an electrochemical reaction. Figure 5.19 shows a logarithmic plot of E_{RHE} vs. $1/R_1$ (τ_2) and $1/R_{ct}$ (τ_1) of sample *b*, and a linear relation can be observed. This indicate that also the high frequency time constant can be attributed to an electrochemical reaction. Only sample *b* showed a distinct potential dependent time constant at high frequency over a wider potential range. The Tafel slope of the low frequency time constant was found in the same manner for all the samples and are given in table 5.4 together with the R_Ω from fitting of the impedance spectra. The Tafel slopes from the impedance correlates well with the Tafel slopes found from the steady state

polarization measurements also shown in table 5.4.

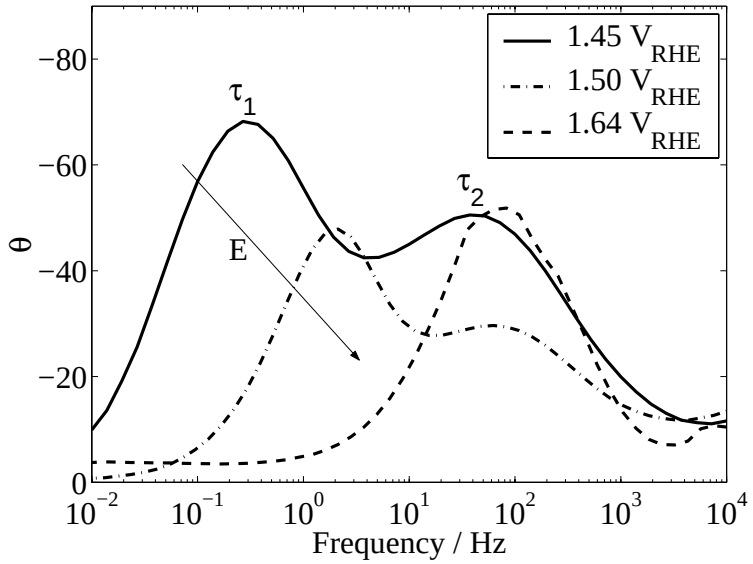

Figure 5.18: Bode plot sample c at 1.45, 1.50 and 1.64 V_{RHE}.

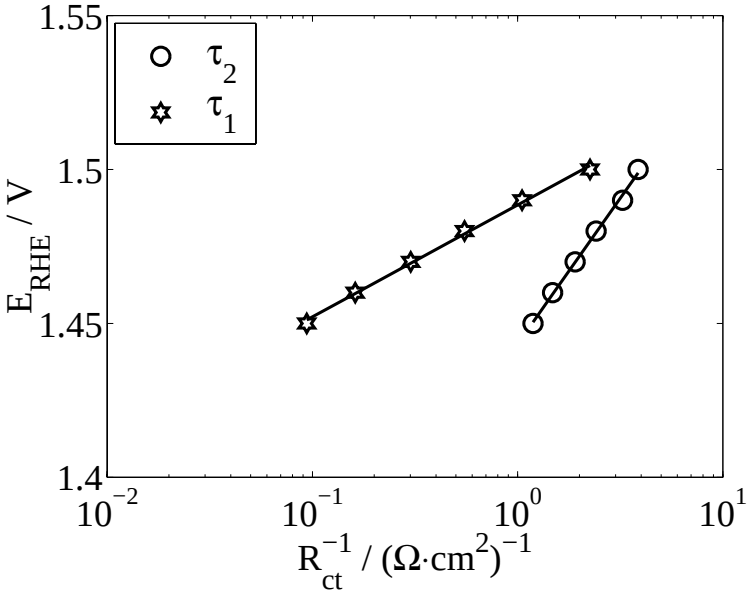

Figure 5.19: Potential as a function of $1/R_{ct}$ on a logarithmic scale.

In figure 5.20 C_{dl} (includes both double layer- and pseudo-capacitance) as a function of potential, found from fitting of the impedance data is shown. C_{dl} is much larger for sample *a* and *b* and increases for increasing potentials, whereas C_{dl} for samples *c*, *d* and *e* are smaller and almost independent of the potential. It can be noted that the potential dependence of C_{dl} for sample *a* changes at 1.50 and 1.55 V_{RHE}. The α-value of the CPE element, given by equation 2.39 changed between 0.9 and 1, which indicate a capacitive behaviour. The capacitance found by AC-impedance is somewhat lower than the capacitance found by voltammetry in table 5.3.

Stationary polarization curves

The current density-potential behaviour of the different samples are shown in figure 5.21. These curves are shown without ohmic drop correction since the electrical conductivity of the metal oxides is of major interest here. It can be seen that the potential curve of sample *a* and *b* shows a steep increase at higher cd. At low cd the potential increases for samples of higher annealing temperature. At high cd a drastic decrease in the potential take place for samples *c*, *d* and *e*, annealed at 490 °C and above.

Sample *c*, annealed at 490 °C, shows the best performance, i.e. highest voltage efficiency at high cd, proven by lower potentials. The Tafel slopes at low and high cd are shown in table 5.4 after correction of IR-drop by R_Ω given in the same table. A slope of 89 $mV \cdot dec^{-1}$ were found at intermediate cd for sample a, which increase to more that 200 $mV \cdot dec^{-1}$ for high cd. The uncorrected and the IR-corrected polarization curve of sample *c* is shown in figure 5.22, together with the Tafel line, and it can be seen that the IR-drop constitutes a performance-loss of almost 100 mV at 2 $A \cdot cm^{-2}$. The slope at high cd is calculated from very few data points and, thus, the assumption of a straight line and purely Tafel behaviour becomes rather uncertain.

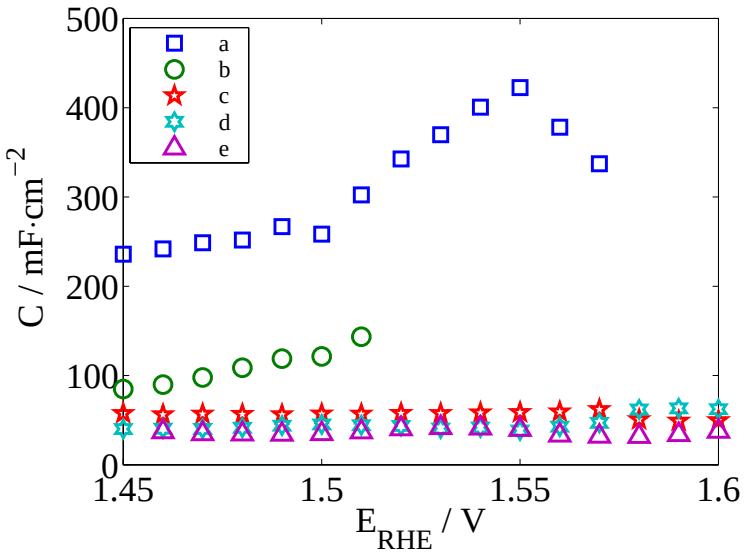

Figure 5.20: Capacitance as a function of potential found by fitting of impedance data.

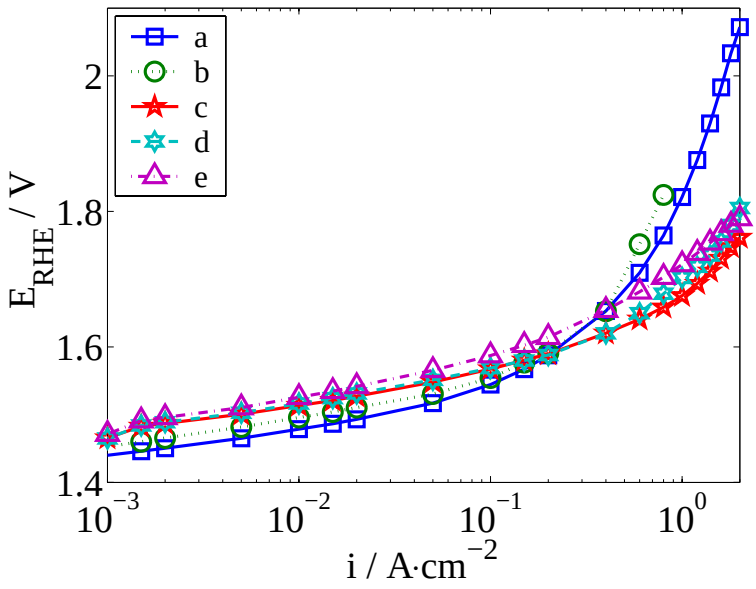

Figure 5.21: Steady state polarization curves of IrO_2 catalysts as a function of annealing temperature. Measured under galvanostatic control. a: Not annealed; b: 440 °C, c: 490 °C, d: 510 °C, e: 540 °C.

Table 5.4: Tafel constants from steady state polarization measurements and R_Ω from fitting of impedance data.

	Polarization curves		AC-impedance	
Sample	b_a at low cd ($mV \cdot dec^{-1}$)	b_a at high cd ($mV \cdot dec^{-1}$)	b_a ($mV \cdot dec^{-1}$)	R_Ω ($\Omega \cdot cm^2$)
a	36	89 → 200	36	0.15-0.34
b	43	> 400	38 / 95	0.09-0.11
c	46	145	42	0.05
d	47	151	44	0.05
e	49	146	48	0.05

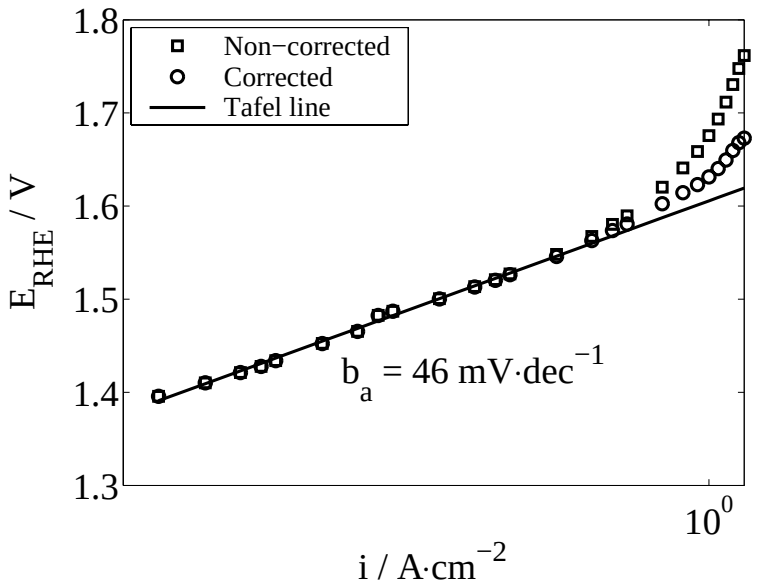

Figure 5.22: Polarization curve corrected for IR-drop and polarization curve not corrected for-IR drop. Sample c, annealed at 490 °C.

5.2.3 Discussion

The TEM images indicate that after the initial calcination stage the majority of the particles are amorphous with a particle size up to 20 nm and that only a minor fraction of the smallest particles has become crystalline. After the annealing stage at 490 °C, particle growth have taken place and small crystallites with high degree of crystallinity are formed within each particle.

The SEM photo in figure 5.14 reveal that most important changes between the different samples takes place on a nm-scale, since no changes can be detected on a μm-scale. Probably, the samples consist of a mixture of relatively large particles on a μm-scale and much smaller particles on a nm-scale. This is agreement to what observed by Hutching *et* al. [101] who prepared mixed oxides of Sn, Ru and Ir by the Adams method.

The voltammogram of sample *a* resembles that of anodically grown oxide of iridium, which can be identified by the narrow hydrogen region between 0 and 0.4 V_{RHE} and a relative broad oxygen region [34]. Anodically grown oxide of Ir indicates that metallic Ir is the main component after the calcination stage due to uncomplete IrO_2 formation, which also have been reported for thermally prepared IrO_2 electrodes in the literature [57, 118]. This means that the precursor probably only decompose to metallic Ir and not by the reaction with $NaNO_3$ according to equation 2.60 and 2.61. Lodi *et* al. [118] investigated the formation of metallic Ir for thermally prepared IrO_2 of DSA-type electrodes and found that when pyrolysing at 400 °C and annealing at 400, 500 and 600 °C for 15 h, a high content of metallic Ir was found at low annealing temperature, whereas the Ir metal content decreased on the cost of increased IrO_2 formation at higher annealing temperature. A similar process have probably taken place in this work, even though the preparation techniques differs significantly.

Since anodically formed hydroxide is more porous than thermally prepared oxides and because the interior of the bulk oxide is available for the charging reaction [51], a larger area of the voltammogram is obtained for the non-annealed sample compared to the annealed samples in figure 5.15b to 5.15e. The decrease in voltammetric charge after annealing is due to particle growth and sintering and to the formation of a dry oxide with strong oxide bridge bonding where protons only can access grain boundaries, crevices and cracks [90]. However, as the metal oxide also becomes more crystalline with increasing crystal lattice and more stoichiometric at increasing annealing temperature, a lower density of the active sites will be formed as the distance between the active sites increases. Increased oxide bridge bonding between the metal ion and oxygen will also take place as the annealing temperature is increased, and further deactivate the oxide catalyst by binding with the d-electrons which participate in the electrochemical reaction [48].

The semi circle from the impedance measurements measured at low cd, confirms what was obtained from the voltammgrams, i.e. an apparently lower electrocatalytic activity at increasing annealing temperature. However, additional information about the ohmic resistance cannot be obtained from the voltammograms, unless the ohmic resistance is very high and lead to separation of the peaks. Samples *a* and *b* must exhibit quite different electrical properties from the samples annealed at higher temperatures, since the electrical resistance decreases for higher potentials. At higher cds, some dissipation of heat and increase in temperature will take place due to the ohmic resistance. The ohmic resistance of semiconduc-

tors will decrease for higher temperatures, which may explain the reduced ohmic resistance of sample *a* and *b* since IrO_2 have been reported to show semiconducting behaviour [38, 43]. Metallic conductivity is probably first obtained after annealing at 490 °C and above, since these samples show insignificant change in ohmic resistance at high cd. The ohmic resistance of sample *c*, *d* and *e* are also much smaller and therefore less influenced by dissipation of heat. The electrical conductivity IrO_2 is very complex [44] and attempting to explain the observed behaviour of the ohmic resistance only become speculations.

Sample *b* exhibits a much steeper increase in potential at high cd compared to sample *a*, even though R_Ω is lower for sample *b*, which suggest that the steep potential increase of sample *b* is being caused by other factors than only the ohmic resistance. Total occupation of active sites is not very likely on sample *b*, since a relatively high capacitance was found. If the assumption about semi conducting properties of sample *a* and *b* is correct, the steep increase in potential of sample *b* may be caused by saturation of charge carriers. Saturation of charge carriers is likely to take place at lower cds for sample *b* than for sample *a*, since annealing will reduce the semiconducting properties. The impedance behaviour of sample *b* also differ from sample *a* by the a high frequency time constant and the formation of a new time constant at higher potentials, independent of the potential. That the high frequency time constant measured at low potentials is caused by the same physical process as the time constant for potentials above 1.58 V_{RHE} is not very likely, since they possess very different potential behaviour. The steep increase in potentials of sample *b*, actually takes place at approximately the same potential where the formation of the potential independent time constant is observed, and it is therefore tempting to believe that this time constant is related to blocking of charge carriers.

Samples *c* to *e*, annealed at 490 °C and above, exhibit a more "normal" impedance behaviour according to what is expected on metallic conductive electrodes, i.e. constant ohmic resistance and a decreasing semi circle by increasing overpotentials. Annealing at 490 °C or more results in crystalline IrO_2 with high degree of metallic conductivity. Increased electrical conductivity and lower density of active sites at increasing annealing temperature corresponds well with the formation of a more ordered crystal structure. The c-axis of the unit cell of the crystal will increase at higher annealing temperature and further enhance the metallic conductivity according to what is described in section 2.5.

The small inductive loop at low frequency appeared very clearly on sample *a* and *b*. Such behaviour can be found for electrochemical reactions involving adsorbed intermediates competing for active reaction sites and have been reported for the corrosion of iron [119] and the ORR [120, 121]. According to the Electrochemical Oxide Path in section 2.4.2, the two adsorbed intermediate species involved are S-OH and S-O. This means that both the last two steps of the reaction path are slow at potentials where the loop appears. The Tafel slope from the impedance of

sample *a* and *b* are below 40 $\text{mV} \cdot \text{dec}^{-1}$, which indicate that the reaction rate is partly determined by the last step in the reaction path. The Tafel slope of sample *c*, *d* and *e* are 40 $\text{mV} \cdot \text{dec}^{-1}$ or more and the rate is mainly determined by the second reaction step, where only the S-OH intermediate is involved. Apparently, no competition of active sites at increasing potentials will therefore take place on sample *c*, *d* and *e*, which is confirmed by the absence of the low frequency loop.

A lower Tafel slope was found on sample *b* from the impedance results compared to the steady state polarization measurements. The equivalent circuit normally used to describe the OER on IrO_2 electrodes takes into account only two time constants, where the time constant at high frequencies is usually attributed to porosity effects and/or intrinsic properties of the oxide layer (see section 2.5) and show no Tafel behaviour. Sample *b*, however, showed clearly two time constants that possessed Tafel behaviour, which indicates that at least two steps in the reaction path limits the reaction rate on this sample. The Tafel slope related to the high frequency time constant was measured to be 95 $\text{mV} \cdot \text{dec}^{-1}$, which probably may be attributed to the electrochemical adsorption step influenced by the back reaction. It is also possible that the transfer coefficient, α, of the adsorption step differ from 0.5. The adsorption step will strongly be influenced by the surface properties of the catalyst, and annealing will certainly create different surface properties and influence the adsorption step. This time constant was also observed on sample *c*, *d* and *e*, however, to a much lesser extent compared to sample *b*. The high frequency time constant may explain why a somewhat higher Tafel slope is found from the polarization measurements compared to the impedance measurements shown in table 5.4. Sample *b* show the largest discrepancy between the Tafel slopes, where a significant contribution of the high frequency time constant take place even at lower potentials.

On sample *a*, no time constant at high frequency was detected within the potential range investigated and the Tafel slope at low cd was the same when measured from the impedance and polarization measurements. A Tafel slope of 89 $\text{mV} \cdot \text{dec}^{-1}$ on sample *a* was found from the polarization curve at higher cds, which indicates that the process related to the high frequency time constant also takes place on sample *a*, however, only at higher cd where impedance measurements becomes obscured by bubble formation. Similar Tafel constants have been reported in the literature. Gottesfeld *et* al. [38] investigated the electrochemical properties of anodically grown hydroxide on Ir and found a Tafel slope of 50 $\text{mV} \cdot \text{dec}^{-1}$ for all cd at thick oxide films and, after anodically dissolution of the oxide film, a Tafel slope of 90 $\text{mV} \cdot \text{dec}^{-1}$ was observed at low cd and 150 $\text{mV} \cdot \text{dec}^{-1}$ for high cd. A Tafel slope of approximately 150 $\text{mV} \cdot \text{dec}^{-1}$ found on sample *c*, *d* and *e* at high cd may also be related to the adsorption step, influenced by gas bubbles or an α different from 0.5.

When annealing the catalyst at a higher temperature, different processes may occur. Presumably, a high degree of metallic Ir, together with some Ir oxides of

lower valence, is formed after the pyrolysis stage. At increasing annealing temperatures the oxide formation take place in the order $Ir_2O_3 \rightarrow IrO_2$ at increasing temperatures [40]. Non-stoichiometry formed by mixtures of Ir(III) and Ir(IV) is among the most important factors that govern the catalytic activity of these types of catalysts, where defects at the surface are assumed to be the catalytically active sites. Increasing the annealing temperature decreases the number of defects, both in bulk and at the surface. A reduced number of defects within the bulk oxide decreases the semiconducting properties and reduced density of defects at the surface reduces the number of active sites [38]. However, as the annealing temperature increases, a more ordered crystal structure is formed and the c-axis of the rutile structure increases which facilitate a higher metallic conductivity

Lodi *et* al. [122] studied the microstructure and electrical properties of IrO_2 prepared by thermal decomposition of $IrCl_3 \cdot xH_2O$ and found that the electrical resistivity decreased by increasing annealing time and temperature, and that the particle size increased by increasing temperature, both during the pyrolysis and the annealing stage. The electrical resistance was believed to depend on both crystallinity and particle size (smaller particles provide more particle boundaries). The growth of particles was much more sensitive to the temperature during the pyrolysis stage than during the annealing stage. In this work high electrical conductivity has been obtained without sacrificing the number of active sites by increased stoichiometry or by particle growth when annealing at 490 °C, which indicates a good compromise between active sites and ohmic resistance. Sample *b* however, annealed at 440 °C, seems to have obtained properties of a semiconductor with too low density of charge carriers and insufficient metallic conductance. Even though the electrochemical area of sample *b* seems to be favourable with respect to capacitance and voltammetric charge, an annealing temperature of 440 °C is too low to obtain the necessary electrical conductivity. Crystallinity and high electrical conductivity of metal oxide catalysts are also important in order to obtain stable performance and long service life. High electrical conductance will prevent the potential field of penetrating into the bulk of the oxide, thus, leaving the bulk of the oxide unaffected [123].

In the literature, the discussion about these type of oxides is traditionally based on work using the DSA technique, where the main focus is on the voltammetric charge and not so much on the electrical conductivity. To understand why this becomes different, one has to consider the difference in design of the two systems. In appendix in figure B.1 a SEM photo of a porous Ti-current collector is shown where the diameter of the wide-open pores ranges from 10 to 50 μm. Figure B.3 shows a cross section image of an MEA, where the anode layer is on the left side and the cathode layer on the right. It can be seen that the layers are about 10 μm in thickness and the membrane about 100 μm. Thus, the thickness of the layers are about the same size as the pore size of the current collectors. The sketch in figure 5.23 shows the principal differences between a catalytic layer and current collector/substrate contact of an MEA and of a DSA electrode. Current must be

transported in lateral direction of the layer as well as in the perpendicular direction to reach the catalytic active zone of the MEA, while on DSA electrodes only perpendicular electron transport is important due to a continuous underlaying substrate of the catalytic layer with a typical thickness of about 2 μm [57]. This results in a much higher specific current density through the catalytic layer of an MEA compared to a DSA electrode and, thus, the electrical conductivity becomes considerably more important of SPE systems. Figure B.2 also shows a SEM photo of a catalytic layer after electrochemical measurements and the morphology of the surface is similar to the morphology of the Ti-sinter. This shows that the uniformity of the catalytic layer will be strongly influenced by the morphology and porosity of the Ti-sinter. Since there is no continuous contact between the catalytic layer and the current collector, this interface contact has to be optimized to obtain a compromise between electrical contact and transport of water/gas to and from the catalytic layer. Thus, the properties of the Ti-sinter is an important topic in SPE water electrolysis, which must be taken into account.

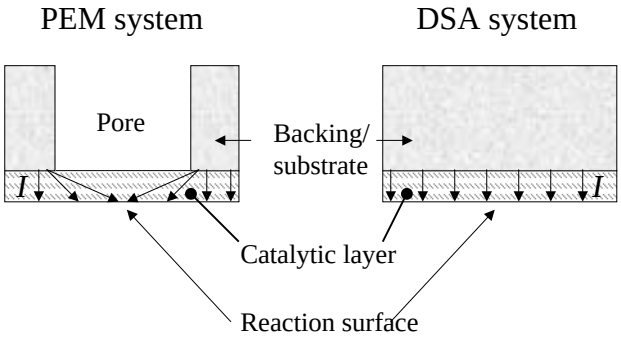

Figure 5.23: Current distribution of catalytic layers of a porous and continuous substrate.

The catalytic layers in SPE systems contain in addition an electrical insulating binder material, which also increase the ohmic resistance in the catalytic layer. In work reported on reversible SPE fuel cell systems, it has been observed that when preparing a bi-functional electrode for oxygen evolution and hydrogen oxidation, the electrode became more active towards oxygen evolution when mixing IrO_2 with Pt-black [78], even though Pt-black is considerably less active towards oxygen evolution than IrO_2. This can probably be explained by an increase in electric conductivity of the catalytic layer.

These results shows in general the principal limitations and interpretation of how to improve the performance of catalysts in SPE water electrolyser, rather than a

final answer. Choosing slightly different conditions during preparation procedure will result in different initial state of the catalysts and, hence, the optimum annealing temperature will possibly change. The optimum time of annealing will change for different temperatures, e.g. longer time will be needed for lower temperatures and shorter time for higher temperatures.

5.2.4 Summary

A major part of metallic Ir is formed after the calcination step at 340 °C and further annealing is necessary for IrO_2 formation to take place.

Optimum annealing conditions of the IrO_2 catalyst, prepared by the Adams method was found to be close to 490 °C, where the best compromise between density of active sites and electrical conductivity was found. Too careful annealing at 440 °C may cause conductivity problems of the oxide, where the metal oxide becomes partly transformed from a semiconductor to a metallic conductor. Increasing the annealing temperature decreases the apparent activity and increases the electrical conductivity.

High electrical conductivity of the catalysts is important in SPE systems due to the porous design of the current collectors, where current transport must take place in lateral direction of the catalytic layer as well as in perpendicular direction. This results in a longer current path and a lower cross section for electron transport compared to what is apparently observed. Thus, electrical conductivity of the catalysts in SPE electrolysis is of outmost importance.

5.3 Characterization of Ir-Ta mixed oxides as anode catalyst

This section describes the electrochemical characterization of the IrO_2 - Ta_2O_5 mixed oxide as anode catalyst as the composition is varied from 100 to 50 mole% Ir.

The binary catalyst system of Ir-Ta mixed oxide was studied for different compositions and annealing conditions. Since increasing content of Ta_2O_5 will suppress the crystallisation of IrO_2 [99], a higher annealing temperature is necessary to obtain the same degree of crystallinity of the IrO_2 phase at increasing content of Ta_2O_5. A certain degree of crystallinity of the IrO_2 must be present to obtain high electrical conductivity of the oxide, however, the annealing temperature must be kept below a certain value to avoid particle growth and sintering and the formation of an oxide with too high stoichiometry, as was shown in section 5.2. Therefore the catalyst samples were divided into two fractions of high and low Ir content of 100 - 65 and 65 - 50 mole% Ir. The samples of high Ir content were annealed at 500 °C, which was approximately the optimum annealing temperature of pure IrO_2, as shown in section 5.2. The fraction of low Ir content was annealed at 550°C which was found to be the optimum annealing temperature for the IrO_2-Ta_2O_5 system in 70 - 30 mole% ratio using the DSA technique [85].

5.3.1 Experimental

The catalyst samples were prepared by the Adams method by calcination at 340 °C for 30 minutes and further annealed for 8 hours. Electrochemical characterization were performed using voltammetry, AC-impedance and steady state polarization. Sample *d* was investigated by TEM and compared to a pure IrO_2 sample annealed at 500 °C, already shown and discussed in section 5.2. All measurements were performed at room temperature. Detailed description of the methods is given in section 4.

Compositions and annealing temperature of the different samples are given in table 5.5

5.3.2 Results

Transmission Electron Microscopy

TEM image of sample *d* is shown in figure 5.24 with a diffraction image in the upper left corner. The white unit-line in the black field represents 20 nm in length. For comparison, the TEM image of the pure IrO_2 annealed at the same temperature, is shown in the same figure at the lower left corner. It is observed

Table 5.5: Composition and annealing temperature of the samples.

Sample	mole% Ir	Annealing temperature (°C)
a	100	500
b	95	500
c	90	500
d	85	500
e	65	500
f	65	550
g	60	550
h	55	550
i	50	550

that the particle of sample *d* consists of small crystallites which are smaller than that of the pure IrO_2 sample. The diffraction image suggests that the pure IrO_2 sample is more crystalline than the mixed sample. The particles of the mixed sample was approximately in the same range as the pure sample, i.e. 20-100 nm in diameter.

Voltammetry

Figure 5.25 shows the voltammograms of the samples as a function mole% Ir. The peak attributed to the Ir(III)/Ir(IV) redox couple at approximately 0.9 V_{RHE} is slightly suppressed compared to the peak attributed to the Ir(IV)/Ir(VI) redox couple at 1.35 V_{RHE} of the samples *b* - *i*. The voltammetric charge more or less continuously decreases for decreasing mole% Ir, until 60 mole% where a small increase take place of samples with 55 and 50 mole% Ir.

AC-impedance

The Nyquist plots of the samples annealed at 500 and 550 °C are shown in figure 5.26 and 5.27 respectively. It is observed that R_p increases from sample *a* to *c*, decreases from *c* to *d* and then increases again for sample *e*. A clear change in impedance behaviour have taken place already after addition of 5 mole% Ta. Samples *f* to *i*, annealed at 550 °C, shows a much more well defined impedance behaviour and R_p increases continuously for decreasing mole% Ir. The impedance behaviour of *e* and *f* is very different, despite the same molar ratio of Ir and Ta. A considerable decrease in both R_p and R_Ω has taken place as a result of the increased annealing temperature from 500 to 550 °C. The values of R_Ω are summarized in table 5.6 and show that R_Ω increases for decreasing mole% Ir

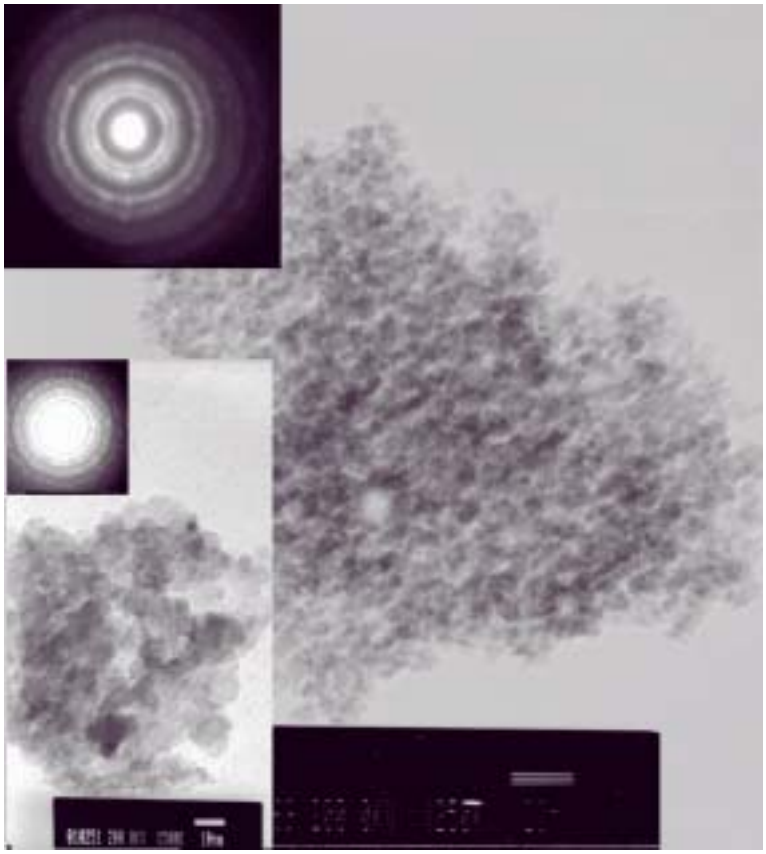

Figure 5.24: TEM and diffraction image of sample 85 mole% Ir. Figure in lower left corner shows TEM and diffraction image of a pure IrO_2 sample.

for samples *a* to *e*, and that R_Ω is more or less constant for samples *f* to *i*. The presence of an inductive loop at low frequencies can also be seen for these samples, as described in section 5.2.

Steady state polarization and open circuit behaviour

The polarization curves were corrected for IR-drop by R_Ω from the impedance measurements and the Tafel slopes were found at high and low cd, given in table 5.7. i_0 on OER is very difficult to measure, and finding i_0 from equation 2.20 requires the value of E^{rev}, which is rarely obtained. E' is expressed by b_a, i_0 and E^{rev} according to equation 2.21, which was found by modelling the data to equation 2.20 and the values are given in table 5.7. Samples *b* - *d* exhibit a low

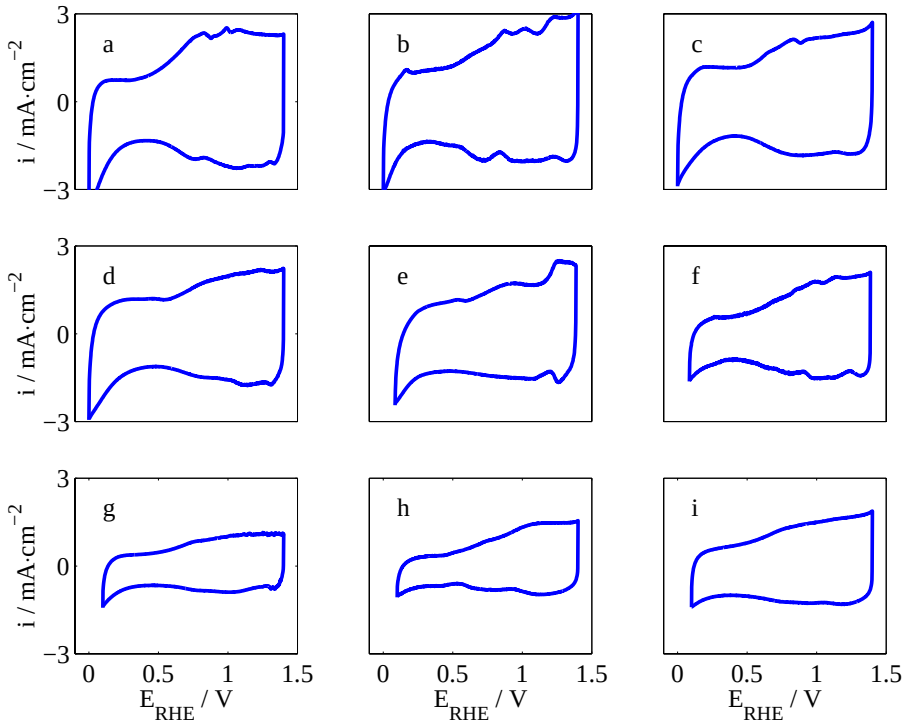

Figure 5.25: Voltammetry of the IrO_2 - Ta_2O_5 catalysts as a function of mole% Ir. Recorded at room temperature at 20 mV $\cdot$ s^{-1}. a) 100 mole%, b) 95 mole%, c) 90 mole%, d) 85 mole%, e) 65 mole%, f) x = 65 mole%, g) 60 mole%, h) 55 mole%, i) 50 mole%. Samples *a* - *e* annealed at 500°C and samples *f* - *i* annealed at 550°C.

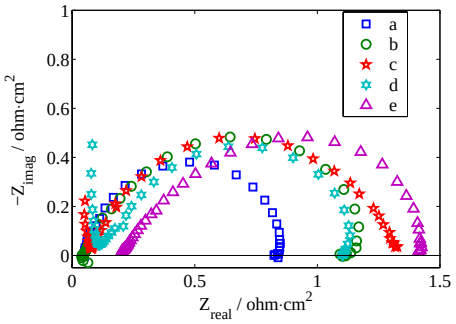

Figure 5.26: Nyquist plot as a function of mole% Ir for samples annealed at 500 °C. a: 100 mole% Ir, b: 95 mole% Ir, c: 90 mole% Ir, d: 85 mole% Ir, e: 65 mole% Ir.

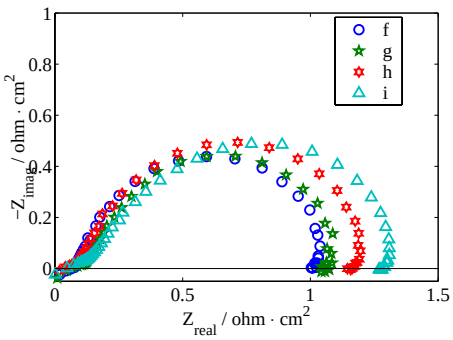

Figure 5.27: Nyquist plot as a function of mole% Ir for samples annealed at 550 °C. f: 65 mole% Ir, g: 60 mole% Ir, h: 55 mole% Ir, i: 50 mole% Ir.

Table 5.6: Ohmic resistance from AC-impedance as a function of composition.

Sample	R_Ω ($\Omega \cdot cm^2$)
a	0.05
b	0.05
c	0.09
d	0.12
e	0.20
f	0.09
g	0.11
h	0.09
i	0.11

Tafel slope of about 30 $mV \cdot dec^{-1}$ at low cd followed by a relatively steep increase in the slope of more than 300 $mV \cdot dec^{-1}$ at higher cd. The samples *b* - *e* exhibits a smaller Tafel slope at low cd compared to the samples from *f* to *i*, whereas for high cd the samples *b* - *e* exhibits a much steeper slope than the samples *f* - *i*. The lowest value of E′ was found for samples *a* to *e*, however, no systematic variation within these samples can be seen. For the samples *f* - *i* it can be seen that E′ increases systematically with decreasing mole% Ir, which probably corresponds to a decreasing i_0. The polarization curves for all samples, not corrected for IR-drop, are shown in figure 5.28 .

The OCP values are also given in table 5.7 and it can be seen that the OCP correlates somewhat systematic with the Tafel slope and increase to above 0.9 V_{RHE} for b_a of approximately 30 $mV \cdot dec^{-1}$ and decreases to 0.9 V_{RHE} or below for b_a of 40 $mV \cdot dec^{-1}$ or more. Sample *d* exhibits the highest OCP value.

From the polarization curves it can be seen that sample *d*, of 85 mole% Ir, exhibits the best performance of the samples proven by lowest potentials for intermediate and high cd.

5.3.3 Discussion

The TEM image shows that the addition of 15 mole% Ta has a large influence on the crystallite size and morphology of the particles. This is consistent with the literature [99] where Ta_2O_5 was found to be enriched at the crystallite surface of IrO_2 and to suppress the crystallite growth. The crystallization is also suppressed by the presence of Ta_2O_5 [99] (see section 3.2), which is confirmed by the diffraction images. It can be concluded that the effect of crystallite size and crystallinity

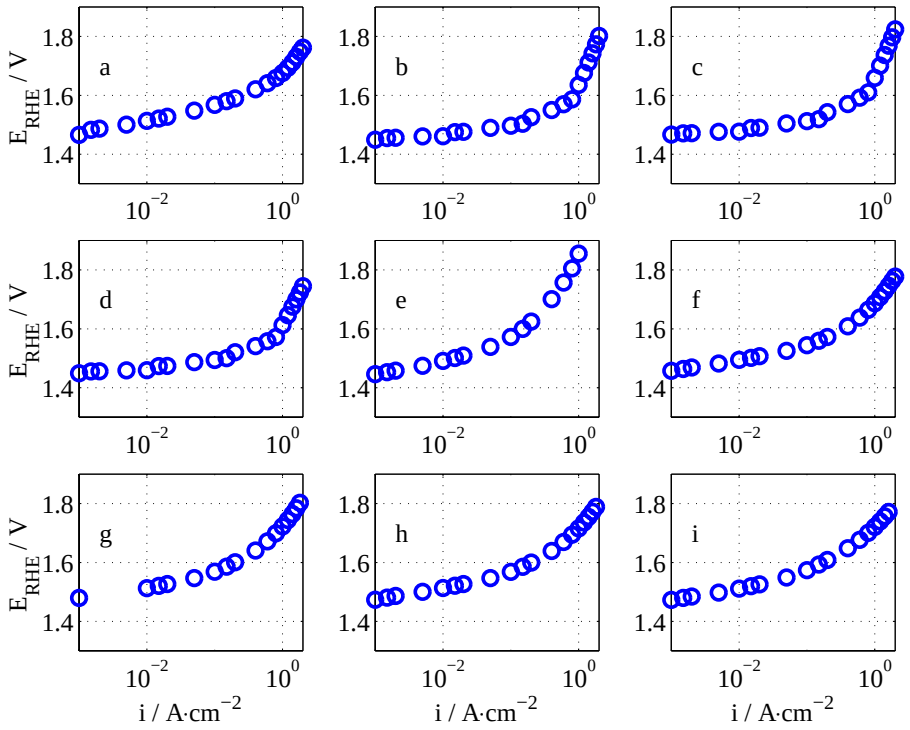

Figure 5.28: Polarization curves as a function of x. a: x = 1.00, b: x= 0.95, c: x = 0.90, d: x = 0.85, e: x = 0.65, f: x = 0.65, g: x = 0.60,h: x= 0.55, i: x = 0.50. a - e: annealed at 500 °C, f - i: annealed at 550 °C.

Table 5.7: Tafel slopes and open circuit potential as a function of composition .

Sample	E′ (V_{RHE})	b_a at low cd ($mV \cdot dec^{-1}$)	b_a at high cd ($mV \cdot dec^{-1}$)	OCP (V_{RHE})
a	1.542	40	-	0.904
b	1.528	32	-	0.917
c	1.543	30	-	0.954
d	1.533	30	-	0.956
e	1.584	44	152	0.914
f	1.571	37	152	0.886
g	1.592	45	150	0.870
h	1.595	41	130	0.851
i	1.605	42	117	0.898

of the IrO_2 - Ta_2O_5 mixed oxide prepared by the DSA technique, also take place when the mixed oxide is prepared by the Adams method.

The low Tafel slopes obtained on samples *b* to *d* suggest a relative change in the rate of two or more sub-processes. According to section 2.4.2, a lowering in b_a may corresponds to a change in the reaction path. It is possible that a change in reaction mechanism have taken place, where step 2.42 changes to 2.45. To verify this, it is necessary to measure the reaction order at constant potentials ($\nu(H^+)_E$), which is difficult within the SPE environment. The presence of Ta in the oxide lattice of Ir may increase the average valence of Ir ions by withdrawal of electrons and increase the affinity towards oxygenated intermediate species. This is consistent with increased OCP and lower b_a, where rds is moved further down the route. A similar behaviour have also been found by Alves *et* al. [34] for the $Ir_{0.3}Ti_{0.7-x}Ce_xO_2$ system, where b_a was found to be 30 $mV \cdot dec^{-1}$ for all compositions ($0 \leq x \leq 0.7$) whereas the OCP changed by x and showed a maximum for intermediate x. A change in Tafel slope may also be related to the very small crystallite size, as was found by TEM. The reaction will preferably take place on defects, kinks and crack and at the corners of the crystallites. For smaller crystallites the active sites becomes closer to each other and facilitate the rearrangement step and the recombination step becomes the rds where a lower Tafel slope will be obtained, according to section 2.4.2.

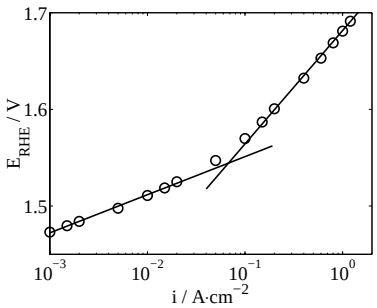

Figure 5.29: IR-corrected polarization curve of sample *i*.

Apparently, a decrease in the electrical conductivity have taken place when IrO_2 was mixed with Ta_2O_5, as can be seen from the values of R_Ω in table 5.6. In addition to being an electrical insulator, Ta_2O_5 suppresses the crystallization process of IrO_2 and results in a more disordered amorphous structure which again decreases the electrical conductivity. A purely resistive relationship would not be a linear slope in a logarithmic scale and the very high slope at high cd of samples *b* to *d* cannot be explained by the R_Ω values alone and, as was suggested in section 5.2, additional effects must be taken into account. It is possible, however, that these samples also possesses a high degree of semiconducting properties which becomes limiting to the reaction for high cd, e.g. saturation of charge carriers. However, it is also likely that the rds has changed and an increase in the Tafel slope have taken place for such high cd.

Sample *e* and *f* for 65 mole% Ir were annealed at 500 and 550 °C respectively, and from table 5.6 it can be seen that R_Ω decreased from 0.20 to 0.09 $\Omega \cdot cm^2$. Compared to the results in section 5.2 where R_Ω of the samples annealed at 490 and 540 °C was almost the same, a much more dramatic influence of the annealing temperature is obtained when Ta is present in the oxide matrix. The lower slope at

high cd of samples *f* to *i* is probably caused by the increased annealing temperature and higher electrical conductivity, and for these samples R_Ω show no systematic increase by increasing Ta content.

Most literature data reports a b_a-value on IrO_2 based electrodes in the range of 40-90 $mV \cdot dec^{-1}$ [38, 124, 95, 125, 126] and 150 $mV \cdot dec^{-1}$ for higher cds [38], which also was found in section 5.2. It is interesting to observe that for low Ir content, the high Tafel slope decreases down to 117 $mV \cdot dec^{-1}$ for 50 mole% Ir, which could correspond to step 1 as rds in the reaction path. The IR-corrected polarization curve of this sample is shown in figure 5.29.

That Ta suppresses crystallization and particle growth of IrO_2 by enriching at the surface, suggests that the IrO_2 particles becomes shielded by the inactive component, which may explain the decrease in the voltammetric charge as the Ta content is increased. However, for samples *g* - *i* the voltammetric charge increases slightly as the Ta content increases, which may be caused by an increased dispersion of the active catalyst. The peak at 0.9 V_{RHE} is slightly decreased relative to the peak at 1.35 V_{RHE} for the samples mixed with Ta. This may be related to the withdrawal of electrons from the Ir ion, which increases the charging current of the Ir(IV)/Ir(VI) redox couple. This may be a complementary explanation to the higher activity of the for samples *b* - *d* for low and intermediate cd, where the OER take place more easily when involving the Ir(IV)/Ir(VI) redox transition. It has been reported in the literature that moving the main peak of Ir catalysts towards the onset of O_2 evolution enhances the catalytic activity [38]. The Ir(IV)/Ir(VI) redox peak is very clearly shown on sample *e* for 65 mole% Ir annealed at 500 °C. Increasing the annealing temperature to 550 °C of this catalyst decreases the Ir(IV)/Ir(VI) peak, as seen from sample *f* in figure 5.25.

Sample *d* of 85 mole% Ir showed the highest voltage efficiency, proven by lowest potentials for cd below 1 $A \cdot cm^{-2}$, which was achieved by a best compromise between i_0, b_a and R_Ω for these samples. All these parameters are strongly influenced by both composition and annealing temperature as discussed above. As revealed by the diffraction image in figure 5.24 sample *d* was less crystalline than pure IrO_2, annealed at the same temperature. The performance of sample *d* can probably be further enhanced for higher cd by increasing the annealing temperature to obtain higher degree of crystallinity and electrical conductivity. Additions of Ta had a much stronger influence on particle size and crystallinity than first expected. To complete this series, optimum annealing conditions with respect to time and temperature should be obtained for each composition. Taking the preparation conditions into account as well, a huge matrix of measurements must be performed to reveal the optimum preparation, composition and annealing conditions.

The results from this work is different from what obtained in the literature where the main enhancement of the mixed oxide was related to formation of needle shaped IrO_2 crystallites on a layer of cobblestone shaped amorphous phase of

Ta_2O_5, strongly influenced by the initial state of the substrate [85]. By the Adams method the most important enhancement by addition of Ta species is mainly related to reduced crystallite size and possible withdrawal of electrons from Ir atoms in the oxide lattice for low Ta content, where stoichiometry of Ta oxide can be different from Ta_2O_5. For higher Ta content it is possible that shielding of active Ir-sites have taken place, probably by accumulation of Ta_2O_5 at the crystallite surface of the IrO_2 rich phases. The loading of IrO_2 was kept constant for all the samples, which means that the total catalyst loading increases for increasing content of Ta, i.e. thicker catalytic layer for samples of higher Ta content. This was not further studied, however, it must be taken into account for further optimization of the mixed oxide catalyst.

Additions of other species than Ta can possibly be interesting for further work. To obtain the same effects as for Ta species, the metal ion of the added species should be able to withdraw electrons from the Ir atom and must also be stable in the acidic PEM environment.

The main purpose for mixing Ta_2O_5 with IrO_2 in DSA based electrodes is to improve the life time performance by reducing the corrosion of Ir where less active electrodes are accepted [85]. Shielding of the IrO_2 rich phase by Ta_2O_5, may indeed be effective for reduced corrosion of Ir. Probably, the catalysts with higher Ta content will also be more stable than the catalysts with low Ta content. For cds as high as 2 $A \cdot cm^{-2}$ the potential difference between sample *d* (85 mole% Ir) and *i* (50 mole% Ir) is less than 80 mV and for 1 $A \cdot cm^{-2}$ the difference is about 110 mV. This means that the catalyst composition must be chosen according to the operational conditions of the electrolyser. For more advanced electrolysers with internal cooling and well protected metallic interfaces and backing material, where high cds of 2 $A \cdot cm^{-2}$ or more can be applied, a composition with 50 mole% Ir content may be preferred. For simpler electrolysers, which operates at 1 $A \cdot cm^{-2}$ or below and where corrosion of the active catalyst is less pronounced, a catalyst composition of 85 mole% Ir may be preferred. In any case the life time performance of these catalysts must be evaluated and further cost optimization will determine the preferred properties of the catalyst according to the wanted operational conditions for the electrolyser.

5.3.4 Summary

Additions of Ta species to IrO_2 were found to enhance the catalyst performance for low contents of Ta. This was attributed to suppressed crystallite growth and possible withdrawal of electrons from the Ir atoms, which increases the adsorption of oxygenated intermediate species and facilitates a lower Tafel slope. Other additives may be of interest for further studies.

Best performance at 1 $A \cdot cm^{-2}$ and below was found for the mixed oxide with additions of 15 mole% Ta, attributed to a best compromise between i_0, b_a and R_Ω.

Probably even better performance can be obtained for this catalyst by increasing the annealing temperature. For high cds of 2 $A \cdot cm^{-2}$ or more the potential difference between the catalysts of low and high Ta content becomes less pronounced and a higher Ta content may be preferred under more severe operating conditions. Further studies of this binary catalyst using higher Ta content and different preparation/annealing conditions can be interesting for further work.

5.4 Characterization of Ir-Ru mixed oxides as anode catalyst

This section discusses the anodic behaviour of the mixed oxides of Ir and Ru as a function of composition.

IrO_2 based catalysts are recognised to be more stable in acidic environment than RuO_2 based catalysts [127]. Composition of higher Ir content is preferred for technical applications due to longer service life of Ir rich samples and the composition range have therefore been studied for 50 - 100 mole% Ir.

5.4.1 Experimental

The samples were studied by *in situ* electrochemical measurements in the NTNU-cells using voltammetry, AC-impedance and stationary polarization curves. The metal oxide catalysts were prepared by the Adams method. Surface characterization was performed by N_2 adsorption using the BET - isotherm. For detailed description see section 4. The Ir content of the samples are shown in table 5.8. All samples were prepared at 450 °C and annealed at 400 °C for 40 hours. A higher preparation temperature was chosen than the series described in section 5.2 and 5.3 to obtain the metal oxide and to avoid metallic formation directly from the precursors. Annealing at 400 °C for 40 hours has been reported to be the optimum annealing conditions with respect to electrical conductivity of IrO_2 [122].

Table 5.8: Mole % Ir of samples.

Sample	mole % Ir
a	100
b	90
c	80
d	70
e	60
f	50

5.4.2 Results

BET measurements

The results from BET measurements are shown in table 5.8 and the surface area decreases from 65 to 50 $m^2 \cdot g^{-1}$ from 90 to 60 mole% Ir respectively and then

increases again for sample with 50 mole% Ir. The data indicates that the surface area slightly decreases for decreasing content of Ir. Sample *a* was unfortunately not included.

Table 5.9: BET measurements

Sample (mole %)	BET ($m^2 \cdot g^{-1}$)
90	65
80	63
70	55
60	50
50	59

Voltammograms

The voltammogram of the samples are shown in figure 5.30. A larger particle size was obtained for the mixed samples, which was noticed during the preparation. For some of the samples a small rest of particles were left in the air gun after MEA preparation. This resulted in a somewhat lower loading of some of the samples. However, the shape of the voltammograms can still be compared. It can be seen that the shape of samples *b* - *e* are very similar and they all differ significantly from sample *a*.

The peaks of IrO_2 at 0.90 and 1.35 V_{RHE}, attributed to the redox couples of Ir(III)/Ir(IV) and Ir(IV)/Ir(VI) respectively, are flattened out even for 90 mole% Ir. The current density at the onset of oxygen evolution increased considerably in the presence of the Ru component.

AC-impedance

The impedance measurements showed little change between the mixed samples, however, the mixed samples differ significantly from the 100 mole% Ir sample. The results from some of the samples are shown in figure 5.31. It is observed that sample *a* exhibits a much smaller R_p compared to sample *b*, *d* and *f* and that the three latter samples are very similar to each other, despite the difference in Ir content of 90, 70 and 50 mole% respectively. Sample *b* differ from sample *d* and *f* by the presence of the low frequency loop, which also can be seen on sample *a*. The Bode-plot reveal that there are at least two time constants, one within the frequency range 1 Hz - 10 Hz and a second time constant within 10 - 100 Hz. A few impedance measurements were performed at higher potentials and no potential dependence of R_Ω was found for any of the samples.

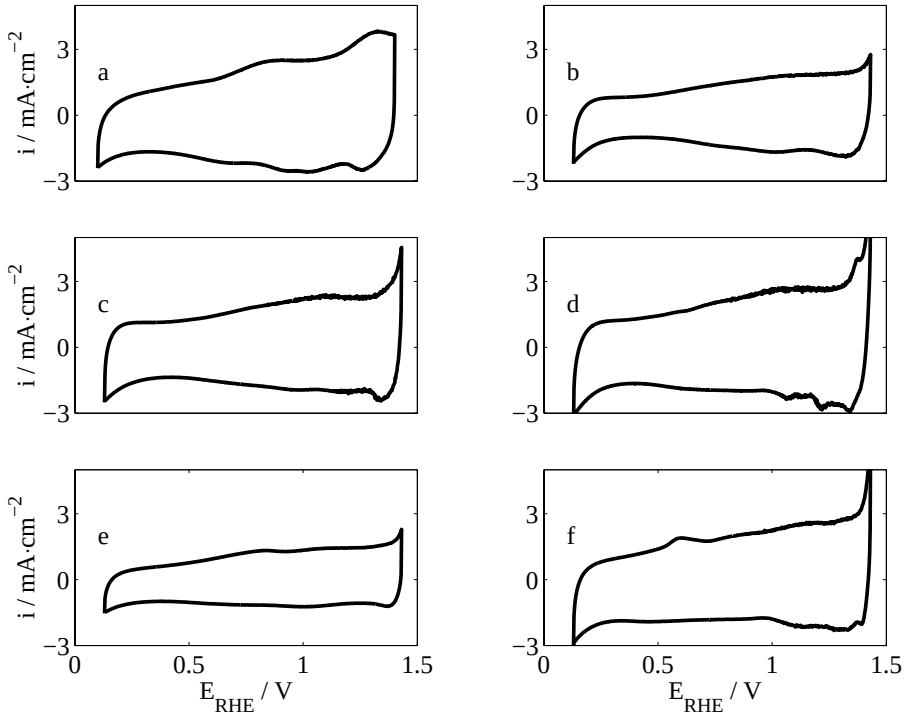

Figure 5.30: Voltammograms measured at 20 $mV \cdot s^{-1}$ and room temperature. Mole % Ir: a: 100 % Ir, b: 90 % Ir, c: 80 % Ir, d: 70 % Ir, e: 60 % Ir, f: 50 % Ir.

Table 5.10: R_Ω as a function of composition.

Mole% Ir	R_Ω ($\Omega \cdot cm^2$)
100	0.08
90	0.05
80	0.07
70	0.05
60	0.08
50	0.05

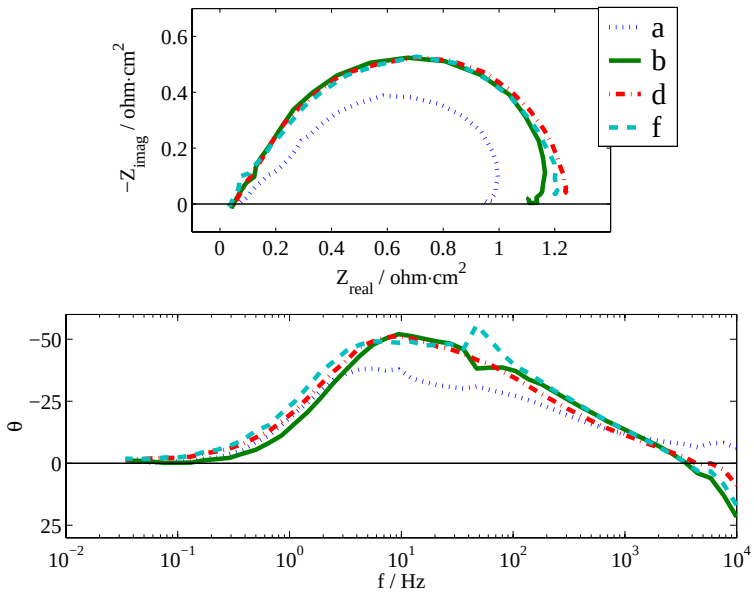

Figure 5.31: Nyquist- and Bode plot. a: 100 mole% Ir, b: 90 mole% Ir, d: 70 mole% Ir, f: 50 mole% Ir. Measured at 20 mA $\cdot$ cm^{-2} at room temperature.

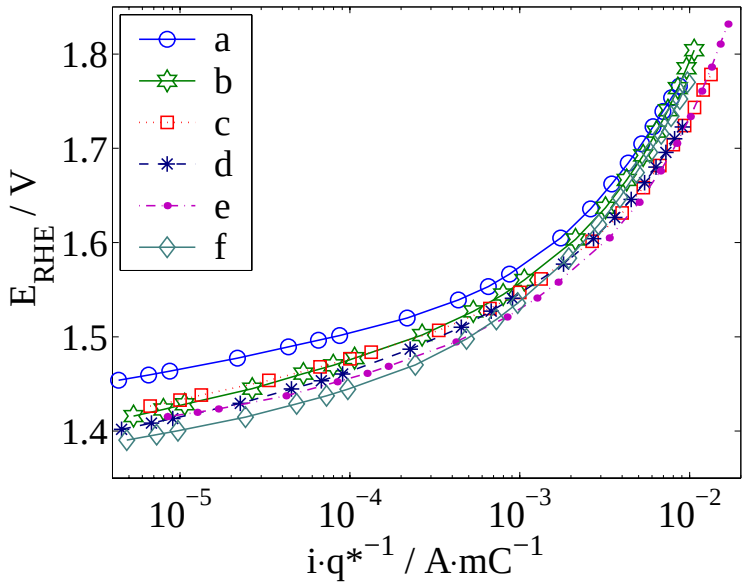

Figure 5.32: Potential versus i/q* for all x. Measured under galvanostatic control at room temperature. Mole % Ir: a: 100 % Ir, b: 90 % Ir, c: 80 % Ir, d: 70 % Ir, e: 60 % Ir, f: 50 % Ir.

Polarization curves

Due to an uneven loading of the electrodes, the current density was corrected by the voltammetric charge, q*, found by integrating the voltammograms between 0.4 and 1.4 V_{RHE}. The curves were also corrected from IR-drop by R_Ω obtained from AC-impedance. The corrected polarization curves are shown in figure 5.32 and it can be seen that at low cd the potential increases more or less continuously for increasing content of Ir, which corresponds to a decrease in i_0. The curves are shifted towards lower potentials at all cd for decreasing mole% Ir except sample *f* of 50 mole% Ir, where the potential increases more steeply at high cd and intercept the curves of higher Ir content.

The Tafel slope at low and high cd was found after IR-correction and are given in table 5.11. The Tafel slope at low cd increases from 36 to 46 $mV \cdot dec^{-1}$ after addition of 10 mole% Ru. For further additions of Ru, the Tafel slope decreases from 46 to 40 $mV \cdot dec^{-1}$. The slope at high cd is about 150 $mV \cdot dec^{-1}$ for 100 and 90 mole% Ir and decreases to about 130 and 120 $mV \cdot dec^{-1}$ for 80 and 70 mole% Ir respectively. The slope then increases to 163 $mV \cdot dec^{-1}$ at 60 mole% Ir and increases further to 191 $mV \cdot dec^{-1}$ for 50 mole% Ir. Thus, the slope at high cd shows a minimum for 70 - 80 mole% Ir.

The potential measured at 2 $A \cdot cm^{-2}$ is given in table 5.11 as a measure of the voltage efficiency/performance. However, the data must be interpreted with care due to different loading of the samples and shows no systematic variation with mole% Ir.

Table 5.11: Tafel slopes and E_{RHE} at 2 $A \cdot cm^{-2}$ without correction of IR-drop.

Ir content (mole %)	b_a at low cd ($mV \cdot dec^{-1}$)	b_a at high cd ($mV \cdot dec^{-1}$)	E_{RHE} at 2 $A \cdot cm^{-2}$ (V)
100	36	150	1.766
90	46	152	1.804
80	44	130	1.778
70	43	121	1.722
60	40	163	1.832
50	40	191	1.770

5.4.3 Discussion

BET analysis shown in table 5.8, suggests that the particle size increases for increasing content of Ru, where smaller active area indicate larger particles. Increased particle size was also confirmed during the preparation of MEAs, where

a non-transparent layer was difficult to achieve and where some of the particles segregated before preparation was completed. Formation of larger particles when adding the Ru-precursor can probably be explained by stronger affinity towards oxygen for RuO_2 ($\Delta G_f^0 = -253$ kJ $\cdot$ mole^{-1}) compared to IrO_2 ($\Delta G_f^0 = -188$ kJ $\cdot$ mole^{-1}) [14] where RuO_2 is probably formed at an earlier stage than IrO_2. It is possible that the presence of Ru during the pyrolysis stage changes the precipitation kinetics where RuO_2 may act as a nucleus for the precipitation of IrO_2.

The shape of the voltammograms changes in a rather sudden way after mixing 10 mole% Ru into the oxide of Ir. From 90 to 50 mole% Ir, the shape is more or less the same, which indicates that the electrode kinetics becomes determined by the behaviour of Ru already after 10 mole% Ru. A sharp increase in cd of the voltammograms at about 1.35 V_{RHE} take place for the samples containing Ru, more typical of the RuO_2 catalyst where the onset of O_2 evolution starts at lower potentials compared to IrO_2 [48]. The voltammograms of Ir-Ru mixed oxides typically shows a maximum in q* for intermediate compositions [128, 93], which arises as a consequence of diminished probability of homogeneous crystal growth [93]. The change in q* as a function of composition is not possible to determine for these samples as the loading differs. The BET analysis rather suggests that a minimum in surface area has been obtained for intermediate compositions. This discrepancy is probably related to the very different preparation technique used in this work compared to literature data.

At low i/q*-values, E_{RHE} decreases continuously for increasing mole% Ru, which is in agreement with increasing content of the more active RuO_2 catalyst, which exhibits higher i_0 than IrO_2. The i/q*-values are comparable to what observed by Mattos-Costa *et* al. [93] at low cds and shows approximately the same i/q*- E_{RHE} behaviour. The potentials in this work was measured up to 2 A $\cdot$ cm^{-2}, whereas Mattos-Costa *et* al. measured only to 100 mA$\cdot$cm^{-2}, thus, ohmic resistance effects are more important in this work and must be taken into account. The i/q* - E_{RHE} plot corrected for IR-drop is a measure of the electrocatalytic behaviour and the most favourable kinetics at high cd is possessed by the 60 mole% Ir sample. From table 5.11 it can be seen that the best real performance, which takes into account surface area and ohmic drop effects, was obtained by the 70 mole% Ir sample at $E_{RHE} = 1.722$ V at 2 A$\cdot$cm^{-2}. This corresponds to a higher voltage efficiency and a better performance than the pure IrO_2 catalyst annealed at 490 °C and IrO_2 - Ta_2O_5 catalyst of 85 mole% Ir. If all samples had been successfully prepared and equal loading obtained, the 60 mole% sample would probably shown better real performance as well.

The Nyquist- and Bode plots in figure 5.31 shows that the impedance behaviour of the mixed electrodes differ from the pure IrO_2 electrode. This can probably be related to different rds of the mixed and the pure IrO_2 sample, and a lower density of active points that hinder the recombination of intermediates and, thus, increases the R_p. This is also in accordance with the Tafel slope of 36 mV $\cdot$ dec^{-1} of the

100 mole% sample, where the reaction rate probably becomes partly determined by the last step in the reaction path. This is also confirmed by the low frequency loop shown in figure 5.31, which suggests that at least two reaction intermediates are competing for reaction sites. The similar shape of the impedance spectra of the mixed electrodes indicates that they possesses similar surface properties.

The Bode-plot reveals that at least two rate determining steps are present for all samples. It was shown in section 5.2 that the Tafel slope attributed to the high frequency time constant and determined the reaction rate for high cd, also took place for low cd. The change from low to high Tafel slope take place by a gradual transition for increasing cd on the Ir-Ru oxide samples, which probably corresponds to increasing surface coverage and a gradually larger influence by the process attributed to the high frequency time constant. This transition probably take place at lower cd on the Ir-Ru particles than on pure IrO_2 particles, since the former possessed much larger particles and lower surface area. A Tafel slope much higher than 120 $mV \cdot dec^{-1}$ may be attributed a value of α different from 0.5. On these samples however, R_Ω does not change for higher cds, and the steep potential increase of sample with 50 mole% Ir must be attributed to other effects than electrical conductivity. It is possible that the surface coverage approaches 1, and saturation of active sites take place for high cd of this sample.

Measuring AC-impedance over a large potential range, as was performed in section 5.2, is very time consuming and only a few impedance spectra of each sample were measured at higher potentials, mainly to check for potential dependence of R_Ω. Two impedance spectra were measured at 1.50 and 1.52 V_{RHE} of each sample. Performing a very simple modelling on these two spectra, as shown in section 5.2, and finding the slope of E_{RHE} vs. $\log(1/R_{ct})$ results in 43 and 192 $mV \cdot dec^{-1}$ of the 70 and 50 mole% Ir samples respectively. This indicates that the process related to the high slope starts below 1.50 V_{RHE} on 50 mole% Ir and causes the very steep increase in potential already at intermediate cd. Effects of porosity, surface heterogenity, diffusion etc. as described in section 2 must probably be taken into account to describe this time constant. Only two impedance spectra is not enough information to draw any conclusions. However, the striking agreement between the slopes from impedance and polarization measurements indicates that impedance can be used to determine the potential behaviour of the different processes that limits the reaction. Attributing the time constants to specific physical and chemical processes that take place at the electrode will give a better opportunity to modify the catalyst to exhibit the desired properties.

In most literature data, b_a changes from 40 to 60 $mV \cdot dec^{-1}$ as the composition is changed from pure RuO_2 to pure IrO_2 respectively [129, 48, 93]. The same trend seems to take place in this work, if not taking the 100 mole% Ir sample into account. However, the increase in the low Tafel slope, from 40 $mV \cdot dec^{-1}$ of the Ru rich samples to higher values of b_a for Ir rich samples, starts to take place first when the Ir content reaches 80 mole%, which is at a higher Ir content than what

is reported in the literature.

The large influence of the Ru component and the similar behaviour between the mixed samples suggests that accumulation of Ru at the crystallite surface have taken place. Segragation of Ir to the surface has been reported in the literature where the mixed catalysts were prepared by thermal decomposition and annealed at temperatures in the range of 400-450°C at 1-3 hours [101, 130, 128]. Segregation of Ir at the surface has been explained by the larger ionic radii of Ir^{4+} (0.077 nm) compared to Ru^{4+} (0.076 nm), where expansion forces segregation of Ir^{4+} to the surface. This is probably not very likely to take place for such a small difference of ionic radii. Another explanation can be the higher oxidation potential of ruthenium, which facilitate crystallisation of RuO_2 at an earlier stage and IrO_2 to be enriched at the surface in a later stage [101].

No surface segregation was reported on samples prepared by reactive sputtering when electrodes were used as prepared without any further heat treatment [48]. Segregation of Ru to the surface has also been reported in the literature where the samples were first fired at 500 - 700 °C for 6 hours, then grind milled and further annealed for 6 hours [131]. Enrichment of Ru at the particles surface was explained by the more negative ΔH for formation of RuO_2 compared to IrO_2 where Ru was pulled out of the mass to the surface [131]. In this work, enrichment of Ru at the surface have also taken place where annealing was performed at 400 °C for 48 hours. Thus, a much shorter annealing time for the IrO_2 - RuO_2 catalyst system has been reported in the literature where surface enrichment of Ir was detected. It is possible that the discrepancy between Ir and Ru enrichment reported in the literature can be explained by the difference in annealing time. The larger driving force for the formation of RuO_2 may result in precipitation of RuO_2 at an early stage and further precipitation of IrO_2 at a later stage in the initial calcination process, which results in Ir enrichment at the surface. However, Ru may segregate to the surface by slow diffusion during the annealing stage, thus, the particle surface becomes enriched by Ru if sufficient time of annealing is applied. The chemical composition of the mixed catalysts must be analysed by X-ray techniques for different annealing time to reveal that this process take place.

Optimum composition of the mixed oxide Ir-Ru system in SPE electrolysis has been reported by Kötz *et* al. [91] at the Brown Boweri Research Center to be 20 to 50 mole% Ir. In this work, the optimum range was found to be 80 to 60 mole% Ir, which is similar to what reported elsewhere [93, 130]. The variation in optimum composition between literature data and the result obtained in this work, can probably be related to different preparation procedures. For the Adams method used at Brown Boweri Research Center, the calcination stage was performed at 450°C for 3 hours without any further annealing [101]. In this work, a short calcination stage was applied followed by washing and removal of excess salt and at last annealing at 400°C for 40 hours in air. Different interpretation of preparation

routines may lead to different properties of the catalysts and different conclusions. In most work reported on the mixed oxide of Ir and Ru in the literature, life time performance was better with higher content of Ir. Since the Ru component seems to be enriched at the surface of the particles in this work it is possible that corrosion of the Ru may take place more rapidly on these samples compared to what obtained in the literature.

Further work on the binary catalyst system of IrO_2 and RuO_2 must be carried out. Less enrichment of Ru at the surface will be desired with respect to lifetime performance, which probably can be controlled by adjusting the annealing conditions and the preparation procedure in general. A more uniform distribution of Ir and Ru can probably be obtained by decreasing the annealing time, perhaps at even higher temperature.

5.4.4 Summary

The particle surface of the binary catalyst system of IrO_2-RuO_2 was found to be strongly enriched with Ru component when prepared according to the procedure described in this chapter. A more uniform distribution of the components is desired to secure long service life of the catalyst and further studies on the preparation conditions is recommended, e.g. shorter annealing times and higher temperatures.

The most favourable performance was obtained by samples of 80 - 60 mole% Ir. The best real performance data, including IR-drop and surface area effects was obtained by the 70 mole% sample, where E_{RHE} was found to be 1.722 V at 2 $A \cdot cm^{-2}$ and room temperature, which corresponds to the highest voltage efficiency of the best catalysts of pure IrO_2 annealed at 490 °C and the 85 mole% Ir sample of the IrO_2 - Ta_2O_5 catalyst system.

5.5 Cathodes i SPE electrolysis

This section show some different characteristics of the cathode layer in SPE® water electrolysis with respect to different type of catalysts, catalyst loading and content of Nafion® ionomer.

Catalytic layers of Pt on polymer membranes have during the last few decades been a subject to a large research field in connection to SPE® fuel cells. The breakthrough in SPE® fuel cells was mainly due to dispersion of the active Pt catalyst onto a substrate of carbon particles, e.g. Vulcan XC-72, where significant decrease in catalyst loading was obtained from 4 to 0.02 mg Pt $\cdot cm^{-2}$ or less [3]. Cathodes in SPE® electrolysis have proven to be of less importance compared to the anode catalyst and very low overvoltages have been obtained by using different type of preparation techniques [70].

5.5.1 Characteristcs of Pt on Vulcan XC-72

Pt particle size of fuel cell catalysts obtained by Ralph *et* al. [132] are given in table 5.12.

Table 5.12: Pt particle size on Vulcan XC-72 [132].

wt% Pt	Particle size (nm)
10	1.9
20	2.1
40	3.5

SEM measurements of catalytic layers

SEM photo of different catalytic layers of 10, 20 and 40 wt% Pt on Vulcan XC-72 can be seen from the figures 5.33 to 5.38, taken after running the electrochemical measurements. Each sample is shown in two different magnifications of 2000X and 200X. The 40 wt% Pt sample in figure 5.37 appear to be less porous in the main matrix compared to the 10 and 20 wt% Pt samples in figure 5.33 and 5.35 respectively. This indicates that for high Pt wt% on carbon, less porous layers are formed. However, the exact porosity is difficult to determine on this scale and have to be revealed for higher magnifications.

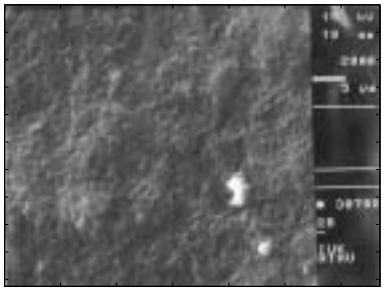

Figure 5.33: SEM photo of 10% Pt on Vulcan XC-72 measured after electrochemical measurements. 2000X magnification.

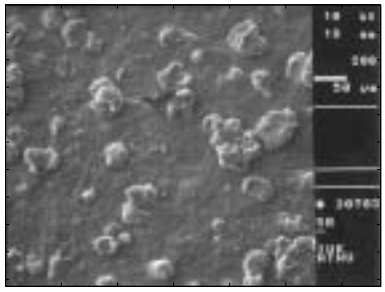

Figure 5.34: SEM photo of 10% Pt on Vulcan XC-72 measured after electrochemical measurements. 200X magnification.

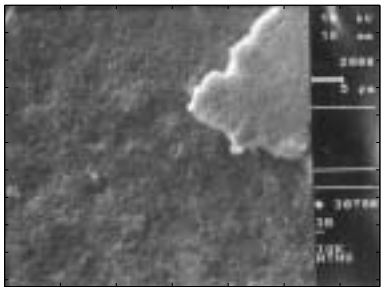

Figure 5.35: SEM photo of 20% Pt on Vulcan XC-72 measured after electrochemical measurements. 2000X magnification.

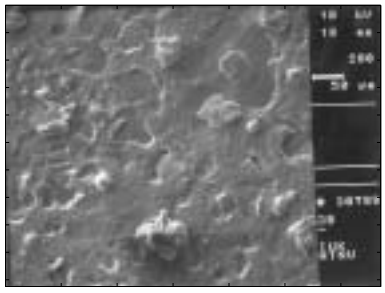

Figure 5.36: SEM photo of 20% Pt on Vulcan XC-72 measured after electrochemical measurements. 200X magnification.

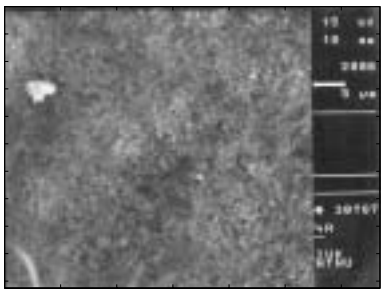

Figure 5.37: SEM photo of 40% Pt on Vulcan XC-72 measured after electrochemical measurements. 2000X magnification.

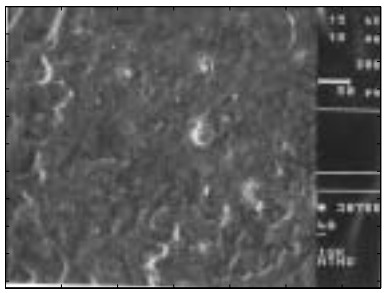

Figure 5.38: SEM photo of 40% Pt on Vulcan XC-72 measured after electrochemical measurements. 200X magnification.

From the photos magnified 200X it can be seen that small clusters are formed within the main matrix. These clusters are much brighter that the main matrix and therefore suggest the formation of Pt rich agglomerates. These clusters are present at the same size and density also before electrochemical measurements and are therefore not a result of cathodic polarization or H_2 evolution. The density of clusters decreases for increasing wt% Pt, which can be seen when comparing figure 5.34, 5.36 and 5.38 of the 10, 20 and 40 wt% Pt catalysts respectively. The clusters size ranges from approximately 5 to 50 μm. Such cluster formation have not been reported before and may therefore be formed during the preparation procedure specific for this work. One explanation can be that the Nafion® ionomer adsorb onto the Pt rich particles and neutralise the electrostatic charge such that electrostatic repulsion between the particles no longer is possible and agglomeration takes place.

A cross section image of a 20 % Pt on Vulcan XC-72 catalytic layer can be seen in figure 5.39. The catalyst was deposited onto the membrane at a total loading of 4 mg $\cdot$ cm^{-2} and the layer thickness is 15 - 20 μm.

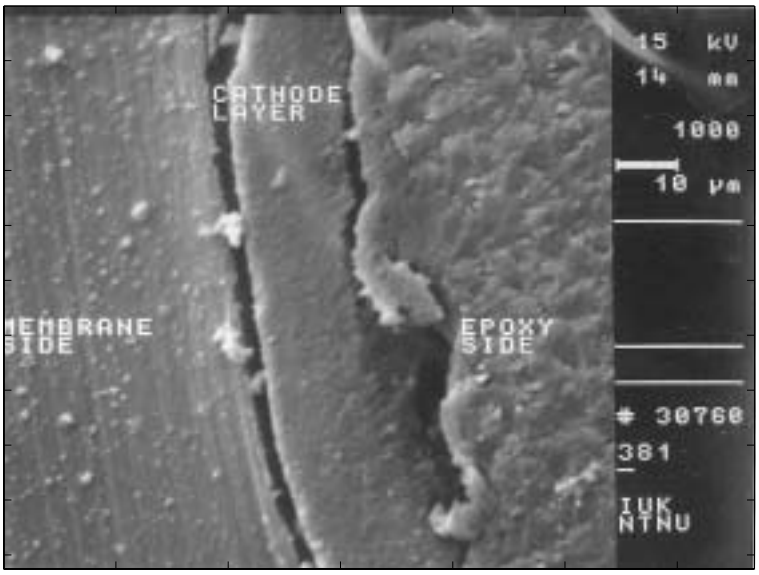

Figure 5.39: Cathode layer of 10% Pt on Vulcan XC-72 at a total loading of 4 mg $\cdot$ cm^{-2}. 1000X magnification.

Effect of loading

20 % Pt on Vulcan XC-72 was deposited at different loadings of 0.15, 0.20, 0.30, 0.40 and 0.80 mg $Pt \cdot cm^{-2}$ using 27 wt% Nafion® ionomer content of all samples. Voltammograms as a function of loading are shown in figure 5.40 and it is observed that the voltammetric current increases as the loading increases. The small figure shows the integrated voltammetric charge of the hydrogen region, q^*_H, measured between 0 and 0.4 V_{RHE}, as a function of Pt loading and it can be seen that q^*_H is not proportional to the Pt loading and the increase becomes less for increasing loadings. This indicates that the catalyst becomes less active further away from the interface between the catalytic layer and the membrane.

The polarization curves in figure 5.41 shows that at high cd the overvoltage decreases as the Pt loading increases from 0.15 to 0.3 $mg \cdot cm^{-2}$ and then start to increase from 0.3 to 0.8 $mg \cdot cm^{-2}$, which indicates an optimum performance close to 0.3 $mg \cdot cm^{-2}$. Boyer *et* al. [133] studied the 20 wt% Pt on Vulcan XC-72 catalyst loading in SPE® fuel cells and found that no further performance was obtained when increasing the Pt loading of more than 0.2 $mg \cdot cm^{-2}$. It is belived that when increasing the catalyst loading too much, there will be an unactive reaction zone at the front of the current collectors, which mostly contributes to increased ohmic drop and transport limitations [132, 134].

The slope of the potential curve at low negative overpotentials ranges from 12 to 20 $mV \cdot dec^{-1}$ for the samples. Supersaturation of H_2 near the interface between Pt and solution and diffusion into the bulk is likely to take place on active Pt electrodes [25], which may explain the low slope where transport of H_2 away from the Pt catalyst becomes the rds and the electrochemical steps in the HER are at equilibrium. For electrodes of high i_0, the back reaction must also be taken into account when measuring the Tafel slope at low η. Maksimov *et* al. [135] found similar behaviour of the HER on Pt particles (3 nm) incorporated into Nafion membrane.

R_Ω was found for the samples by AC-impedance and the values are given in table 5.13. These values were found to be too high when compared with the polarization curves and are probably not representative for the ohmic resistance at high cd. Assuming a Tafel constant of -40 $mV \cdot dec^{-1}$ for high cd and a potential-current density behaviour according to equation 5.1, the R_Ω-values are found to be approximately 10 % less than what found from AC-impedance.

$$E_{RHE} = E^0 + b_c \cdot \log \frac{i}{i_0} - i \cdot R_\Omega \tag{5.1}$$

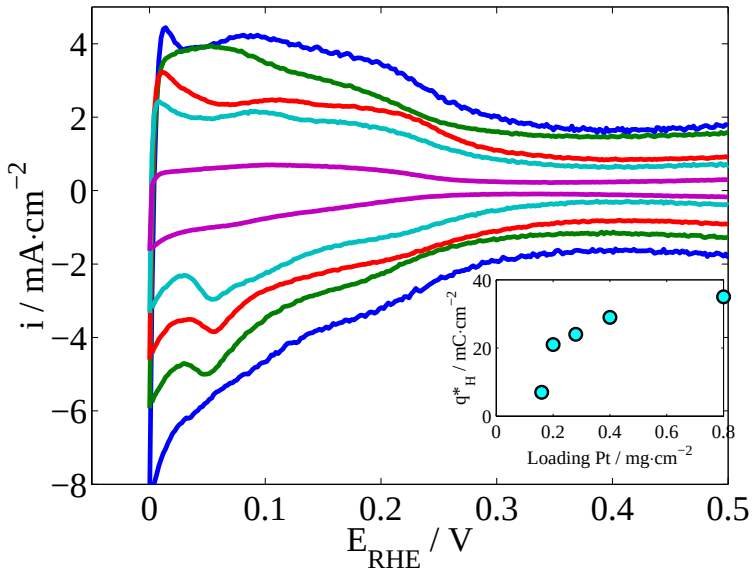

Figure 5.40: Voltammograms of 20% Pt on Vulcan XC-72 at different loadings measured at 20 mV $\cdot$ s^{-1} at room temperature. Loading given as mg Pt $\cdot$cm^{-2}. a: 0.8, b: 0.4, c: 0.3, d: 0.2, e: 0.15.

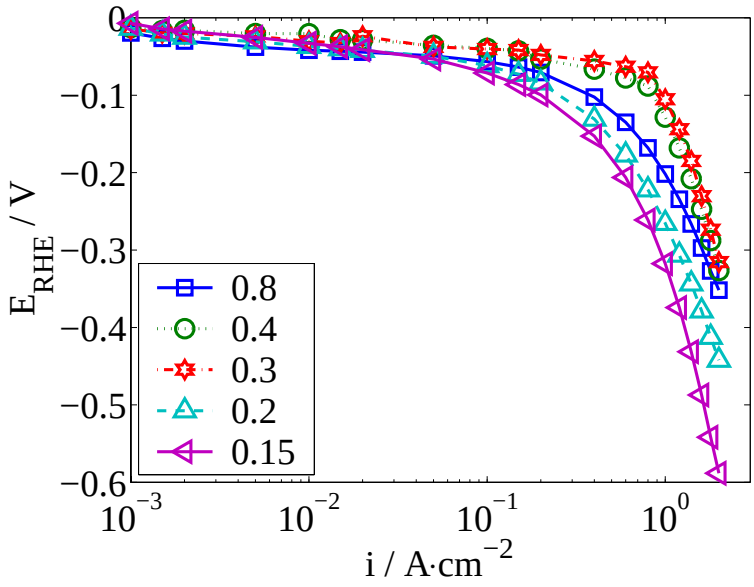

Figure 5.41: Polarization curves of 20 % Pt on Vulcan XC-72 catalyst. Pt loading given in the legend as mg Pt $\cdot$cm^{-2}.

This discrepancy is not observed for anode catalysts (whenever the catalyst possessed purely metallic conductivity) and must be specific to the cathode. Due to water drag, increased wetting of the membrane and catalytic layer will take place for high cd and thereby increase the ionic conductivity and the active area of the otherwise hydrophobic cathode layers. The catalytic layers of Pt catalysts supported by carbon are very hydrophobic, which can easily be seen from a mirror like surface when a dry MEA is introduced into water. This mirror shine is maintained even after boiling the MEA in water for several minutes. After measurements and extensive H_2 evolution, the mirror like surface can be regenerated by first drying the MEA and dipping it into water. Such a high hydrophobicity suggests that release of gas bubbles can become difficult.

As can be seen from table 5.13, R_Ω obtained from AC-impedance does not change according to the thickness of the catalytic layer as normally would be expected. The electrical conductivity of the catalytic layer is a very complex function of the percolating path [68] and also the thickness of the catalytic layer. The current transport of the catalytic layer can be divided into a perpendicular and longitudinally component, as discussed in section 5.2. A lower R_Ω for higher catalyst loading may be explained by increased cross section area for the longitudinally electron transport.

Bubble formation within the pores may take place and increase the ohmic resistance of the catalytic layer at higher cds by expanding the matrix of the catalytic layer [136]. Additional screening of the catalytic sites by bubbles may further lead to higher negative overvoltage [136]. The effect of bubbles within the electrodes seem to be of minor importance since the ohmic resistance rather decrease than increase for high cd. However, screening of active sites for high cd may become a limiting factor if considering the high hydrophobicity of these electrodes.

Table 5.13: R_Ω found by AC-impedance as a function of Pt loading.

Pt loading $(mg \cdot cm^{-2})$	R_Ω $\Omega \cdot cm^2$
0.80	0.16
0.40	0.21
0.30	0.21
0.20	0.26
0.15	0.12

The optimum loading of these cathode layers will differ depending on the method used for preparation. However, it is shown that the catalyst loading have an optimum in accordance with literature data on SPE® fuel cell [133].

Effect of Nafion content in the catalytic layer

The polarization curves as a function of Nafion® wt% in the catalytic layer is shown in figure 5.42 for 20 % Pt on Vulcan XC-72. The negative overpotential decreases from 20 to 25 wt% ionomer and then increases again for 28 and 33 wt%. This show that 25 wt% ionomer is close to an optimum value with respect to performance.

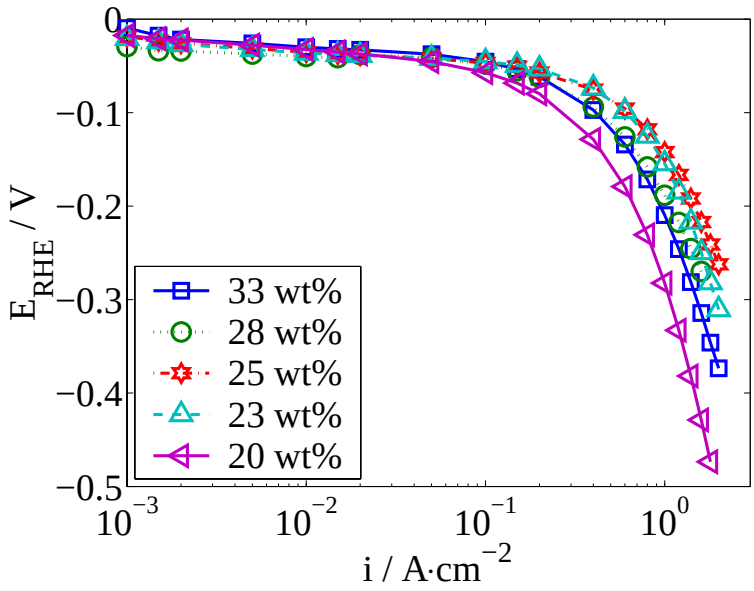

Figure 5.42: Polarization curves as a function of nafion ionomer content. a: 20 wt%, b: 23 wt%, c: 25 wt%, d: 28 wt%, e: 33 wt%.

Table 5.14 shows $q*_H$, measured between 0 and 0.4 V_{RHE}, and R_Ω found the voltammograms from AC-impedance respectively as a function of wt% ionomer. $q*_H$ first increases as wt% ionomer increases, which can be understood from more sulphonic groups available to the Pt adsorption sites. $q*_H$ reaches a maximum of 26 $mC \cdot cm^{-2}$ for 25 wt% and then decreases again for higher wt%. R_Ω is almost unsensitive towards the ionomer content until 33 wt% where a considerably increase take place. R_Ω is a measure of both ionic and electrical conductivity of the catalyst layer and for increasing ionomer content the ionic conductivity increase whereas the electrical conductivity decrease, which can be understood by more isolated particles within the catalytic layers and more dead ends for the electron transport according to the percolation theory [68]. Isolation of particles from electrical contact also explain why $q*_H$ starts to decrease again at higher wt% of the ionomer. Comparing the values of $q*_H$ and R_Ω with the polarization curves, it is clear that additional factors are important. The polarization curves shows that

a better performance is obtained with 33 wt% than with 20 wt% ionomer. Both $q*_H$ and R_Ω indicate better performance of the sample with 20 wt% ionomer. By close inspection of the polarization data it can be seen that the sample of 33 wt% ionomer has the highest potential for low cd, which corresponds to the highest i_0. An increased solubility of H_2 for higher content of the Nafion® ionomer has been reported in the literature [68], which facilitate the escape of H_2 from the catalytic layers.

Table 5.14: Ohmic resistance and hydrogen adsorption charge as a function of wt% ionomer.

Ionomer content (wt%)	$q*_H$ ($mC \cdot cm^{-2}$)	R_Ω ($\Omega \cdot cm^2$)
20	18	0.13
23	23	0.14
25	26	0.14
28	16	0.14
33	15	0.25

Passalacqua *et* al. [68] studied the influence on Nafion® ionomer within the catalytic layer in SPE® fuel cells and found an optimum loading between 25 - 33 wt% using 20 % Pt on Vulcan XC-72, where the performance did not change very much. This optimum was believed to be a best compromise between maximum Pt utilisation and mass transport limitations, where transport limitations were determined by the porosity. The porosity of the catalytic layers of Pt on carbon supported catalysts can be made from 35 % to 65 % by adding pore formers of soluble carbonates, which are removed after MEA-preparation. However, increased porosity is obtained on the expense of electrical conductivity [137].

Comparison between different Pt catalysts supported by Vulcan XC-72

Voltammograms of different wt% Pt on Vulcan XC-72 are shown in figure 5.43. A constant catalyst loading of 0.4 mg Pt $\cdot cm^{-2}$ with 25 wt% Nafion content were used in all samples. It can be seen that the charging current in the H-region is considerably larger for 10 wt% Pt compared to 20 and 40 wt% Pt catalyst, whereas the charging current of the 20 and 40 wt% catalyst are almost the same. The double layer current, however, agree more with the total amount of catalyst applied for each sample.

The electrochemical area (ECA) of the catalysts can be found by using the $q*_H$ value of a plane Pt surface of 210 $\mu C \cdot cm^{-2}$ [24] as shown in equation 5.2.

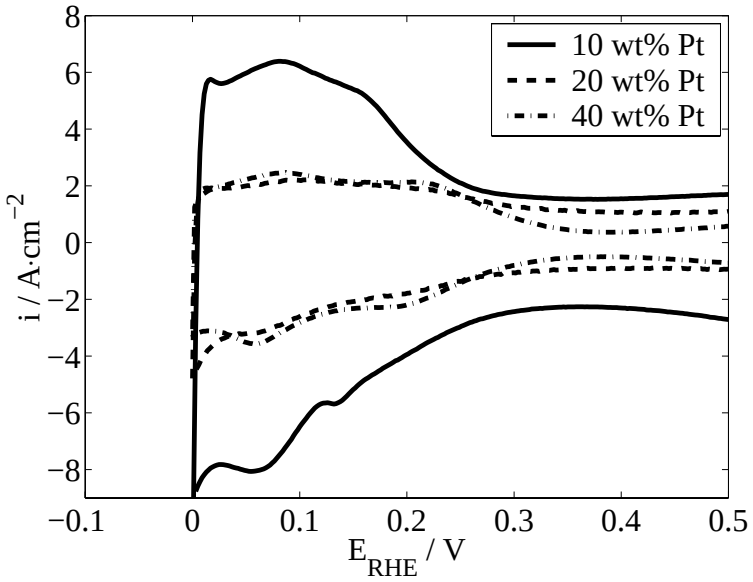

Figure 5.43: Voltammograms of different Pt on Vulcan XC-72 catalysts as a function of wt% Pt. Measured at 20 mV·s^{-1} at room temperature.

$$\text{ECA} = (\text{cm}^2 \quad \text{Pt} \cdot \text{g}^{-1}) = \frac{\text{q*}_\text{H}}{210(\mu\text{C} \cdot \text{cm}^{-2} \quad \text{Pt}) \cdot \text{Loading(g} \quad \text{Pt} \cdot \text{cm}^{-2})} \tag{5.2}$$

Table 5.15 shows the relationship between the electrochemical area (ECA) and the Pt loading on VulcanXC-72. Ralph *et* al. [132] measured the ECA for the same wt% Pt and and the values are given in column to the right in table 5.15. The catalysts were made at their laboratory and the measurements performed in 1.0 M H_2SO_4 aqueous solution and, thus, comparison must be interpreted with care. The aqueous solution should provide better wetting of the catalysts, however, the sulphuric acid solution used by Ralph *et* al. does not necessarily provide the same density of sulphonic groups as the Nafion environment. The significant difference indicates that a relatively large surface area have been obtained by the spraying technique used in this work.

The polarization curves of the different catalysts are shown in figure 5.44 and it can be seen that the best performance is obtained by using 10 wt % Pt on Vulcan XC-72. The 20 wt% sample possess higher negative overpotentials at high cd and shows very similar future as the 10 wt% sample, despite the very different voltammograms and values of ECA obtained for these two samples. Worst performance is obtained by the 40 wt% catalyst, which also shows a quite different shape of the curve. The slope of the electrodes with 10 and 20 wt% Pt is even less than 10

Table 5.15: Relationship between the electrochemical area and the Pt loading on Vulcan XC-72 supported catalyst.

Catalyst (wt % Pt)	ECA ($m^2 \cdot g^{-1}$ Pt)	ECA [132]
10	530	120
20	240	100
40	330	60

$mV \cdot dec^{-1}$. These three samples are the most active cathodes of the respective catalysts obtained in this work.

It has been found throughout in this work that the voltammogram of Pt on carbon catalysts show very bad correlation with the polarization measurements, i.e. the voltage efficiency. The polarization curve of the 20 wt% Pt catalyst possess almost the same behaviour as the 10 wt% sample up to about 0.75 $A \cdot cm^{-2}$, where a sharp transition to a more negative slope take place for higher cd. The voltammogram suggests that the 10 and 20 wt% samples should exhibit very different performance, whereas the polarization curves shows that the performance is very much the same for cds less than 0.75 $A \cdot cm^{-2}$. This discrepancy indicates that the performance at low cd is determined by the catalytic zone near the membrane and that structural effects of the catalytic layers becomes important for high cd. According to the SEM photos the different catalysts showed different morphology with respect to porosity in the main matrix and density of Pt rich clusters. These structural differences may play an important role with respect to ohmic resistance and transport of water/gas through the catalytic layers.

Figure 5.45 shows the Nyquist plot of the three samples, where a characteristic high frequency inductive loop for the 10 and 20 wt% samples can be observed. The 40 wt% sample, however, does not show the presence of the high frequency loop. In general, this high frequency loop is not present on less active electrodes of the Pt on Vulcan XC-72 catalysts. The loop will be further discussed below.

The difference in R_Ω of 0.10 and 0.17 $\Omega \cdot cm^2$ for the 10 and 20 wt% samples may explain the different performance found by the polarization measurements. The preparation of Pt on Vulcan XC-72 catalysts results in quite scattered performance data and different R_Ω from time to time, even when using the same type of catalysts and preparation conditions. This indicates the formation of a complex porous structure with high sensitivity towards the preparation procedure.

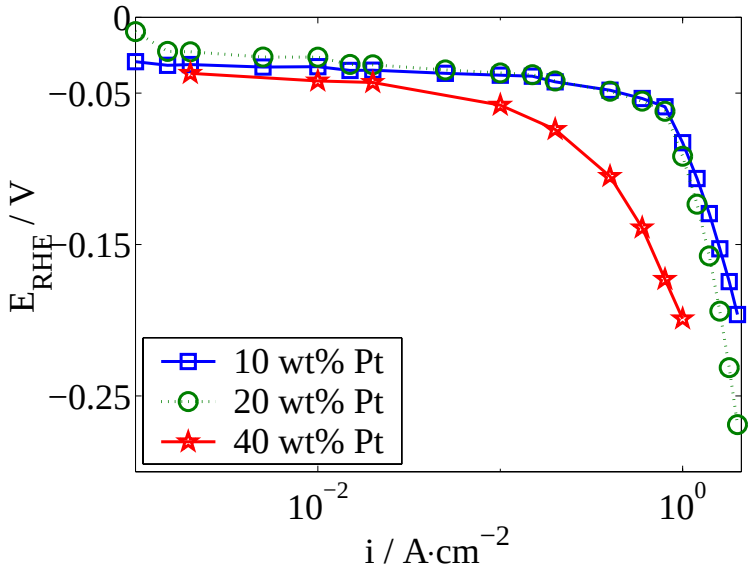

Figure 5.44: Polarization curves of different Pt on Vulcan XC-72 catalysts as a function of wt% Pt.

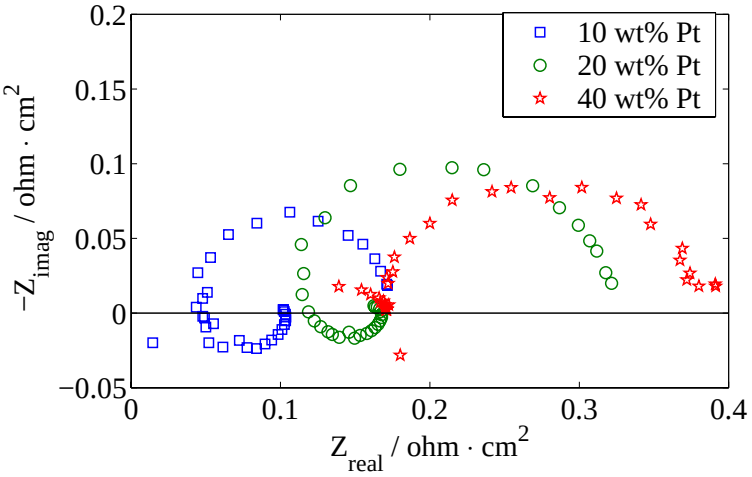

Figure 5.45: Impedance of different Pt on Vulcan XC-72 catalysts as a function of wt% Pt.

These results shows that the 10 wt% Pt on Vulcan XC-72 exhibits the best performance of the three catalysts compared and that the most important difference probably can be addressed to the structural properties of the catalytic layers.

5.5.2 RuO_2 as catalysts towards the HER

RuO_2 have been proposed as catalyst towards the HER due to high activity, stability performance and unsensitivity towards UPD and poisoning of metal cations [138]. The oxide of Ru is also known to become more active after H_2 evolution due to improved wetting of the pores and increased surface area [139].

One sample was prepared and tested as cathode in SPE® electrolysis. The sample was pyrolysed 30 minutes and annealed 1 hour at 350 °C. Figure 5.46 shows the polarization curve of a RuO_2 catalysts using a total loading of 2 $mg \cdot cm^{-2}$. Voltammetry, impedance and polarization curves were measured before and after electrode activation by extensive H_2 evolution at 1 $A \cdot cm^{-2}$ for 24 hours at room temperature.

The polarization curves before and after activation can be seen in figure 5.46. It can be seen that the negative overpotential has slightly decreased after H_2 evolution, however, the difference is almost insignificant. At 1 $A \cdot cm^{-2}$ the potential is about -0.32 V_{RHE}, which is more than 200 mV in overpotential compared to the 10 wt% Pt on Vulcan XC-72 catalyst at approximately 5 times the Pt loading.

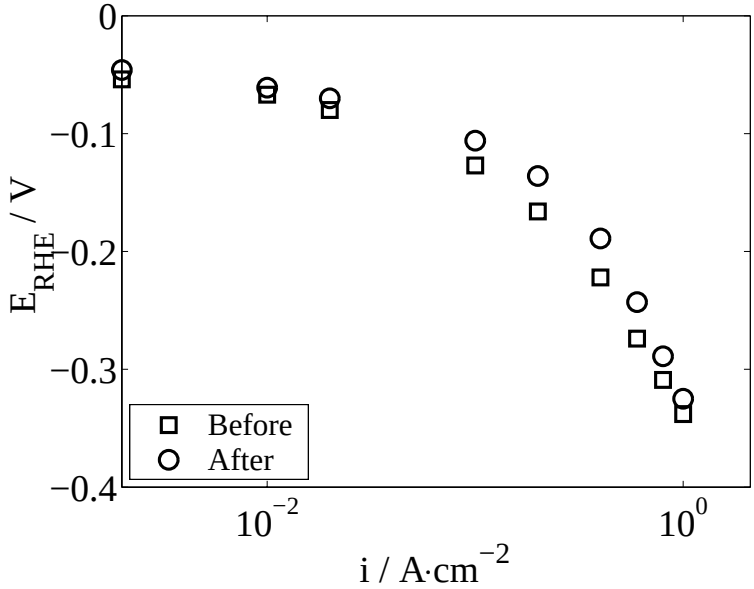

Figure 5.46: Cathodic polarization of a RuO_2 electrode.

The voltammograms, measured before and after extensive H_2 evolution, are shown in figure 5.47 and resemble that of a typical RuO_2 voltammogram shown in figure 2.12. The voltammetric area have increased after activation, which is in accordance with the literature [139, 140].

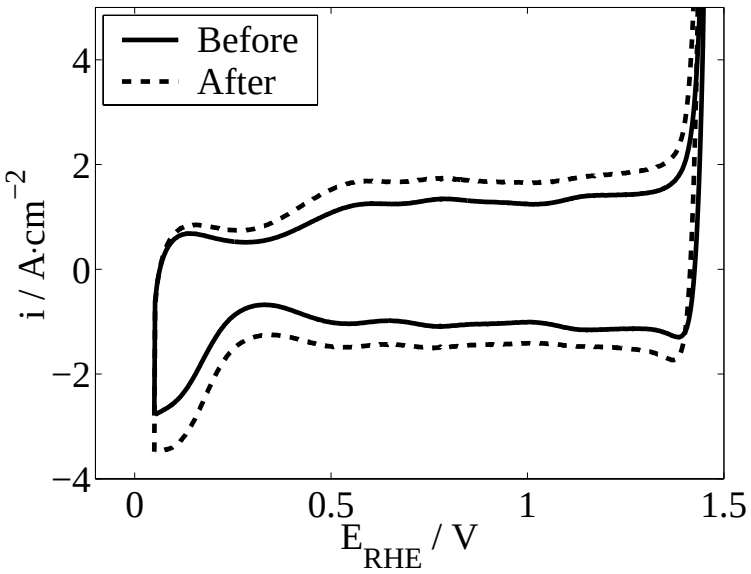

Figure 5.47: Voltammogram of a RuO_2 electrode in the SPE cell. Measured at 20 mV $\cdot$ dec^{-1} and room temperature.

The Nyquist plots are shown in figure 5.48. The high frequency region was distorted by inductance and R_Ω can only be estimated approximately. As can be observed, the semicircle shifts towards lower values along the real axis, which corresponds to a decrease in R_Ω.

The Tafel slopes at high and low η after correction of ohmic drop are given in table 5.16 together with R_Ω from impedance. A Tafel slope of -40 mV $\cdot$ dec^{-1} was found for the sample measured before extensive H_2 evolution. Due to few number of points in these measurement the slopes are difficult to determine accurately. However, the value indicate a Tafel-Heyrovsky mechanism where the Heyrovsky-step is the rds, see table 2.3 in section 2.4.1. The Tafel slope corresponds well with the value found in most literature on RuO_2 and IrO_2 electrodes [91, 141, 140]. Kötz *et* al. [138] studied RuO_2 as a cathode in the Membral® electrolyser and found also a Tafel slope of -40 mV $\cdot$ dec^{-1}. Kodintsev *et* al. [142] reported of a Tafel slope of -60 mV $\cdot$ dec^{-1} of pure RuO_2 electrode and attributed this to a surface rearrangement step of the electrochemical adsorbed hydrogen species after the primary discharge step.

It can be seen that only an apparent activation is obtained after H_2 evolution on the RuO_2 catalyst. In addition to an increase in number of active sites, increased

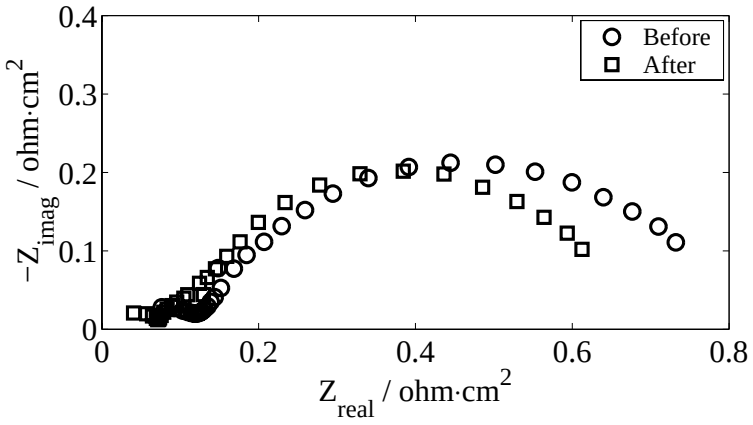

Figure 5.48: Nyquist plot of a RuO_2 electrode at cathodic polarization. Measured at 20 $mA \cdot cm^{-2}$ and room temperature.

Table 5.16: Cathodic Tafel slopes on RuO_2 catalyst before and after H_2 evolution.

Sample	b_c low η ($mV \cdot dec^{-1}$)	b_c high η ($mV \cdot dec^{-1}$)	R_Ω ($\Omega \cdot cm^2$)
Before	-40	-120	0.13
After	-50	-140	0.08

Tafel slopes suggest a change to less favourable kinetics. Reduced R_Ω is not easy to understand, however, sintering of the catalytic layer due to mechanical interaction with the gas bubbles can be possible explanation.

Tests reported in the literature are typically performed in half cell experiments at low cd, up to 100 $mA \cdot cm^{-2}$ or so on a continuous underlaying substrate. Thus, the most important limitations at high cd are not observed. The difference in overpotential between the RuO_2 and the 10 wt% Pt on Vulcan XC-72 at 1 $A \cdot cm^{-2}$ is about 200 mV and constitutes almost 0.48 kWh per Nm^3 H_2 produced, which leads to a considerably increase in production costs for large scale H_2 production. The loading of the RuO_2 catalyst was also about 5 times higher than the Pt loading and, thus, the electrode cost of the two catalysts becomes approximately the same. Unless other type of membranes are developed, which are non-sensitive to poisoning, RuO_2 has little interest in SPE® electrolysis.

5.5.3 Pt-black as cathode catalyst

In SPE® water electrolysis unsupported Pt is most commonly used as cathode catalyst, either by chemical precipitation [76, 114] into the membrane or by hot-pressing the catalytic layers of Pt-black onto the membrane [77, 78, 143]. Reports on using Pt supported catalyst in SPE® water electrolysis in the literature is scarce. In this work, the Pt supported catalysts have been chosen mainly to obtain lower Pt loadings, as analogue to fuel cells [3], and because many different catalysts are already available at the commercial market.

Preparation of catalytic layers of Pt-black by the spraying technique was found to be very difficult in this work. Even though the Pt particles are of the same particle size as the oxide particles prepared by Adams method, the Pt particles quickly formed large agglomerates and segregated during the spraying stage and were also deposited onto the wall of the airgun-cup. Metallic Pt possess different surface properties compared to oxide particles and interact differently with the ink solvent, where adsorption of solvents and Nafion® ionomer at the particle surface takes place. However, one Pt-black electrode was prepared for comparison. The preparation of this electrode was very troublesome and the catalyst loading was not possible to control accurately, however, the loading was somewhere in the range of 2 - 2.5 mg $\cdot$ cm^{-2}. The Pt-black catalyst has been compared to the 10 wt% Pt on Vulcan XC-72 at 0.4 mg Pt $\cdot cm^{-2}$.

Voltammograms of the Pt-black electrode and the 10 wt% Pt on Vulcan XC-72 catalyst are shown in figure 5.49. The Pt-black voltammogram resemble more a typical Pt voltammogram obtained in acidic solutions as shown in figure 2.7, except that the H-peaks are somewhat asymmetric about the x-axis and that the oxygen adsorption have taken place at lower anodic potentials and oxygen reduction peak at higher anodic potentials. This discreapancy is probably related to the Nafion® environment and different acidity. Much more well defined H-peaks are obtained by the Pt-black catalyst compared to the Pt supported catalyst.

Figure 5.51 shows the polarization curve of the Pt-black and 10 wt% Pt samples. As can be seen, the Pt-black catalyst shows superior performance at high cd compared to the 10 wt% Pt catalyst, where the Pt-black electrode possess 100 mV less overvoltage at 2 A $\cdot$ cm^{-2}. The Nyquist plots are shown in figure 5.51 and R_Ω was found to be 0.04 and 0.10 $\Omega \cdot cm^2$ for Pt-black and 10 wt% Pt on Vulcan XC-72 respectively. This shows how important the ohmic resistance of the catalytic layers becomes, also emphasized in section 5.2.

The potential at low cd is higher of the 10 wt% Pt on Vulcan XC-72 catalyst, which correspond to a higher i_0 and a higher apparent catalytic activity. The Pt loading is 5 times higher for the Pt black catalyst than the Pt supported catalyst, which indicates that a higher dispersion of the active sites at the interface between the membrane and the catalytic layer has been obtained with the Pt supported catalyst compared to Pt-black.

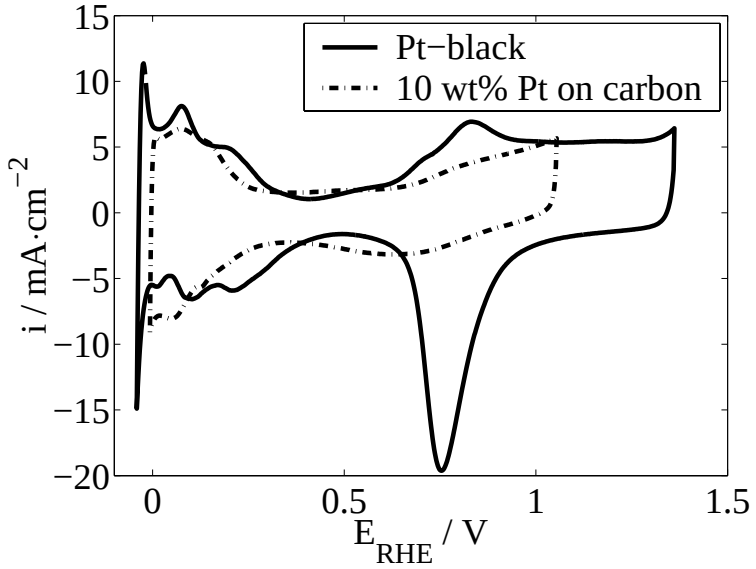

Figure 5.49: Pt-black and 10 wt% Pt on Vulcan XC-72 catalysts. Measured at 20 mV $\cdot$ s^{-1}
at room temperature.

It is not only the conductivity of the material that determine the electrical conductivity of the catalytic layer. The carbon particles are of 0.5 μm in particles size, whereas the Pt-black and the metal oxide particles are in the range from 10 to 100 nm. A much closer packing of the catalytic layer will be obtained in the case of smaller particles and result in higher electrical conductivity. The carbon particles provide a porosity of 35 - 65 % in the catalytic layers of SPE® fuel cells and increased porosity have been observed to increase the ohmic resistance [137]. It is not clear whether the increased R_Ω of the Pt supported catalyst is due to lower electrical conductivity of the material itself or to increased porosity, probably both effects must be taken into account. In fuel cells however, the disadvantage of higher ohmic resistance by increasing the porosity is compensated by better access to the active sites of the reacting gases and less diffusion limitations (this depends on the pore size and pore size distribution as well). Probably, a considerable performance enhancement of Pt supported catalysts can be obtained by reducing the particle size of the support and/or by using support of higher electrical conductivity.

Figure 5.52 shows the potential dependence by time after stepping the current to 0.2 A $\cdot$ cm^{-2} of the Pt-black and the Pt supported catalysts. As can be seen the negative overvoltage of the Pt supported catalyst decreases by time, whereas the Pt-black catalyst first increases and then reaches a constant and somewhat oscillating potential.

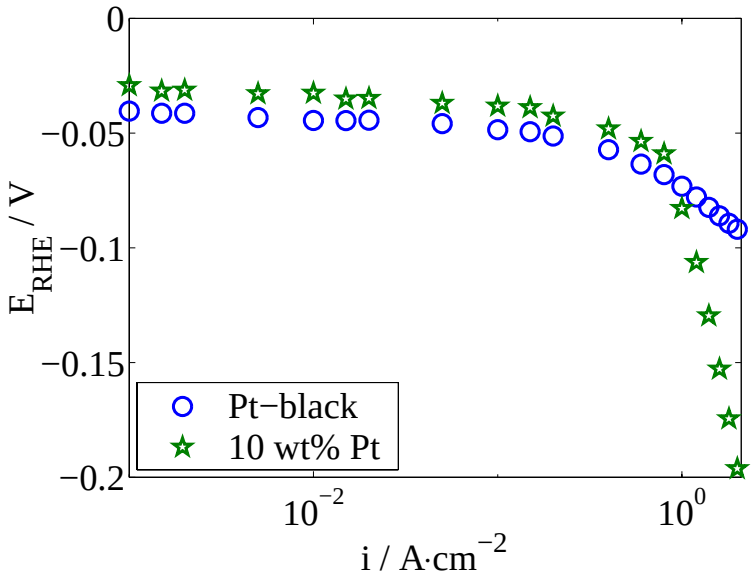

Figure 5.50: Polarization curves of Pt-black and 10 wt% Pt on Vulcan XC-72 catalysts.

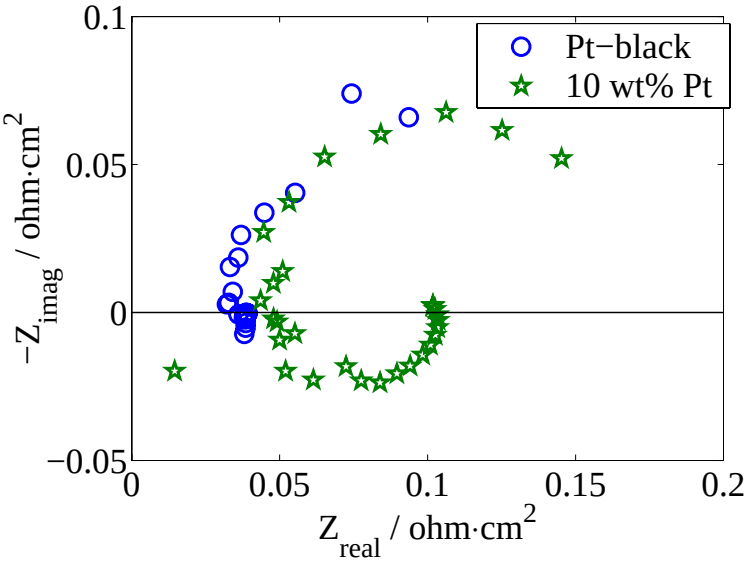

Figure 5.51: Polarization curves of Pt-black and 10 wt% Pt on Vulcan XC-72 catalysts.

This can probably be related to increased ionic conductivity and access to more active sites by increased wetting of the strongly hydrophobic Pt supported catalytic layer as mentioned above. This type of behaviour was found for all the Pt supported catalysts.

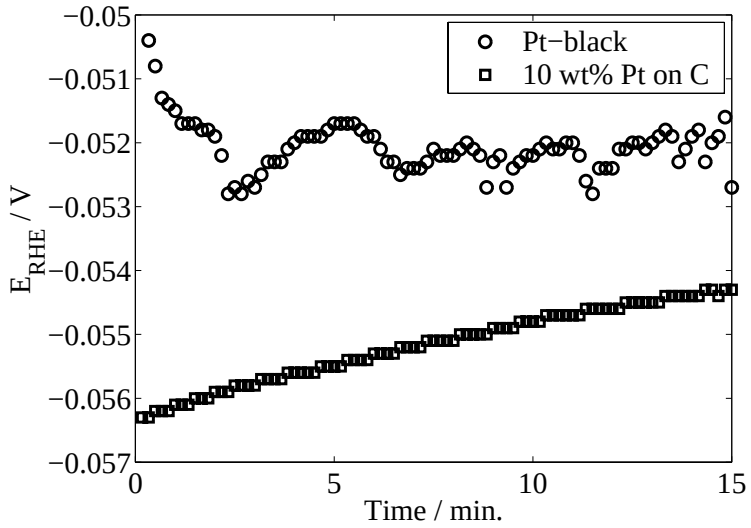

Figure 5.52: Potential-time curves of Pt-black and 10 wt% Pt on Vulcan XC-72 electrodes. Current stepped to 0.2 A · cm^{-2}.

It can be seen from the Nyquist plots in figure 5.51 that only the 10 wt% Pt catalyst possess the high frequency loop. The pseudo inductive loop at high frequency of the Pt supported catalyst is always measured on 10 and 20 wt% Pt on Vulcan XC-72 catalysts, never on the 40 wt% Pt on Vulcan XC-72, Pt-black or RuO_2 or any other materials. This inductive behaviour have been confirmed by about 300 electrodes where the 10 and 20 wt% constitute about 60 - 70 % of the samples. Figure 5.53 and 5.54 shows the Nyquist and Bode plot respectively of the 10 wt% Pt on Vulcan XC-72 catalyst measured from 25 to 40 mV negative overpotentials. It can be seen than the semi circle increases for increasing negative potentials. The response of this time constant is measured at frequencies from 10 to 100 Hz and indicate a process related to the electrochemical response and the diameter of the loop increases for increasing polarization of the electrode. Grzeszczuk *et* al. [144] measured a similar pseudo inductive loop for the HER on nanoparticles of Pt incorporated into a polyaniline film on a polished glassy carbon disk measured in HCl aqueous solution. This type of inductive behaviour has usually been addressed to phenomena as intrinsic capacitances of the reference electrode, interfacial relaxation and adsorption phenomena [145].

To check the consistency of the measurements, a material with well known impedance behaviour can be used for comparison. An electrode of 10 wt% Pd on Vulcan XC-

72 was prepared according to standard procedure at 0.4 Pd $mg \cdot cm^{-2}$ and the impedance behaviour can be seen in figure 5.55 together with the impedance of 10 and 20 wt% Pt on Vulcan XC-72. The two time constants on the Pd catalyst can easily be recognised for HER at metals with hydrogen storage capacity [146], where the time constant at high frequency can be attributed to adsorption and diffusion of hydrogen into the porous structure of Pd and the second time constant at low frequency can be attributed to the HER. The straight line at high frequency was very close to 45°. This further confirms that the impedance measured *in situ* in the SPE® cell is a response of the electrode process. From figure 5.55 the inductive loop is smaller for 20 wt% than on 10 wt% Pt.

It is striking to observe that this inductive loop is only present for very small Pt particles on 10 and 20 wt% Pt on Vulcan XC-72. The fact that the diameter of the loop is larger for 10 wt% Pt than for 20 wt% Pt and that the diameter increases for increasing potentials, suggest that this loop increases for increasing H_2 fugacity. The loop can probably be related to supersaturation and transport away from the Pt surface and, thus, can be used as an indication of a very active electrode.

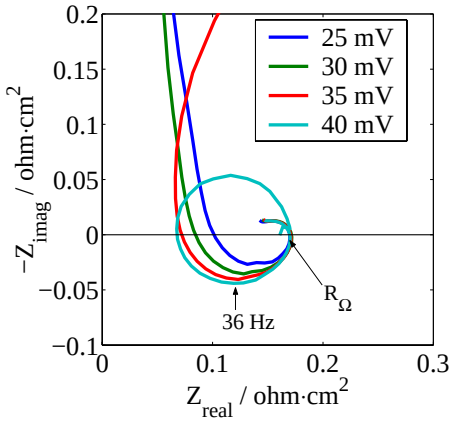

Figure 5.53: Nyquist plot at increasing potentials of 10 wt% Pt on Vulcan XC-72.

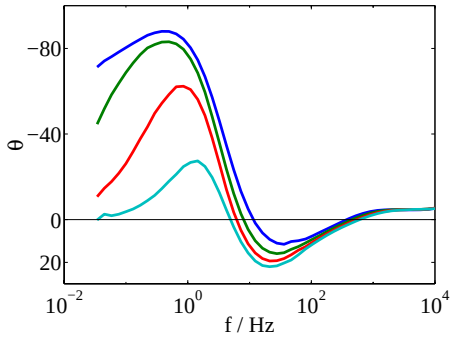

Figure 5.54: Bode plot at increasing potentials of 10 wt% Pt on Vulcan XC-72.

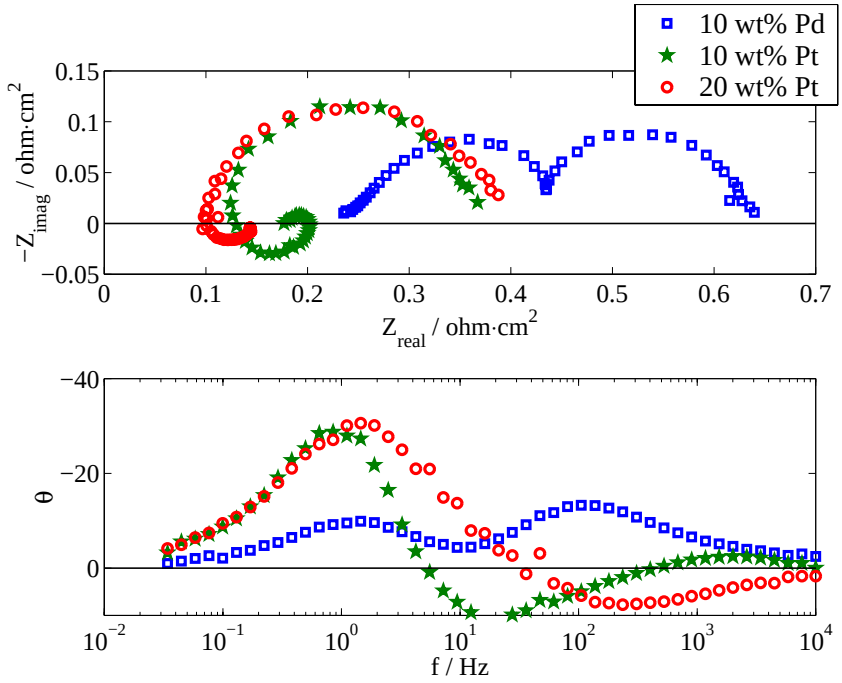

Figure 5.55: Nyquist and Bode plot of 10 wt% Pd, 10 wt% Pt and 20 wt% Pt on Vulcan XC-72 support. Measured at constant cd of 20 $mA \cdot cm^{-2}$ and room temperature.

5.5.4 Summary

Optimum catalyst performance of the 20 wt% Pt on Vulcan XC-72 catalyst was obtained by using approximately 25 wt% Nafion® ionomer and a Pt loading of about 0.3 mg $\cdot cm^{-2}$. Increasing catalyst performance was obtained for lower wt% Pt on the carbon support, attributed to the smaller particle size.

By using Pt supported catalyst, a very high activity and dispersion of the active catalyst can be obtained by the spraying technique. However, the high porosity provided by the large carbon particles also results in a high ohmic resistance within the catalytic layer, which seriously limits the performance/voltage efficiency for high current density. The Pt-black catalyst possessed a much lower ohmic resistance and possessed 100 mV less in negative overvoltage at 2 $A \cdot cm^{-2}$ and room temperature compared to the best Pt supported catalyst. Still, a higher electrocatalytic activity of the Pt supported catalyst was obtained and suggests that a support material of lower particle size and better electrical conductivity should be found. High hydrophobicity of the Pt supported catalysts may result in difficult release of gas bubbles from the electrode.

A pseudo-inductive loop from 10 to 100 Hz found on the 10 and 20 wt% Pt on Vulcan XC-72 catalysts, can probably be attributed to the high activity of the electrodes. The can probably be attributed to supersaturation of H_2 and transport away from the electrode surface. However, more study is necessary to determine the origin and behaviour of this time constant.

RuO_2 as cathode catalyst in SPE® electrolysers was found to be of little interest and its performance became very limited for high current density. However, if membranes of less sensitivity towards metal cation poisoning are developed, RuO_2 as a cathode catalyst may be justified.

5.6 Performance summary

This section shows what performance than can be expected of a SPE electrolyser based on the results shown in previous chapters.

The main emphasis in this work has been to understand the properties of the electrodes and catalysts that limit the electrode performance by the use of a reference electrode to measure the anode and cathode characteristics. The measurements has more conveniently been carried out at room temperature and anode and cathode catalysts has randomly been connected to each other. Only a very few polarization curves were obtained at higher temperatures and figure 5.56 shows a quasi steady state polarization curve obtained at 80 °C using 10 wt% Pt on Vulcan XC-72/Nafion® -115/IrO_2 composite of noble metal loading less than 2.4 $mg \cdot cm^{-2}$. This was obtained using the Kurchatov-cell (see section 4), where the temperature was much easier to control for different cds. However, this cell never showed performance as good as the NTNU-cells and it was believed that this cell design limited the performance of the MEAs. U_{cell} was measured to be 1.645 and 1.811V at 1 and 2 $A \cdot cm^{-2}$ respectively. This still represent a relative good performance compared to the literature as described in section 3. These results are obtained using thermally prepared IrO_2 based electrodes, which is considered to be somewhat less active, however, far more stable compared to metallic Ir, which is frequently used as anode catalyst in SPE® electrolysis.

The NTNU-cells were used for electrochemical characterization at room temperature. Independent optimization of anode and cathode resulted in a random cell performance from time to time and the total cellvoltage of the different MEAs have not been focused on during this optimization. However, in a few occasions, where a relatively good overall cell performance was obtained, the feed water was heated to higher temperatures to evaluate the performance at typical operating conditions, which will be of primary interest from a more industrial point of view. The cellvoltage measured at 1 $A \cdot cm^{-2}$ and 80-90 °C represent a typical regime for continuous hydrogen production of the SPE® electrolyser and is throughout in the literature used for comparison of the energy efficiency of electrolysers.

The anode and cathode potentials to some of the most interesting MEAs in this work, measured versus RHE at room temperature and 1 $A \cdot cm^{-2}$, are shown in table 5.6 together with the U_{cell}. The different catalysts and loadings of active catalyst[3] of the MEAs are given in table 5.18. The anode catalyst of MEA #1, #2 and #3 are described in section 5.3, 5.4 and 5.2 respectively, and represents the catalyst with best performance from each series. The Pt-black catalyst of MEA #4 was described in section 5.5. The anode catalyst of MEA #4 is the same as the pure IrO_2-catalyst described in section 5.4. However, this anode catalyst was not expected to show any good performance due to a strongly oxidized Ti-sinter

[3]Active catalyst loading here refers to mg IrO_2, IrO_2+RuO_2 or Pt per cm^2

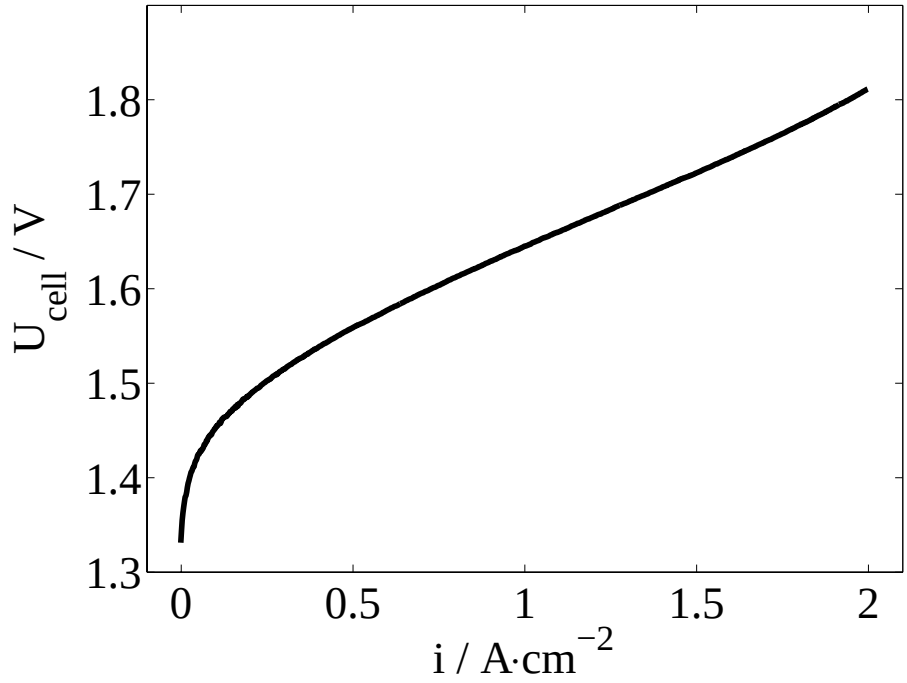

Figure 5.56: Quasi steady state polarization curve at 80 °C of a 10 wt% Pt on Vulcan XC-72/Nafion-115/IrO_2 composite using noble metal loading of less than 2.4 mg $\cdot$ cm^{-2}.

at the anode side, which had previously been used in a series of high temperature measurements. Only the characteristics of the Pt-black catalyst is of primary interest of MEA #4.

Table 5.17: Anode and cathode potentials, measured versus the reference electrode, and cell potentials at 1 A $\cdot$ cm^{-2} and room temperature.

# MEA	E_{anode} (V_{RHE})	$E_{cathode}$ (V_{RHE})	U_{cell} (V)
1	1.64	-0.14	1.78
2	1.65	-0.19	1.84
3	1.68	-0.28	1.92
4	1.78	-0.07	1.85

MEA #1 shows a U_{cell} of 1.78 V at 1 A $\cdot$ cm^{-2} and room temperature. This is close to the performance obtained in the literature (see section 3), where U_{cell} ranges from 1.68 - 1.75 V measured at 80 - 90 °C[69, 73, 77, 78, 81, 83]. From

Table 5.18: Catalyst type and loading of active catalyst.

	Anode catalyst		Cathode catalyst	
#MEA	Catalyst type	Loading ($mg \cdot cm^{-2}$)	Catalyst type	Loading ($mg \cdot cm^{-2}$)
1	0.85Ir-0.15Ta oxide	2	10 wt% Pt on C	0.4
2	0.7Ir-0.3Ru oxide	2	20 wt% Pt on C	0.4
3	IrO_2	2	RuO_2	2
4	IrO_2	2	Pt-black	2-2.5

table 2.5 in section 2.7 it can be seen that the ohmic resistance of the Nafion® -115 membrane is approximately 0.17 $\Omega \cdot cm^2$, which represents 170 mV of the total cellvoltage at 1 $A \cdot cm^{-2}$. By using a thinner membrane, e.g. Gore-Select™, the ohmic contribution from the membrane constitute only 30 mV at 1 $A \cdot cm^{-2}$ and room temperature. Thus, for MEA #1 a cellvoltage of 1.78 - 0.17 + 0.03 = 1.64 V at room temperature can be possible using the same type of catalysts and a Gore-Select™ membrane. Assuming that the reference point measured with the reference electrode is in the middle between anode and cathode, as described in section 4, the anode and cathode potential can be added together to give the cellvoltage. i.e. $U_{cell} = E_{anode} + |E_{cathode}|$. Adding together E_{anode} of MEA #1 and $|E_{cathode}|$ of MEA #4 results in $U_{cell} = 1.64 + 0.07 = 1.71$ V at room temperature. It must be noted that these values represents the best obtained catalytic layers and that the the reproducibility of the electrodes typically is ±50 mV.

The feed water of MEA #2 was heated to maximum and the temperature was measured inside the cell together with the U_{cell} at constant current density of 1 $A \cdot cm^{-2}$. The cellvoltage as a function of temperature is shown in figure 5.57. A cellvoltage of 1.59 V was obtained at 90 °C of this MEA. The data were fitted to a polynomial given by equation 5.3 and the fitted curve is shown as continuous line in figure 5.57. The constants in equation 5.3 are given in table 5.19.

$$U_{cell}(T°C) = U_{cell}(25°C) + a_1 + a_2 \cdot T + a_3 \cdot T^2 \tag{5.3}$$

Table 5.19: Parameters in equation 5.3.

a_1	0.127
a_2	$5.4 \cdot 10^{-4}$
a_3	$1.5 \cdot 10^{-5}$

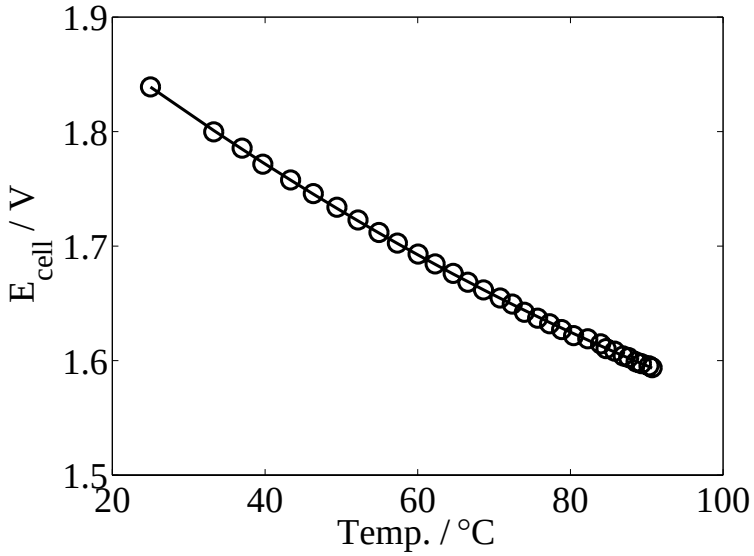

Figure 5.57: U_{cell} versus temperature at constant current of 1 $A \cdot cm^{-2}$.

The cellvoltage is a complex function of the temperature, which influences important parameters as the thermodynamic potential, electrode kinetics, ionic conductivity of the membrane and release of gas bubbles. Assuming that the cellvoltage-temperature behaviour is approximately the same for the different MEAs, equation 5.3 can be used to predict the cell voltage at 1 $A \cdot cm^{-2}$ and higher temperatures. In section 5.1 the cellvoltage-current density behaviour was studied as a function of the temperature, shown in figure 5.10, and U_{cell} was found to be 2.005 V at 25 °C. Entering 2.005 V and 75 °C into equation 5.3 returns a value of 1.762 V, which is in fairly good agreement with the measured value of 1.761 V at 1 $A \cdot cm^{-2}$ and 75 °C of this MEA. Following the same procedure of MEA #1 and substituting U_{cell} = 1.78 V and T = 90 °C into equation 5.3 results in a U_{cell} value of 1.51 V using a noble metal loading of less than 2.4 $mg \cdot cm^{-2}$ and Nafion® -115 membrane. Taking into account that better cathode performance has been obtained, U_{cell} less than 1.5 V at 1 $A \cdot cm^{-2}$ and 90 °C seem possible. This shows promising results when compared with the 1.53 V obtained within the WE-NET program [79] where 3.5 mg noble metals per cm^2 was used at the electrodes using 51 μm thick membrane and gold and Pt plated current collectors. However, it must be taken into account that the japanese group obtained their results using 50 cm^2 active surface area.

Predicting U_{cell} using equation 5.3 may be misleading since different behaviour of different catalysts not are taken into account. However, it seem to be possible to get close to thermoneutral potential of 1.48 V (see section 2) at practical operating conditions of a SPE® electrolyser. This corresponds to an energy consumption of

3.54 kWh $\cdot$ Nm^{-3} at 10 kA $\cdot$ m^{-2}, or approximately 4.1 Nm^{-3} H_2 per hour from one electrode of 1 m^2 in active area, if only considering the voltage efficiency. The current efficiency of SPE® electrolysers is about 98-99 % [77].

The anode catalyst of MEA # 1 showed a very steep potential increase for current density of more than 0.75 A $\cdot$ cm^{-2}, whereas the anode catalyst of MEA #2 on the other hand showed a much better performance above 1 A $\cdot$ cm^{-2}. Figure 5.58 shows the anodic polarization curve of MEA #2 added together with the cathodic polarization curve of MEA #4 measured at room temperature. The resulting polarization curve exhibit a cell potential of 1.719 and 1.815 V at 1 and 2 A $\cdot$ cm^{-2} respectively. In section 5.1 it was shown that the cellpotential at 2 A$\cdot$cm^{-2} decreased by 336 mV when increasing the temperature from 25 to 75 °C. Assuming a reduction in U_{cell} of more than 300 mV can be obtained when heating from 25 to 90 °C, U_{cell} down to 1.5 V should be possible to obtain at 2 A $\cdot$ cm^{-2} and 90 °C using $Ir_{0.7}Ru_{0.3}O_2$ anode catalyst and Pt-black cathode catalyst and a Nafion® -115 membrane and a noble metal loading of approximately 4 - 4.5 mg $\cdot$ cm^{-2}.

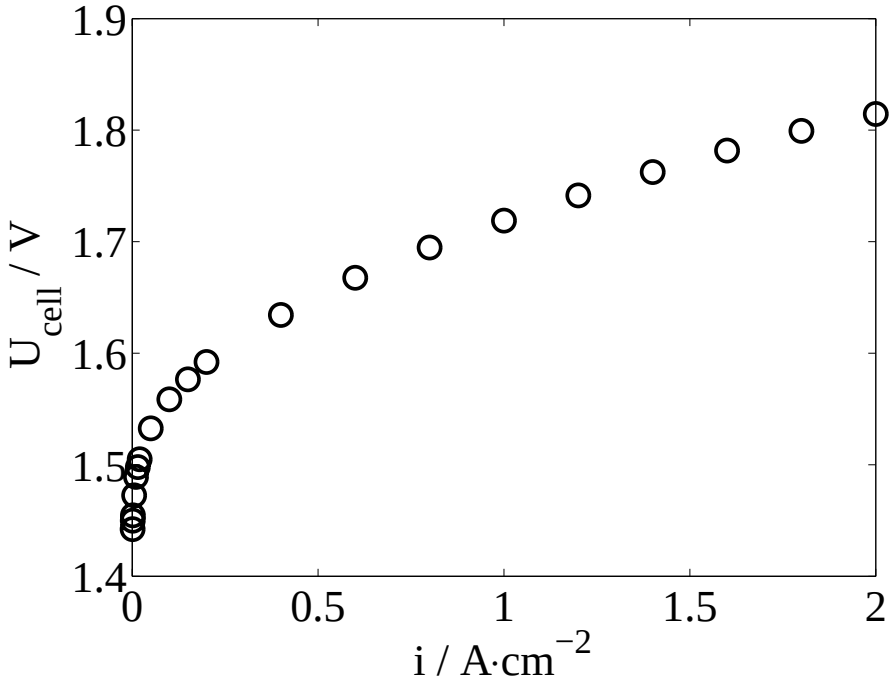

Figure 5.58: A predicted polarization curve when adding together the anode and cathode potentials from two different MEAs found to exhibit the best performance in this work.

These predicted results suggests than even higher energy efficiency can be obtained than what is reported in the in the literature so far, however, it remains to be

measured at the laboratory. The best results actually measured in this work at 1 $A \cdot cm^{-2}$ and 90 °C was U_{cell} = 1.59 V by MEA #2, as shown in figure 5.57. It can be noted that the cathode of MEA #2 was not of any particular good performance. Assuming a current efficiency of 99 %, Gibbs energy efficiency of MEA # 2 corresponds to $\varepsilon_{\Delta G} = (1.17/1.59) \cdot 100 \cdot 0.99 = 73$ % and the thermal energy efficiency corresponds to $\varepsilon_{\Delta H} = (1.48/1.59) \cdot 100 \cdot 0.99 = 92$ %.

Chapter 6

Conclusions

Catalysts for electrodes in water electrolysis system using a polymer membrane as electrolyte, have been carried out and cell voltage of 1.59 V ($\varepsilon_{\Delta G} = 73$ %) has been obtained at practical operation conditions of the electrolyser at 10 $kA \cdot m^{-2}$ and 90 °C using a noble metal loading of less than 2.4 $mg \cdot cm^{-2}$. A cell voltage less than 1.5 V is possible at the same conditions by combination of the best anode and the best cathode obtained in this work.

The results have been obtained by the following steps:

- Lab cells with 5 cm^2 active area have been designed and constructed with minimum IR-drop and without transport limitations of water or gases. *In situ* electrochemical measurements in the lab cells have made it possible to reveal important limitations of the catalysts and to evaluate the electrode preparation technique.
- An electrode preparation technique by direct deposition onto the membrane have been developed. The technique has been shown to be:
  - satisfactory for metal oxide catalyst
  - less satisfactory for Pt supported catalysts or metallic Pt.
- Preparation and characterization of different catalysts have been performed.

Different anode catalysts have been produced and characterized based on thermally prepared oxides of iridium and important factors and limitations of these catalysts have been determined. It was found that the electrical conductivity is of the outmost importance due to the porous backing/current collector system, which provide longer pathways and a more narrow cross-section for electron transport than what is apparently observed. A compromise between electrical conductivity

and density of active sites must be found by tailoring the preparation and thermal annealing condition of the metal oxide catalysts.

Mixed oxides of Ir-Ta and of Ir-Ru have been studied as anode catalyst. Additions of small amounts of Ta to Ir resulted in suppressed crystallite growth, decreased crystallinity and led possibly also to a withdrawal of electrons from the Ir cation. This resulted in a very low Tafel slope at current densities below 1 $A \cdot cm^{-2}$ and high voltage efficiency. Better performance at high current densities can be expected for this catalyst composition if the oxide is annealed at higher temperature. For current densities up to 2 $A \cdot cm^{-2}$ a higher Ta content may be favourable due to expected longer life time. More studies on this catalyst composition for higher Ta content is recommended in the future.

The mixed oxide of Ir-Ru showed very good performance at current densities above 1 $A \cdot cm^{-2}$ at 60-80 mole% of Ir. However, the surface of the oxide was found to be enriched by the Ru component, which may be unfortunate with respect to life time performance. The enrichment process was believed to be caused by stronger affinity towards oxygen of the Ru specie where the long annealing time allowed sufficient time for diffusion to the surface. Further studies on this catalyst composition using shorter annealing time is recommended.

In general, when working with metal oxide catalysts, the electrochemical behaviour is determined by the physico-chemical state of the oxide. It is therefore the outmost importance to understand the correlation between electrochemical properties and the crystal structure of the metal oxides and X-ray techniques must be applied to gain further knowledge of the preparation process of these catalysts. A multi-disciplinary approach is necessary for further progress in the future.

It was found that commercial available fuel cell catalysts of Pt on Vulcan XC-72 not showed favourable properties as cathode catalyst at typical operation conditions of a SPE® electrolyser. The relatively low performance of these catalysts at higher current densities may be caused by one or more of the following matters:

- High porosity provided by the catalyst and thereby introduced higher ohmic drop.
- A relatively low electrical conductivity of the carbon particles.
- Difficult release of evolved gas from the very hydrophobic catalyst.

Pt-black served as a much better hydrogen catalyst at higher current densities, possibly caused by a more densely packed catalytic layer and a higher electrical conductivity. For low current density the Pt supported catalyst was apparently more active than the Pt-black catalyst, probably due to a much higher dispersion of Pt on the carbon support. Possibly, a better performance of the Pt supported

catalyst can be obtained by using smaller particles of the support and/or support particles of higher electrical conductivity.

RuO_2 was not found to show any promising performance as cathode catalyst at typical operation conditions of a SPE® electrolyser due to much lower electrocatalytic activity and lower electrical conductivity compared to the Pt catalysts. RuO_2 may be of interest to replace the more expensive Pt catalyst only when there is danger of poisoning the membrane by metal cations, however, purification of the feed water will in any case be necessary to avoid contamination of the sulphonic groups of the membrane and thereby loss of ionic conductivity. In any case, removal of cations, which contaminate both membrane and cathode catalyst, seem to be possible by intermittent flushing with diluted HCl.

Bibliography

[1] C.-J. Winter. Hytime-it's high time for hydorgen energy business fourm. *Int. J. Hydrogen Energy*, 22:847, 1997.

[2] D. G. Kessel. Global warming-facts, assessment, countermeasures. *J. Petroleum Sci. and Engeneering*, 26:157, 2000.

[3] G. Sasi Kumar, M. Raja, and S. Parthasarathy. High performance electrodes with very low platinum loading for polymer electrolyte fuel cells. *Electrochim. Acta*, 40:285, 1995.

[4] R. de Levie. The electrolysis of water. *J. Electroanal. Chem.*, 476:92, 1999.

[5] J. A. A. Ketelaar. *Fuel cell systems*. Plenum Press, New York, 1993.

[6] W. Kreuter and H. Hofmann. Electrolysis: the important energy transformer in a world of sustainable energy. In T. N. Verziroğlu, C. J. Winter, J. P. Baselt, and G. Kreysa, editors, *Hydrogen Energy progress XI*, volume 1, page 537, 1996.

[7] M. Rikukawa and K. Sanui. Proton-conducting polymer electrolyte membranes based on hydrocarbon polymers. *Prog. Polym. Sci.*, 25:1463, 2000.

[8] T. N. Verziroğlu. Twenty years of the hydrogen movement. *Int. J. Hydrogen Energy*, 20:1, 1995.

[9] P. Kruger. Electric power requirement in California for large-scale production of hydrogen fuel. *J. Hydrogen Energy*, 25:395, 2000.

[10] B. Gaudernack. Hydrogen production from fossil fuels. In T. O Saetre, editor, *Hydrogen power: Theoretical and engineering solutions*, volume 1, page 75, Netherlands, 1997. Hypothesis II, Kluwer Academic Publishers.

[11] H. Wendt and V. Plzak. Electrocatalysis and electrocatalysts for cathodic evolution and anodic oxidation of hydrogen. In H. Wendt, editor, *Electrochemical hydrogen technologies*, page 15. Elsevier, 1990.

[12] *JANAF Thermochemical Tables*. U.S Department of Commerce, NSRDS, second edition, 1971.

[13] S. Trasatti. Electrode kinetics and electrocatalysis of hydrogen and oxygen electrode reactions. In H. Wendt, editor, *Electrochemical hydrogen technologies*, page 1. Elsevier, Amsterdam, 1990.

[14] I. Barin. Thermochemical data of pure substances. VCH, New York, 3 edition, 1995.

[15] S. Trasatti, editor. *Electrodes of conductive metallic oxides. Part B.* Elsevier Scientific, 1980.

[16] A. J. Bard and L. R. Faulkner, editors. *Electrochemical methods.* Wiley, New York, 1980.

[17] B. E. Conway. *Electrochemical supercapacitors.* Kluwer Academic, New York, USA, 1999.

[18] B. E. Conway W. G. Pell. Voltammetry at a de levie brush electrode as a model for electrochemical supercapacitor behaviour. *J. Electroanal. Chem.*, 500, 2001.

[19] J. R. Macdonald, editor. *Impedance spectroscopy.* Wiley, New York, 1987.

[20] R. De Levie. On porous electrodes in electrolyte solutions-IV. *Electrochim. Acta*, 9:1231, 1964.

[21] D. D. Macdonald. *Characterization of electrodes and electrochemical processes.* Wiley, NewYork, 1991.

[22] S. Trasatti. Work function, electronegativity, and electrochemical behaviour of metals. *J. Electroanal. Chem.*, 39:163, 1972.

[23] B. E. Conway and G. Jerkiewicz. Relation of energies and coverages of underpotential and overpotential deposited H at Pt and other metals to the 'vulcano curve' for cathodic H_2 evolution kinetics. *Electrochim. Acta*, 45, 2000.

[24] L. D. Burke. Oxide growth and oxygen evolution on noble metals. In S. Trasatti, editor, *Electrodes of conductive metallic oxides. Part A*, page 141. Elsevier Scientific, Amsterdam, 1980.

[25] S. Morin J. Barber and B.E. Conway. Specificiy of the kinetics of H_2 evolution to the structure of single-crystal pt surfaces, and the relation between opd and upd H. *J. Electroanal. Chem.*, 446, 1998.

[26] G. Andreasen R. C. Saverezza M. E. Martins, C. F. Zinola and A. J. Arvia. The possible existence of subsurface H-atom adsorbates and H_2 electrochemical evolution reaction intermediates on platinum in acid solutions. *J. Electroanal. Chem.*, 445:135, 1998.

[27] H. Kita, S. Ye, A. Aramata, and N. Fruya. Adsorption of the hydrogen on platinium single crystal electrodes in acid and alkali solutions. *J. Electroanal. Chem.*, 295:317, 1990.

[28] F. Andolfatto, R. Durand, A. Michas, P. Millet, and P. Stevens. Solid polymer electrolyte water electrolysis: electrocatalysis and long-term stability. *Int. J. Hydrogen Energy*, 19:421, 1994.

[29] S.Trasatti. Electrocatalysis in the anodic evolution of oxygen and chlorine. *Electrochim. Acta*, 29, 1984.

[30] S. Trasatti. The oxygen evolution reaction. In H. Wendt, editor, *Electrochemical hydrogen technologies*, page 104. Elsevier, Amsterdam, 1990.

[31] S.Trasatti. Electrocatalysis by oxides - attempt at a unifying approach. *J. Electroanal. Chem.*, 111:125, 1980.

[32] J. O'M. Bockris. Kinetics of activation controlled consecutive electrochemical reactions: anodic evolution of oxygen. *J. Chem. Phys.*, 24:817, 1956.

[33] R. Kötz, H. Neff, and S. Stucki. Anodic iridium oxide films. *J. Electrochem. Soc.*, 131:72, 1984.

[34] J. F. C. Boodts V. A. Alves, L. A. Da Silva and S. Trasatti. Kinetics and mecahnism of oxygen evolution on IrO_2-based electrodes containing Ti and Ce acidic solutions. *Electrochim. Acta*, 39:1585, 1994.

[35] M. Vuković D. Čukman and M. Milun. Enhanced oxygen evolution on an electrodeposited ruthenium + iridium coating on titanium. *J. Electroanal. Chem.*, 389:209, 1995.

[36] I. Krasil'shchikov. *Zh. Fiz. Khim.*, 37:531, 1963.

[37] A. Dey A. Damjanovic and J. O'M. Bockris. Kinetics of oxygen evolution and dissolution on platinum electrodes. *Electrochim. Acta*, 11:791, 1966.

[38] S. Gottesfeld and S. Srinivasan. Electrochemical and optical studies of thick oxide layers on iridium and their electrocatalytic activities for the oxygen evolution reaction. *J. Electroanal. Chem.*, 86:89, 1978.

[39] D. B. Rogers, R. D. Shannon, A. W. Sleight, and J. L. Gillson. Chrystal chemistry of metal dioxides with rutile-related structures. *J. Inorg. Chem.*, 8:841, 1968.

[40] T. Arikawa, Y. Takasu, Y. Murakami, K. Asakura, and Y. Iwasawa. Characterization of the structure of RuO_2 - IrO_2/Ti electrodes by EXAFS. *J. Phus. Chem. B*, 102:3736, 1998.

[41] S.Trasatti. Physical electrochemistry of ceramic oxides. *Electrochim. Acta*, 36:225, 1991.

[42] J. M. Honig. Electronic band strucure of oxides with metallic or semiconducting characters. In S. Trasatti, editor, *Electrodes of conductive metallic oxides, part A*, page 1. Elsevier Scientific, Amsterdam, 1980.

[43] L. D. Burke and D. P. Whelan. A voltammetric investigation of the charge storage reaction of hydrous iridium oxide layers. *J. Electroanal. Chem.*, 162:121, 1984.

[44] S. Trasatti. Transition metal oxides: versatile materials for electrocatalysis. In J. Lipkowski and P. N. Ross, editors, *Electrochemistry of novel materials*, page 207. VCH, New York, 1994.

[45] D. Michell, D. A. J. Rand, and R. Woods. A study of ruthenium electrodes by cyclic voltammetry and X-ray emission spectroscopy. *J. Electroanal. Chem.*, 89:11, 1978.

[46] M. Pourbaux. *Atlas of electrochemical equilibria in aqueous solutions.* NACE, Houston, 2 edition, 1974.

[47] M. A. Petit and V. Plichon. Anodic electrodeposition of iridium oxide films. *J. Electroanal. Chem.*, 444:247, 1998.

[48] R. Kötz, H. J. Lewerenz, P. Brüesch, and S. Stucki. Oxygen evolution on Ru and Ir electrodes. XPS studies. *J. Electroanal. Chem.*, 150:209, 1983.

[49] T.C. Wen and C.C. Hu. Hydrogen and oxygen evoluion on Ru-Ir binary oxides. *J. Electroanal. Chem.*, 138:2158, 1992.

[50] J. E. Weston and B. C. H. Steele. Proton diffusion in crystalline ruthenium dioxide. *J. App. Electrochem*, 10:49, 1980.

[51] S. Ardizzone, G. Fregonara, and S.Trasatti. Inner and outer active surface of RuO_2 electrodes. *Electrochim. Acta*, 35:263, 1990.

[52] I. R. Burrows, D. A. Denton, and J. A. Harrison. Chlorine and oxygen evolution on various compostions of RuO_2/TiO_2 electrodes. *Electrochimica Acta*, 23:493, 1978.

[53] S. H. Glarum and J. H. Marshall. The AC response of iridium oxide films. *J. Electrochem. Soc.*, 127:2727, 1980.

[54] J. Rishpon and S. Gottesfeld. Resolution of fast and slow charging processes in ruthenium oxide films; an AC impedance and optical investiagion. *J. Electrochem. Soc.*, 131:1960, 1984.

[55] T. A. F. Lassali, J. F. C. Boodts, and L. O. S. Bulhões. Charging process and electrocatalytic properties of IrO_2 / TiO_2 / SnO_2 oxide films investiagetd by in situ ac impedance measurements. *Electrochimica Acta*, 44:4203, 1999.

[56] V. A. Alves, L. A. da Silva, and J. F. C. Boodts. Electrochemical impedance spectroscopic study of dimensionally stable anode corrosion. *J. Appl. Electrochem.*, 28:899, 1998.

[57] L. A. Da Silva, V. A. Alves, M. A. P. da Silva, S. Trasatti, and J. F. C. Boodts. Oxygen evolution in acid solution on $IrO_2 + TiO_2$ ceramic films. a study by impedance, voltammetry and sem. *Electrochim. Acta*, 42:271, 1996.

[58] R. Adams and R. L. Shriner. Platinum oxide as a catalyst in the reduction of organic compounds. iii. Preparation and properties of the oxide of platinum obtained by the fusion of chloroplatinic acid with sodium nitrate. *The Journal of the American Chemical Society*, 45:2171, 1923.

[59] B. Mattsson. *Polymer ionic materials*. PhD thesis, Chalmers University of Technology, 1998.

[60] N. Walsby. *Preparation and characterisation of radiation-grafted membranes for fuel cells*. PhD thesis, University of Helsinki, 1996.

[61] T. D. Gierke, G. E. Munn, and F. C. Wilson. The morphology in Nafion® perfluorinated membrane products as determined by wide- and small- angle X-Ray studies. *J. Polymer. Sci.*, 19:1687, 1981.

[62] C. Gavach, G. Pamboutzoglou, M. Nedyalkov, and G. Pourcelly. AC impedance ivestigation of the kinetics of ion transport in Nafion® perfluorosulfonic membranes. *J. Memb. Sci.*, 45:37, 1989.

[63] T. A. Zawodzinski, J. Davey, J. Valerio, and S. Gottesfeld. The water content dependence of electro-osmotic drag in proton-conducting polymer electrolytes. *Electrochim. Acta*, 40:297, 1995.

[64] K. M. Nouel and P. S. Fedkiw. Nafion based composite polymer electrolyte membranes. *Electrochim. Acta*, 43:2381, 1998.

[65] M. Wakizoe, O. A. Velev, and S. Srinivasan. Analysis of proton exchange membrane fuel cell performance with alternate membranes. *Electrochim. Acta*, 30:335, 1995.

[66] N. Yoshida, T. Ishisaki, A. Watakabe, and M. Yoshitake. Characterization of Flemion® membranes for PEFC. *Electrochim. Acta*, 43:3749, 1998.

[67] K. Broka and P. Ekdunge. Oxygen and hydrogen permeation properties and water uptake of Nafion® 117 membrane and recast film for PEM fuel cell. *J. Appl. Electrochem.*, 27:117, 1997.

[68] E. Passalacqua, F. Lufrano, G. Squadrito, A. Patti, and L. Giorgi. Nafion content in the catalyst layer of polymer electrolyte fuel cell: effects on structure and performance. *Electrochim. Acta*, 46:799, 1996.

[69] P. Millet, R. Durand, and M. Pineri. Preparation of new solid polymer electrolyte composites for water electrolysis. *J. Hydrogen Energy*, 15:245, 1990.

[70] P. Millet, T.Alleau, and R. Durand. Characterization of membrane-electrode assemblies for solid polymer electrolyte water electrolysis. *Journal of applied electrochemistry*, 23:322, 1993.

[71] A. Michas and P. Millet. Metal and metal oxides based membrane composites for solid polymer water electrolysers. *J. Membrane Science*, 61:157, 1991.

[72] C. Mitsugi, A. Harumi, and F. Kenzo. WE-NET: Japanese hydrogen program. *Int. J. Hydrogen Energy*, 23:159, 1998.

[73] H. Mori, C. Inazumi, M. Kato, S. Maezawa, K. Oguro, H. Takenaka, and E. Torikai. Development of membrane-electrode composites for polymer electrlyte water electrolysis using new chemical plating method. In T. N. Verziroğlu, C. J. Winter, J. P. Baselt, and G. Kreysa, editors, *Hydrogen Energy progress XI*, volume 1, page 579, 1996.

[74] Y. Kawami Y. Naka E. Torikai, H. Takenaka and K. Nagaya. Japan Pat. no. 60-162780, 1985.

[75] C. Inazumi, H. Mori, M. Kato, S. Meazawa, N. Sawai, K. Oguro, and H. Takenaka. The long-term stability of the solid polymer electrolyte water electrolyzer. In T. N. Verziroğlu, C. J. Winter, J. P. Baselt, and G. Kreysa, editors, *Hydrogen Energy progress XI*, volume 1, page 741, 1996.

[76] H. Takenaka T. Sakai, Y. Kawami and E. Torikai. Effects of surface roughening of Nafion® on electrode plating, mechanical strength, and cell perfromances for SPE water electrolysis. *J. Electroanal. Chem.*, 12:3777, 1990.

[77] M. Kondoh, N. Yokoyama, C. Inazumi, S. Maezawa, N. Fujiwara, Y. Nishimura, K. Oguro, and H. Takenaka. Development of solid polymer-electrolyte water electrolyser. *J. New Mat. for Electrochem. Sys.*, 3:61, 2000.

[78] T. Ioroi, N. Kitazawa, K. Yasuda, Y. Yamamoto, and H. Takenaka. Iridium oxide/platinum electrocatalysts for unitized regenerative polymer electrolyte fuel cells. *J. Electrochem. Soc.*, 147:2018, 2000.

[79] M. Yamaguchi, K. Okisawa, and T. Nakanori. Development of high performance solid polymer electrolyte water electrolyzer in WE-NET. In *32nd Enfersociety Energy Conversion Engineering Conference*, http://www.enaa.or.jp/WE-NET/ronbun/ p_1997_e.html. WE-NET.

[80] M. Yamaguchi, T. Shinohara, H. Taniguchi, T. Nakanori, and K. Okisawa, 1998. http://www.enaa.or.jp/WE-NET/ronbun/1998/10/1098.htm.

[81] K. Ledjeff, A. Heinzel, V. Peinecke, and F. Mahlendorf. Development of pressure electrolyser and fuel cell with polymer electrolyte. *Int. J. Hydrogen Energy*, 19:453, 1993.

[82] K. Ledjeff, F. Mahlendorf, V. Peinecke, and A. Heinzel. Development of electrode membrane units for the reversible poymer fuel cell (rspfc). *Electrochemical Acta*, 40:315, 1995.

[83] F. Mahlendorf. *Elektrodenkinetische untersuchungen der bifuntionellen oxidationselektrode von reversiblen membranbrennstoffzellen.* PhD thesis, Albert-Ludwigs-Universität Freiburg im Breisgau, 1995.

[84] S. Stucki, G. G. Scherer, S. Schlagowski, and E. Fischer. PEM water electrolysers: evidence for membrane failure in 100 kW demonstration plants. *J. Appl. Electrochem.*, 28:1041, 1998.

[85] CH. Comninellis and G. P. Vercesi. Characterization of DSA® -type oxygen evolving electrodes: choice of a coating. *J. Appl. Electrochem.*, 21:335, 1991.

[86] L. Ma, S. Warthesen, and D. A. Shores. Evaluation of materials for bipolar plates in PEMFCs. *J. New Mat. Electrochem. Sys.*, 3:221, 2000.

[87] D. P. Davies, P. L. Adcock, M. Turpin, and S. J. Rowen. Bipolar plate materials for solid polymer fuel cells. *J. Appl. Electrochem.*, 30:101, 2000.

[88] D. R. Hodgson, B. May, P. L. Adcock, and D. P. Davies. New lightweight bipolar plate system for polymer electrolyte membrane fuel cells. *J. Power Sources*, 96:233, 2001.

[89] H. B. Beer. Improvements in or relating to electrodes for electrolysis. British Pat. no. 1,147,442, 1969.

[90] J. F. C. Boodts L. M. Da Silva and L. A. De Faria. 'In situ' and 'ex situ' characterization of the surface properties of the $RuO_2(x) - Co_3O_4(1\text{-}x)$ system. *Electrochim. Acta*, 45:2719, 2000.

[91] R. Kötz and S. Stucki. Stabilization of RuO_2 by IrO_2 for anodic oxygen evolution in acid media. *Electrochim. Acta*, 31:1311, 1986.

[92] O. De Nora, G. Bianchi, A. Nidola, and G. Trisoglio. Method of electrowinning metals. US Pat. no. 3,926,751, 1975.

[93] F. I. Mattos-Costa, P. de Lima-Neto, S. A. S. Machado, and L. A. Avaca. Characterisation of surfaces modified by sol-gel derived $Ru_xIr_{1-x}O_2$ coatings for oxygen evolution in acid medium. *Electrochimica Acta*, 44:1515, 1998.

[94] R. Mráz and J. Krýsa. Long service life IrO_2/Ta_2O_5 anodes. *J. Appl. Electrochem.*, 24:1262, 1994.

[95] M. Morimitsu R. Otogawa and M. Matsunaga. Effect of microstructure of IrO_2-based anodes on electrocatalytic properties. *Electrochim. Acta*, 44:1509, 1997.

[96] S. Kulandaisamy, J. Prabhakar, S. C. Chockalingam, S Visvanathan, K. V. Venkateswaran, P. Ramachandran, and V. Nandakumar. Perforance of catalytically activated anodes in the electrowinning of metals. *J. Appl. Electrochem.*, 27:579, 1997.

[97] G. P. Vercesi, J. Y. Salamin, and CH. Comninellis. Morphological and microstructural study of the Ti/IrO_2-Ta_2O_5. *Electrochim. Acta*, 36:991, 1991.

[98] J. Krýsa, L. Kule, R. Mráz, and I Roušar. Effect of coating thickness and surface treatment of titanium on the properties of IrO_2-Ta_2O_5. *J. Appl. Electrochem.*, 26:999, 1996.

[99] E. N. Loubnin A. V. Popov Yu. I. Ulitina V. V. Zhurov Yu. E. Roginskaya, O. V. Morozova and S.Trasatti. X-ray diffraction, transmission electron microscopy and X-ray photoelectron spectroscopic characterization of IrO_2 + Ta_2O_3 films. *J. Chem. Soc. Faraday Trans.*, 89:1707, 1993.

[100] T. A. F. Lassali, L. O. S. Bolhões, L. M. C. Abeid, and J. F. C. Boodts. Surface characterization fo thermally prepared, Ti-supported, Ir-based electrocatalysts containing Ti and Sn. *Electrochim. Acta*, 144:3348, 1997.

[101] R. Hutchings, R. Kötz, K. Müller, and S. Stucki. A structural investigation of stabilized oxygen evolution catalysts. *J. Mat. Science*, 19:3987, 1984.

[102] B. Baroux, G. Béranger, and C. Lemaitre. *Stainless Steels*, chapter 5. Les Editions de Physique Les Ulis, 1993.

[103] A. K. Roy, M. K. Spragge, D. L. Fleming, and B. Y. Lum. Cracking of titanium alloys under cathodic applied potentials. *Micron*, 32:211, 2001.

[104] P. Millet. Water electrolyisis using eme technology: Electric potential distribution inside a nafion membrane during electrolysis. *Electrochim. Acta*, 39:2501, 1994.

[105] S. Møller Holst. *Solid Polymer Fuel Cells, Electrode and Membrane Performance Studies*. PhD thesis, Norwegian University of Science and Technology, 1996.

[106] M. S. Wilson and S. Gottesfeld. High performance catalyzed membranes of ultra-low Pt loadings for polymer electrolyte fuel cells. *J. Electrochem. Soc*, 139:L28, 1992.

[107] E. A. Ticianelli, C. R. Derouin, A. Redondo, and S. Srinivasan. Methods to advance technology of proton exchange membrane fuel cells. *J. Electrochem. Soc*, 135:2209, 1988.

[108] M. S. Wilson, J. A. Valerio, and S. Gottesfeld. Low platinum loading electrodes for polymer electrolyte fuuel cells fabricated using thermoplastic ionomers. *Electrochim. Acta*, 40:355, 1995.

[109] J. L. Weininger and R. R. Russel. Corrosion of the ruthenium oxide catalyst at the anode of a solid polymer electrolyte cell. *J. Electrochem. Soc.*, 125:1452, 1978.

[110] T. C. Liu, W. G. Pell, and B. E. Conway. Self-discharge and potential recovery phenomena at thermally and electrochemically prepared RuO_2 supercapacitor electrodes. *Electrochimica Acta*, 42, 1999.

[111] M. J. Jørgensen, S. Primdahl, and M. Mogensen. Characterisation of composite SOFC cathodes using electrochemical impedance spectroscopy. *Electrochim. Acta*, 33:4195, 1999.

[112] J. Winkler, P. V. Henriksen, N. Bonanos, and M. Mogensen. Geometric requirements of solid electrolyte cells with a reference electrode. *J. Electrochem. Soc.*, 44:1515, 1998.

[113] R. Halseide, P. J. S. Vie, R. J. Aaberg, and R. Tunold. Influence of cell geometry on AC-impednace measurements as applied to PEFCs. In F. N. Büchi, G. G. Scherer, and A. Wokaun, editors, *1st European PEFC Form Prodeedings*.

[114] P. Millet, R. Durand, E. Dartyge, G. Tourillon, and A. Fontaine. Precipitation of metallic platinum into Nafion ionomer membranes. *J. Electrochem. Soc.*, 140:1373, 1993.

[115] J. F. C. Boodts and S. Trasatti. Effect of compostion fo the electrocatalytic activity of the ternary oxide $Ru_{0.3}Ti_{0.7-x}Sn_xO_2$. *J. Electrochem. Soc.*, 137:3784, 1990.

[116] A. Ferry, M. M. Doeff, and L. C DeJonghe. Transport property measurements of polymer electrolytes. *Electrochim. Acta*, 43:1387, 1998.

[117] L. L. Swette, A. B. LaConti, and S. A. McCatty. Proton-exchange membrane regenerative fuel cells. *J. Power Sources*, 47:343, 1994.

[118] G. Lodi, A. De Battisti, A. Benedetti, G. Fagherazzi, and J. Kristof. Formation of iridium metal in thermally prepared iridium dioxide coatings. *J. Electroanal. Chem.*, 256:441, 1988.

[119] I. Epelboin and M. Keddam. Faradaic impedances: Diffusion impedance and reaction impedance. *J. Electrochem. Soc*, 117:1052, 1970.

[120] O. Antoine, Y. Bultel, and R. Durand. Oxygen reduction reaction kinetics and mechanism on platinum nanoparticle inside Nafion®. *J. Electroanal. Chem.*, 499:87, 2001.

[121] S. Pyun and Y-G. Ryu. A study of oxygen reduction on platinum-dispersed porous carbon electrodes at room and elevated temperatures by using a.c. impedance spectroscopy. *J. Power Sources*, 62:1, 1996.

[122] G. Lodi, A. De Battisti, G. Bordin, C. De Asmundis, and A. Benedetti. Microstucture and electrical properties of iro$_2$ prepared by thermal decomposition of $IrCl_3 \cdot xH_2O$. *J. Electroanal. Chem.*, 277:139, 1990.

[123] S. Trasatti. Electrocatalysis: understanding the success of DSA®. *Electrochim. Acta*, 45:2377, 2000.

[124] A. Dey A. Damjanovic and J. O'M. Bockris. Electrod kinetics of oxygen evolution and dissolution on Rh, Ir and Pt-Rh alloy electrodes. *J. Electrochem. Soc.*, 113:739, 1966.

[125] S. A. S Machado L. A. Avaca A. de Oliveira-Sousa, M. A. S. da Silva and P. de Lima-Neto. Influence of the preparation method on the morphological and electrochemical properties of Ti/IrO_2-coated electrodes. *Electrochim. Acta*, 45:4467, 2000.

[126] S. Trasatti L. A. da Silva, V. A. Alves and J. F. C. Boodts. Surface and electrocatalytic properties of ternary oxides $Ir_{0.3}Ti_{0.7-x}PtO_2$. Oxygen evolution from acidic solution. *J. Electroanal. Chem.*, 427:97, 1996.

[127] L. A. Da Silva, V. A. Alves, S. Trasatti, and J. F. C. Boodts. Surface and electrocatalytic properties of ternary oxides $Ir_{0.3}Ti_{0.7-x}Pt_xO_2$. oxygen evolution from acidic solution. *J. Electroanal. Chem.*, 427:97, 1997.

[128] C. Angelinetta and S. Trasatti. Surface properties of RuO_2 + IrO_2 electrodes. *J. Electroanal. Chem*, 214:535, 1986.

[129] C. Angelinetta, M. Falciola, and S. Trasatti. Heterogeneous acid-base equilibria and reaction order of oxygen evolution on oxide electrodes. *J. Electroanal. Chem*, 205:347, 1986.

[130] S.M. Lin and T. C. Wen. Oxygen evolution on IrRuSn ternary oxide-coated electrodes in H_2SO_4 solution. *J. Electrochem. Soc.*, 140:2265, 1993.

[131] R. Viganò, J. Taraszewska, A. Daghetti, and S.Trasatti. The point of zero charge of RuO_2 + IrO_2 mixed oxides. *J. Electroanal. Chem.*, 182:203, 1985.

[132] R. R. Ralph, G. A. Hards, J. E. Keating, S. A. Campbell, D. P. Wilkinson, M. Davis, J. St-Pierre, and M. C. Johnson. Low cost electrodes for proton exchange membrane fuel cells. *J. Electroanal. Chem.*, 144:3845, 1997.

[133] C. Boyer, S. Gamburzev, O. Velev, S. Srinivasan, and A. J. Appleby. Measurements of proton conductivity in the active layer of PEM fuel cell gas diffusion electrodes. *Electrochim. Acta*, 43:3703, 1998.

[134] A. A. Kulikovsky, J. Divisek, and A. A. Kornyshev. Modeling the cathode compartment of polymer electrlyte fuel cells: dead and active reaction zones. *J. Electrochem. Soc.*, 146:3981, 1999.

[135] Y. M. Maksimov, B. I. Podlovchenko, and T. L. Azarchenko. Preparation and electrocatalytic properties of microparticles incorporated into polyvinylpyridine and Nafion films. *Electrochim. Acta*, 43:1053, 1998.

[136] M. Khalioullin, N. Kuleshov, S. Grigoriev, and V. Fateev. SPE-electrolysis under increased pressure. page 97, St. Petersburg, 1999. HYPOTHESIS III.

[137] A. Fischer, J. Jindra, and H. Wendt. Porosity and catalyst utilization of thin layer cathodes in air operated PEM-fuel cells. *J. Appl. Electrochem.*, 28:277, 1998.

[138] E. R. Kötz and S. Stucki. Ruthenium dioxide as a hydrogen-evolving cathode. *J. Appl. Electrochem.*, 17:1190, 1987.

[139] S. Ardizzone, G. Freganora, and S. Trasatti. Influence of hydrogen evolution on the voltammetric charge of RuO_2 electrodes. *J. Electroanal. Chem.*, 266:191, 1989.

[140] M. Blouin and D. Guay. Activation of ruthenium oxide, iridium oxide, and mixed Ru_xIr_{1-x} oxide electrodes during cathodic polarization and hydrogen evolution. *J. Electrochem. Soc.*, 144:573, 1997.

[141] L. Chen, D. Guay, and A. Lasia. Kinetics of the hydrogen evolution reaction on RuO_2 and IrO_2 oxide electrodes in H_2SO_4 solution: An AC impedance study. *J. Electrochem. Soc.*, 143:3576, 1996.

[142] I. M. Kodintsev and S. Trasatti. Electrocatalysis of H_2 evolution on RuO_2 + IrO_2 mixed oxide electrodes. *Electrochim. Acta*, 39:1803, 1994.

[143] Y. Balolian S. Zhigang and H. Ming. Bifunctional electrodes with a thin catalyst layer for unitized proton exchnage membrane regenerative fuel cell. *J. Power Sources*, 79:82, 1999.

[144] M. Grzeszczuk and P. Poks. The HER performance of colloidal Pt nanoparticles incorporated in polyaniline. *Electrochim. Acta*, 45:4171, 2000.

[145] A. Losch and J. W. Schultze. Impedance spectroscopy and other electrochemical in-situ investigations of the phosphating process. *J. Electroanal. Chem.*, 359:39, 1993.

[146] L.O. Valøen. *Metal Hydrides for Rechargeable Batteries*. PhD thesis, Norwegian University of Science and Technology, 2000.

[147] R. N. Goldberg and L. G. Hepler. Thermochemistry and oxidation potentials of the platinum group metals and their compounds. 12:154, 1967.

[148] W. Hume-Rothery and G.V. Raynor. *The Structure of Metals and Alloys*. Inst. of Metals, London, 1954.

APPENDIX

Appendix A

Design of PEM cell

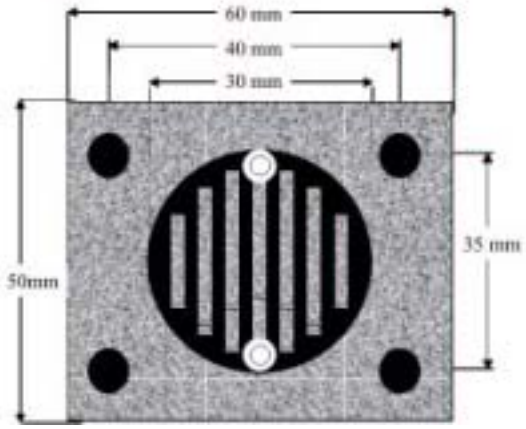

Figure A.1: Flow field pattern of PEM cell.

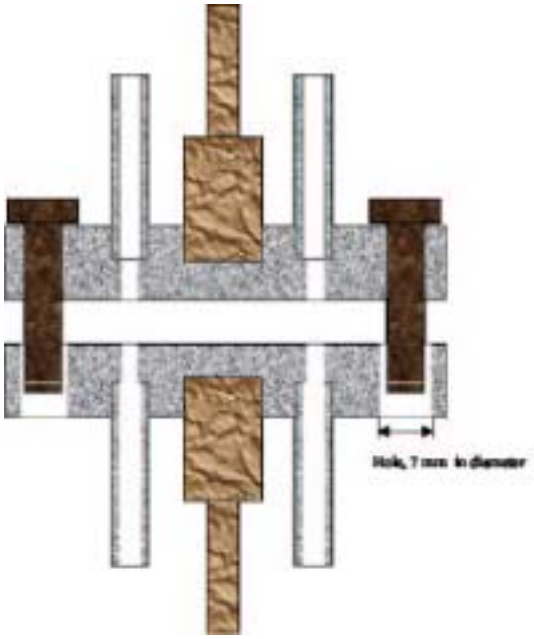

Figure A.2: PEM cell from above.

Figure A.3: PEM cell mounted in a clamp.

Appendix B

SEM photos

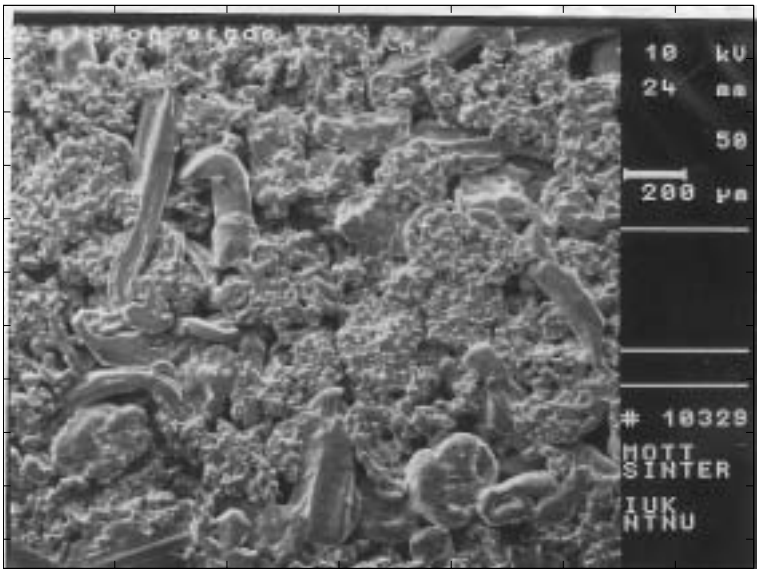

Figure B.1: Ti-current collector magnified 50X.

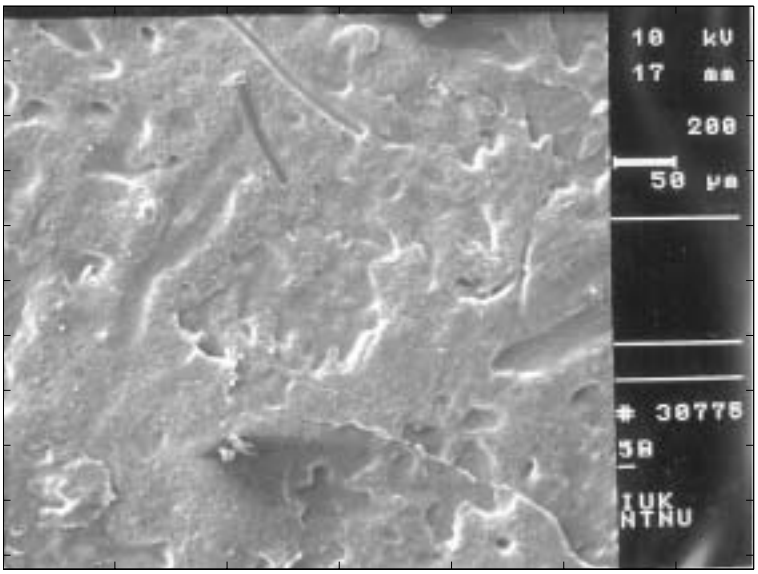

Figure B.2: Catalytic layer after electrochemical measurements. Patterns from the Ti-current collector can be seen. Magnified 200X.

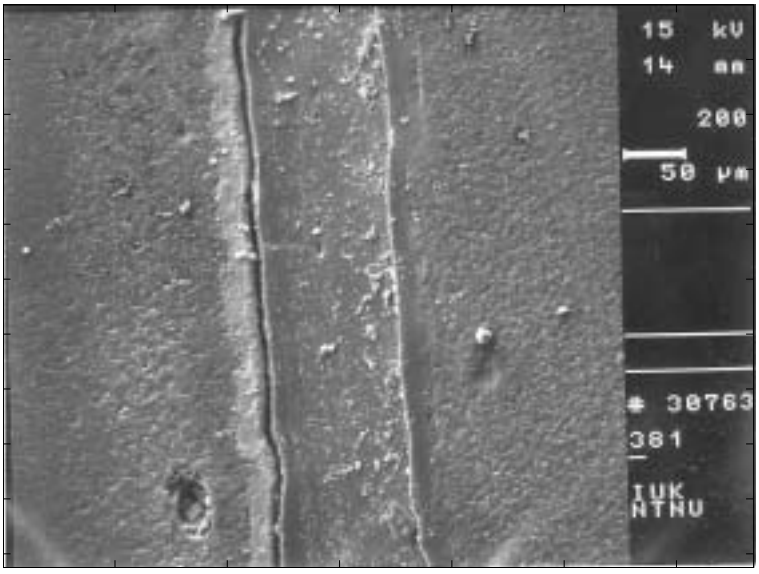

Figure B.3: Cross section image of an MEA showing anode layer to left and cathode layer to right. Magnified 200X.

Appendix C

Physical parameters

Table C.1: Physical properties of some metal oxides

Substance	Gitter constants a	b	c	Electron config.	ΔG_f^0
RuO_2	4.4906	-	3.1064	$4d^4$	-255.4 [147]
IrO_2	4.4990	-	3.1546	$5d^5$	-175.8 [147]
PtO_2	4.4867	4.5366	3.1375	$5d^6$	-276.3 [147]
PdO_2	-	-	-	–	-301.4 [147]
Rh_2O_3	4.4862	-	3.0884	$4d^5$	-272.5 [147]
TiO_2	4.594	-	2.958	$3d^0$	-
Ta_2O_5	4.709	-	3.065	$5d^1$	-
SnO_2	4.738	-	3.188	$4d^{10}$	-
PbO_2	4.955	-	3.383	$5d^{10}$	-

Hume-Rothery rules

Limits of solid solubility [148]:

- difference in atomic size less thant 15%
- solute and solvent should crystallize with same crystal lattice
- solute and solvent should have the same valence
- chemically resemble eatch other - not forming a coumpound